The Effect of Microstructure on the Spatial Distribution of the Damage Produced by Ions in Solids

Hosny M. Attaya

May 1981

UWFDM-420

Ph.D. thesis.

FUSION TECHNOLOGY INSTITUTE

UNIVERSITY OF WISCONSIN

MADISON WISCONSIN

The Effect of Microstructure on the Spatial Distribution of the Damage Produced by Ions in Solids

Hosny M. Attaya

Fusion Technology Institute
University of Wisconsin
1500 Engineering Drive
Madison, WI 53706

http://fti.neep.wisc.edu

May 1981

UWFDM-420

Ph.D. thesis.

THE EFFECT OF MICROSTRUCTURE ON THE SPATIAL DISTRIBUTION OF THE DAMAGE PRODUCED BY IONS IN SOLIDS

BY

HOSNY M. ATTAYA

A thesis submitted in partial fulfillment of the requirements for the degree of

DOCTOR OF PHILOSOPY

Nuclear Engineering

at the

UNIVERSITY OF WISCONSIN-MADISON

1981

THE EFFECT OF MICROSTRUCTURE ON THE SPATIAL DISTRIBUTION OF THE DAMAGE PRODUCED BY IONS IN SOLIDS

A thesis submitted to the Graduate School of the University of Wisconsin-Madison in partial fulfillment of the requirements for the degree of Doctor of Philosophy

by

Hosny M. Attaya

Degree to be awarded: December 19____ May 1981___ August 19____

Approved by Thesis Reading Committee:

Major Professor — March 30, 1981, Date of Examination

Dean, Graduate School

THE EFFECT OF MICROSTRUCTURE ON THE SPATIAL DISTRIBUTION OF THE DAMAGE PRODUCED BY IONS IN SOLIDS

Hosny M. Attaya

Under the Supervision of Professor Gerald L. Kulcinski

The accurate estimation of the ranges and damage of primary knock on atoms or injected ions in materials is critical to the successful operation of fusion reactors. Recent measurements of the ranges and damage of ions in material show that there are large differences between theory and experiment.

In this work, a three-dimensional Monte-Carlo model, HERAD, has been developed to study the ranges and the damage of ions in materials. The model incorporates the options to use a large number of nuclear and electronic stopping models. The HERAD code takes into account the presence of cavities on the range and ion distribution. The results of the HERAD model were compared to the other current computational models, and the effect of cavities on the range as well as the distribution of damage was studied. The HERAD code yields a closer agreement between experiments and theory than other computational models. The code is also shown to be less expensive to run and more versatile than present Monte Carlo codes for radiation damage calculations. A reduction of more than 80% of the LSS

electronic cross section was found to produce better agreement between theory and experiment.

APPROVED

March 30, 1981

Date

Professor Gerald L. Kulcinski
Nuclear Engineering

Acknowledgements

I wish to single out a few of the many persons who contributed to the completion of this work. First, I would like to express my deep thanks and gratitude to my thesis advisor Professor Gerald L. Kulcinski for his continual encouragement, guidance, support, and for everything I am very much indebted.

Sincere thanks also to Professor Charles W. Maynard for his help and willingness to discuss some of the problems in this work, and for his helpful suggestions.

Acknowledgement also to all my professors in the Nuclear Engineering departments of the University of Wisconsin and the University of Alexandria, and in particular Professors Y. Elmeshad and M. El Fouly.

I am grateful to Drs. N. Ghoniem and T. Hunter, both of whom initiated my interest in the Radiatiam Damage Studies, and were of great help to me.

I am also indebted to Drs. M. T. Robinson and J. P. Biersack who have made their codes available to me, and for many valuable discussions with them.

Special thanks are due to all the members of the Radiation Damage Group and in particular, Dr. J. Billen, D. Jackson, R. Zee, K. McLaurin, B. Knoll, and D. Bullen for preparing and irradiating the nickel samples. Thanks to Dr. M. Sawan for his help in editing the thesis.

The patience, understanding, and care of my wife, Hala, have been of great help to me and played a major role in the completion of my work.

Last, but not least, I would like to acknowledge Ms. B. Brown whose patience and attention to detail in the preparation of this thesis was masterful indeed.

TABLE OF CONTENTS

TABLE OF CONTENTS (continued)

TABLE OF CONTENTS (continued)

CHAPTER I

INTRODUCTION

Most current theories of the production of defects in solids neglect the evolutionary nature of the microstructure and the effect that it can have on the ultimate spatial distribution of defects. This problem is especially critical for solids irradiated with charged particles which have rather short ranges in the material. These charged particles could emanate from nuclear fission reactions or from the leakage of plasma debris (D^+, T^+, He^{++}, etc.) from a thermonuclear reaction. Another source of such short range charged particles would be an accelerator used for research or commercial applications in the solid state industry.

There are at least two areas where a proper treatment of the emerging microstructure is very important. The first is the production of gas bubbles below the surface of a fusion reactor first wall bombarded with low energy (10-1000 KeV) helium atoms, and the second is the production of voids in heavy ion bombarded metals. In both of these examples the production of defects varies considerably as the particle travels into the solid and it theoretically drops to zero at the end of the particle range. However, if voids or bubbles form in the damage zone, then it is reasonable to expect that the average range of the particle (as measured from the front surface) will increase as the bombarding particles now encounter, on the average, fewer atoms per cm^3 in their path.

Such observations have indeed been made experimentally. For example, it has been normally accepted that the blister thickness of a metal irradiated with helium atoms would be roughly equal to the projected range in the unirradiated metal. However, in some studies [1], the blister skin thickness was found to be larger than the range of the helium ions. In those studies, no corrections were made because of the fact that a very high density of helium gas bubbles reduced the average density of metallic atoms in the ion's path. A similar situation has recently arisen in the ion bombardment simulation studies. Whitley et al. [2] and Narayan et al. [3] have found that damage can be observed well beyond the projected range in an unirradiated metal. It is possible that there may be other explanations for this behavior, such as overestimates of the electronic stopping powers, channeling, etc., but it is also possible that the less dense microstructure near the surface can have an effect on ultimate spread in the range of particles.

There have been previous attempts to include the presence of the cavities on the damage calculations [4,5] but the proposed corrections have been merely first order, one-dimensional gross density adjustments. In the present study, a three-dimensional Monte Carlo code, HERAD (Heterogeneous Radiation Damage) has been developed to study such effects.

A great deal of this thesis research (Chapters 2, 3, 4) has been devoted to study the previous theories and codes which have been developed to describe the production of damage in unirradiated

materials. In general it was found that the present codes are inadequate to describe the problems studied here. Therefore, a large effort was required to identify the best features from the theories available, and second, to write a computer code (Chapter 5) which would be at the same time both accurate and inexpensive to run. The flexibility to use different interatomic potentials, different energy loss models, and to take into account the presence of cavities on the ion transport and the damage production was deemed to be a vital feature of such a universal code. The usefulness of the HERAD code in this respect will be illustrated by comparison to other widely used codes including both qualitative and quantitative observations on test problems (Chapter 6). Finally, the HERAD code will be compared in Chapter 6 to recent experimental measurements of the ranges of ions, and the damage produced by ions.

To summarize, the objective of this thesis is to construct a model which will be inexpensive and simple to run on a standard computer and will give the greatest amount of the information about the ranges of incident ions in materials and the damage they produce in solids which are either homogeneous or contain randomly placed heterogeneities.

References for Chapter I

1. M. Kaminsky, Adv. Chem. Series 155, 112 (1976).

2. J. B. Whitley, G. L. Kulcinski, H. V. Smith, and P. Wilkes, "Effects of Radiation on Structural Materials," ASTM-STP-683, J. A. Sprague and D. Kramer, eds., American Society for Testing and Materials, 125-142 (1979).

3. J. Narayan, T. S. Noggle, and O. S. Oen, Proceeding of Int. Conf. on "Fundamental Aspects of Radiation Damage in Materials, " Gatlinberg, Tenn., Oct. 1975, CONF-751006, 90 (1976).

4. G. R. Odette, D. M. Schwortz, and A. J. Ardell, Rad. Eff. 22, 217 (1974).

5. W. G. Johnston, T. H. Rosolowski, A. M. Turkalo, and T. Lauritzen, J. Nucl. Mat. 47, 155 (1971).

CHAPTER II

SLOWING DOWN OF IONS IN MATERIALS

II-1. Introduction

A description of the interaction of ions with target atoms is essential for a clear understanding of the slowing down of ions in material. The nature of ionic interactions is also important to obtain the associated quantities of interest in this study, such as the range and damage. In general, this interaction involves all the constituents of the two interacting particles, i.e. electrons and nuclei, and presents a complicated many-body problem. Because of the possible excitation and/or ejection of one or more of the involved electrons, the interaction can be inelastic.

As was suggested first by Bohr [1], this problem can be simplified by separating the interaction into an inelastic part, in which energy is transferred to individual electrons of the atoms (electronic stopping), and a quasi-elastic part in which momentum and kinetic energy are transferred to translatory motion of the stopping atom. In the latter process the presence of electrons merely involves an electrostatic screening of the nuclear field of force (nuclear stopping).

Such a separation procedure is a justifiable approximation because of the negligible amount of momentum an electron can have compared to that of the nucleus, and because the inelastic energy loss in individual collisions is often small [2]. Both parts, i.e.

nuclear and electronic stoppings, are energy dependent. Figure 2-1 shows the dependence of both on the ion velocity.

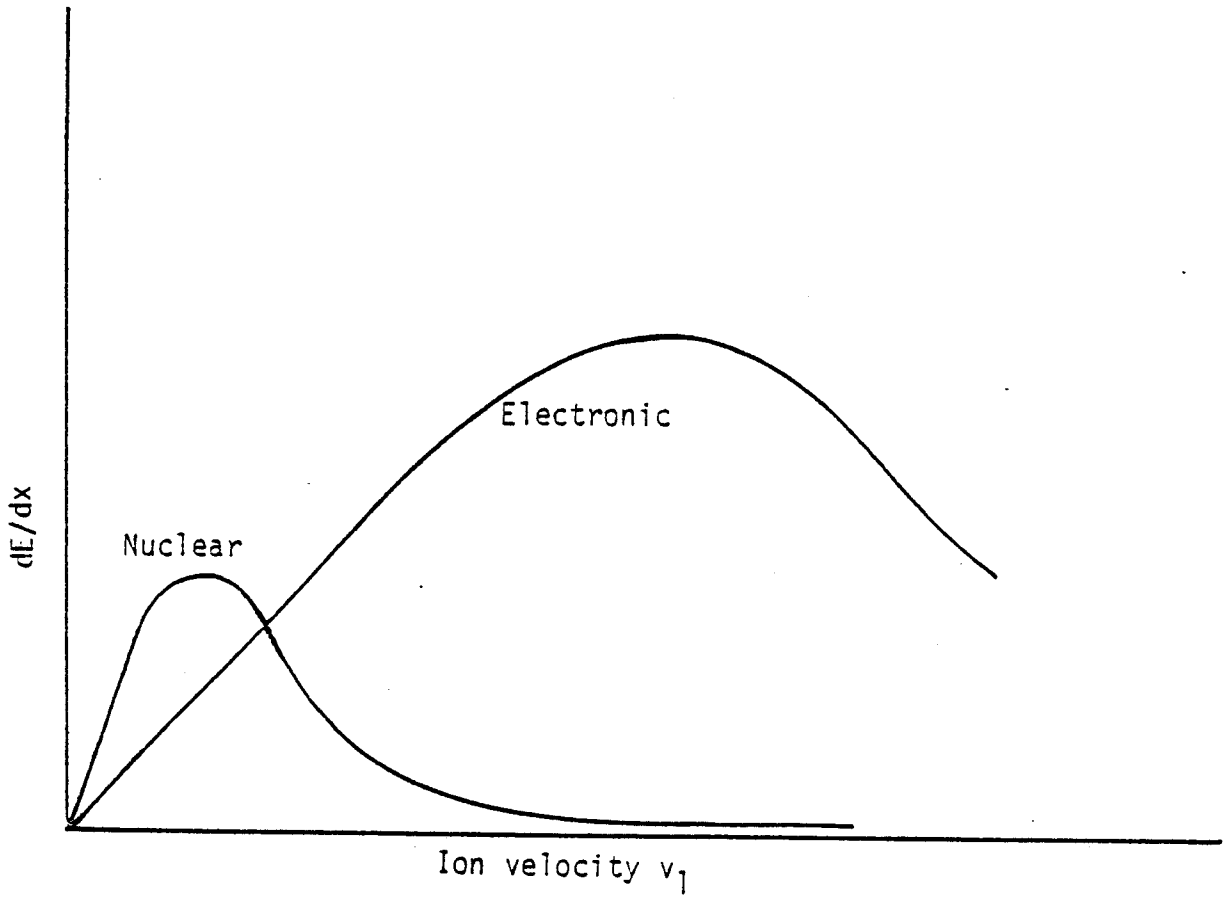

Fig. 2-1. The behavior of the nuclear and electronic contributions to the total energy loss as a function of the ion velocity v_1.

II-2. Electronic Stopping and Screening of the Ion

For highly energetic ions whose velocity is greater than any orbital velocity of the ion-core electrons, i.e. when $v_1 > Z_1 v_o$*, the ion acts as a point charge with a value equal to $Z_1 e$. In this case, the electronic stopping dominates and is described adequately by the Bethe-Bloch equation [3]:

$$\frac{dE_1}{dx} = \frac{4\pi Z_1^2 Z_2 e^4}{m_e v_1^2} \ln \left(\frac{2 m_e v_1^2}{\langle I \rangle}\right) , \qquad (2.1)$$

for nonrelativistic energies, where $\langle I \rangle$ is the average excitation energy of the stopping atom, Z_2.

As the ion energy is reduced so that $v_1 \approx Z_1^{2/3} v_o$, where $Z_1^{2/3} v_o$ is the mean electron velocity, the ion starts to acquire bound electrons, and its nuclear charge begins to be screened by these electrons. No precise theoretical treatment for the electronic energy loss exists for this case due to the complications and the uncertainties of the ion wave function introduced by the acquired electrons (their orbitals are highly distorted and it is difficult to

---

*Throughout this thesis we will abide, unless otherwise stated, with the following notations and symbols:

Z_1, Z_2	atomic number of the ion and the target atom, respectively;
M_1, M_2	atomic mass of the ion and the target atom, respectively;
E_1, v_1	energy and velocity of the ion, respectively;
e, m_e	electron charge and electron mass, respectively;
h	Plank's constant = 6.63×10^{-27} erg-sec;
$\hbar$	$= h/2\pi$;
a_o	Bohr radius = $\hbar^2/e^2 m_e = 0.529 \times 10^{-8}$ cm;
v_o	Bohr velocity = $e^2/\hbar$.

assign velocities for them [4]). The ion, in this velocity range, could be thought of as an ion with an effective charge $Z_{1eff}e \leq Z_1 e$, which can then be used in Eq. (1). Brandt [5] and Ziegler et al. [4] reviewed the concept of the effective charge. The effective charge is assumed to include the charge state of the ion as well as all the effects of the screening and all the perturbations of the ion's electrons [4].

In practice, the effective charge is obtained by a simple empirical formula given by Northcliff [6] as

$$Z_{1eff} \approx Z_1 \left(1 - \exp\left(-\frac{v_1}{v_o Z_1^{2/3}}\right)\right) \quad . \tag{2.2}$$

A similar empirical method [7] to obtain the effective charge is to scale the electronic stopping of an ion to that of the proton of the same velocity, i.e.

$$(Z_{1eff})^2 = S_e(Z_2, Z_1; E_1)/S_e(Z_2, 1; E_1/M_1) \quad . \tag{2.3}$$

We notice that the effective charge is independent of the target material. A similar empirical formula [7] for the effective charge is

$$\ln\left(1 - \frac{Z_{1eff}}{Z_1}\right) = (2m_e)^{1/2}\left[1 - (E_1/Q_1)^{1/2}\right] \quad , \tag{2.4}$$

which utilizes a threshold energy Q_1 given by

$$\begin{aligned} Q_1 &= v_o M_1 Z_1^{1.376} \\ &= [27.211 \text{ eV}]\, M_1 Z_1^{1.376} \quad . \end{aligned} \tag{2.5}$$

Ziegler et al. [4] have recently reviewed the electronic stopping in this velocity range (i.e. $v_1 > v_o Z^{2/3}$) and presented a compilation of extensive experimental data for many ion-target combinations.

As the ion velocity reduces further, $v_1 < v_o$, the ion is covered with an electron cloud that dynamically screens the ion charge over a distance a few times the screening length of the static atoms. For the long-range interaction with target electrons, the ion is effectively considered as a neutral atom.

Lindhard and Scharff [8] proposed that in this energy region S_e is proportional to the velocity as

$$S_e = 8\pi e^2 a_o \xi_e (Z_1 Z_2 / Z)\ v/v_o \quad , \tag{2.6}$$

where

$$Z^{2/3} = Z_1^{2/3} + Z_2^{2/3} \quad ,$$

and

$$\xi_e \approx Z_1^{1/6} \quad .$$

They suggested that the upper limit for the validity of this expression is $v_o Z^{2/3}$.

Firsov [9] also proposed a similar dependence of S_e on the velocity. Firsov's theory is based on some theoretical formulation. In this theory, a binary collision between an ion and an atom leads to mutual transfer of the ion's and atom's electrons which results in a

transfer of momentum, slowing down the ion. The flux of the electrons crossing an imaginary plane between the two particles could be calculated using the electron density and the electron velocity derived from the Thomas-Fermi stastical model. Firsov's formula is given by:

$$S_e = 7.51\ (3\pi^2\ \hbar\ a_o/32)(Z_1 + Z_2)\ v_1 \quad . \tag{2.7}$$

The more accurate Hartree-Fock electronic representation has been used [10] in a modification of Firsov's theory. Also Brice [11], using a precise quantum-mechanical definition of the flux, defined a bound state wave function which contains only that portion of the electronic motion that contributes to the flux in one direction across the Firsov plane, and then used three adjustable parameters to fit his resulting expression of S_e for all nonrelativistic velocities.

Neither Lindhard's theory nor Firsov's theory could predict the oscillatory dependence of S_e on the ion charge Z_1. Northcliff and Schilling [12] have employed the available experimental data to develop a semi-empirical correlation procedure which permits the estimation of the electronic stopping for many ion-target combinations.

Robinson [7] reviewed the electronic stopping and concluded that: "The electronic stopping S_e rises proportionally to the projectile velocity, at least approximately in accord with Lindhard theory (Eq. 2.6), at energies below about Q_1 (Eq. 2.5). Near Q_1, S_e

commences to increase more rapidly, reaching a broad maximum near $v_1 = v_o Z^{2/3}$".

The above discussion illustrates the uncertainties of electronic stopping powers and the need for more accurate theoretical estimation and experimental verification of such quantities.

II-3. Nuclear Stopping

When considering the collision of an ion with a target nucleus, one has to consider the interaction force between the two particles. This force is best described by a potential energy V(r) which arises from many-body interactions involving the electrons and the nuclei. From the basic principles [17], the interatomic potential for two atoms or ions containing a total of n electrons and separated by a distance r_{12}, is

$$V(r_{12}) = \frac{1}{2} \sum_{i \neq j=1}^{n} \frac{e^2}{r_{ij}} - \sum_{i=1}^{n} \left(\frac{Z_1 e^2}{r_{i1}} + \frac{Z_2 e^2}{r_{i2}}\right) + \frac{Z_1 Z_2 e^2}{r_{12}} \quad . \qquad (2.8)$$

It is not practical or even possible to solve the collision problem with such a potential form when n (the number of electrons) is large. However, the many-body problem has been treated for simple systems like He-He. The interatomic potential will be discussed later in a separate section, and it is sufficient now to consider V(r) as a simple screened Coulomb potential

$$V(r) = \frac{Z_1 Z_2 e^2}{r} \Phi \quad , \qquad (2.9)$$

where r is the distance of separation, and Φ is a screening function

which would include all the effects of the screening of the ion's and atom's electrons to the nuclear charges. The screening function Φ should approach unity when r goes to zero, i.e. for a very small distance of separation one has a simple Coulomb potential for the interaction of the two nuclei at the other extreme, Φ must vanish as $r \to \infty$.

Apparently the nuclear charge of the target atom is always completely screened by the atomic electrons at large distances, but as shown in Section (II-2), the screening of the ion is velocity dependent. For the velocity region $v > v_o Z$, i.e. for a completely stripped nucleus, and for a small distance of separation the unscreened Coulomb field would lead to a Rutherford scattering which is small. For $v_1 \leq v_o Z^{2/3}$ the screening of the ion's nuclear charge begins to take place. Thus, the screening function Φ should depend on the velocity. Despite this fact, and for the sake of simplicity, the screening functions are always considered to be that of <u>static</u> atom-atom interaction.

Bohr [1] suggested that Φ takes the simple form

$$\Phi = \exp\left(-\frac{r}{a}\right) \quad , \tag{2.10}$$

where a is the screening parameter or the screening length, given by

$$a = a_o \left(Z_1^{2/3} + Z_2^{2/3}\right)^{-1/2} \quad , \tag{2.11}$$

although some authors used empirical values of a up to three times the Bohr value [13]. This is because when $r > a$, the Bohr potential

decreases more rapidly than does the actual ion-atom interaction. Lindhard et al. [14] used Thomas-Fermi potential with the screening length, a, slightly different from Bohr's and given by

$$a = 0.8853\ a_o\ (Z_1^{2/3} + Z_2^{2/3})^{-1/2} \quad . \tag{2.12}$$

Firsov [15] on the other hand, used a screening length given by

$$a = 0.8853\ a_o\ (Z_1^{1/2} + Z_2^{1/2})^{-3/2} \quad . \tag{2.13}$$

It is convenient to introduce the collision diameter b, which is the distance of closest approach in a head-on collison for the case of Coulomb interaction, defined as

$$b = Z_1 Z_2 e^2 / (\tfrac{1}{2} M_o v_1^2) \quad , \tag{2.14}$$

where M_o is the reduced mass defined as

$$M_o = M_1 M_2 / (M_1 + M_2) \quad . \tag{2.15}$$

Bohr [1] used the ratio of b to the screening length a

$$\xi = b/a \quad , \tag{2.16}$$

as a measure of the degree of screening, while Lindhard et al. [14] used the inverse of the same ratio

$$\varepsilon = \frac{a}{b} = \frac{a}{Z_1 Z_2 e^2}\ \frac{1}{2} M_o v_1^2 \quad . \tag{2.17}$$

as a measure of the energy.

II-3-1. Applicability of Classical Mechanics

If we wish to apply the classical mechanics to the collision problem, two conditions must be satisfied [16]. The first is that the orbit of the particle must be well-defined in relation to distance, and the second is that the deflection due to the collision must be well defined. The first requires that the DeBroglie wavelength $\lambda\!\!\!^{-}$ of the particle should be less than the minimum dimension associated with the collision. A suitable choice of this distance is the collison diameter b. Thus,

$$\lambda\!\!\!^{-} = \frac{\hbar}{M_o v_1} << b \quad . \tag{2.18}$$

Defining

$$\chi = \frac{b}{\lambda\!\!\!^{-}} \quad , \tag{2.19}$$

Equation (2.17) becomes

$$\chi >> 1 \quad . \tag{2.20}$$

The second condition requires that, if Δp is the momentum transfer in the collision, one must have

$$b\Delta p >> \hbar \quad . \tag{2.21}$$

Δp is the order of $V(b)/v_1$, and hence we have

$$b\frac{V(b)}{v_1\hbar} >> 1 \quad . \tag{2.22}$$

In terms of the angle of scattering θ, which is of the order $V(b)/M_o v^2$, this condition can be written as $\theta \gg \hbar/mva$. Since θ is of the order of unity, and in case of Coulomb interaction, the first condition, Eq. (2.20), is a necessary and sufficient condition for using classical mechanics, leading to Rutherford scattering [1].

For the case of minimum screening, i.e. $\xi \ll 1$, $\varepsilon \gg 1$, or minimum distance of separation, and when condition (2.20) is satisfied, classical mechanics can be applied and leads to Rutherford scattering for all angles larger than a minimum angle. This minimum angle corresponds to an impact parameter in the order of the screening length and is given by Bohr [1] to be

$$\theta_{min} \approx \xi = \frac{Z_1 Z_2 e^2}{M_o v_1^2 a} \quad , \tag{2.23}$$

and by Mott and Massey [16] as

$$\theta_{min} = \frac{3.8\ Z_2^{4/3}\ e^2}{M_o v^2 a_o} \quad . \tag{2.24}$$

If Eq. (2.20) is not fulfilled, i.e. when $\lambda\!\!\!^{-} > b$ and still $\xi \ll 1$, i.e. $(b \ll a)$, the Born approximation can be used and there will be a region of scattering angles confined to Rutherford scattering with a minimum angle given by

$$\theta_{min} = \frac{\lambda\!\!\!^{-}}{a} \quad , \qquad \text{(Bohr)}$$

and (2.25)

$$\theta_{min} = 2.1\ Z_2^{1/3}\ \hbar/(M_o v_1 a_o) \quad . \qquad \text{(Mott and Massey)}$$

In the case of excessive screening, i.e. $b > a$, condition (2.20) would not be sufficient for the classical mechanics to be applied, and we require $\lambda << a$ rather than $\lambda << b$. In this case, it would be impossible to trace angles smaller than

$$\theta_{min} \approx \frac{\lambda}{a} = \frac{\xi}{\chi} \quad , \tag{2.26}$$

and the scattering will be essentially different from that in the unscreened fields. The scattering then tends towards a spherically symmetrical angular distribution. Thus the condition for classical mechanics to be applied in this case is $\theta_{min} << 1$. From Eq. (2.26), this implies that

$$\chi >> \xi \quad . \tag{2.27}$$

When $\lambda > a$, the quantum mechanics treatment should be used. However, there exists a region where the Born approximation can still be used where $\chi < \lambda/2a$ or

$$\chi << \sqrt{\xi} \quad . \tag{2.28}$$

The criteria specified are best illustrated in Fig. 2-2 where a schematic diagram represents the different cases. Also, Fig. 2-3 shows the different regions in terms of χ and ξ.

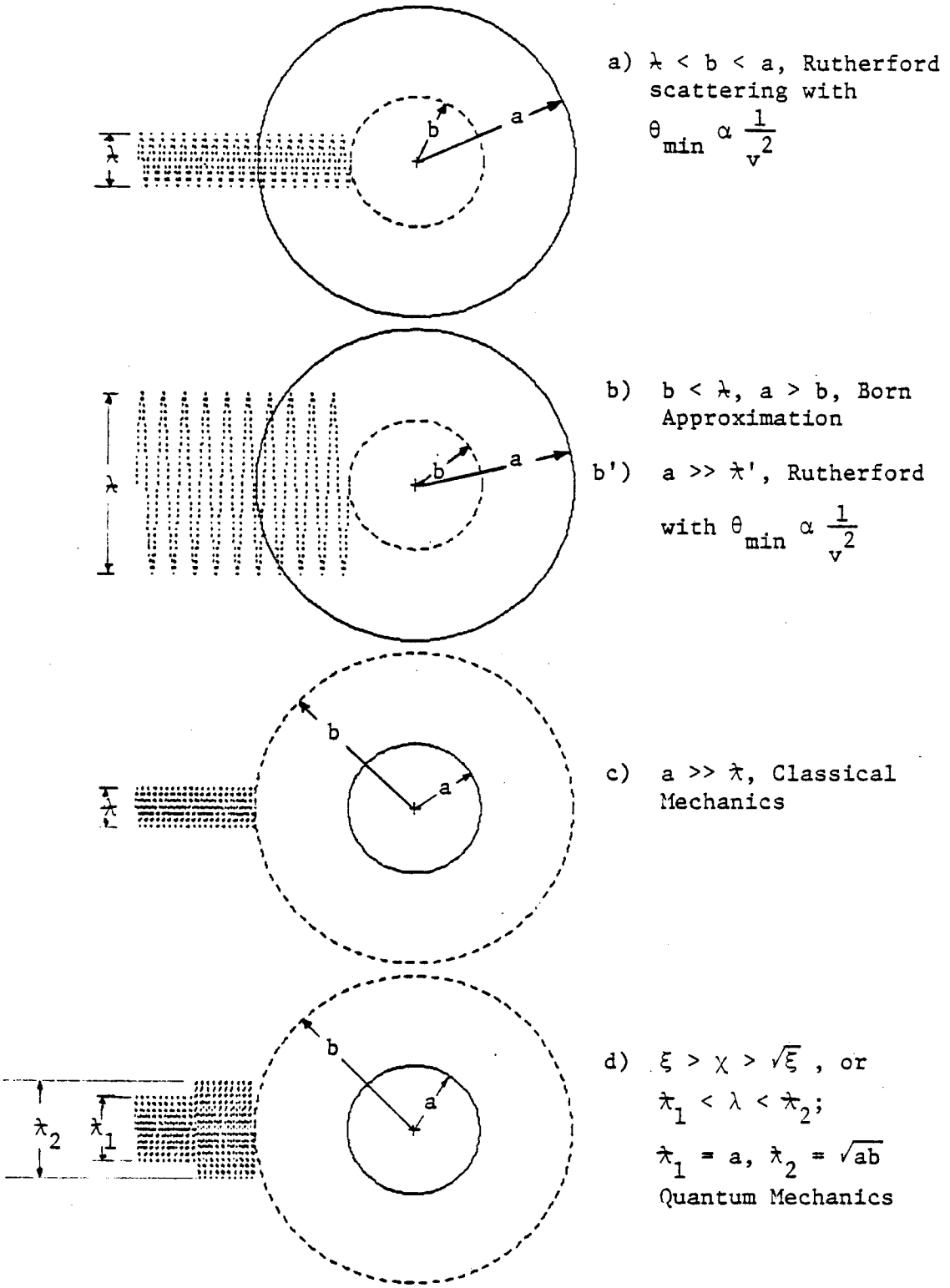

Fig. 2-2. Schematic diagram of the relationship between the collision diameter b, the screening length a, and the wave length ƛ.

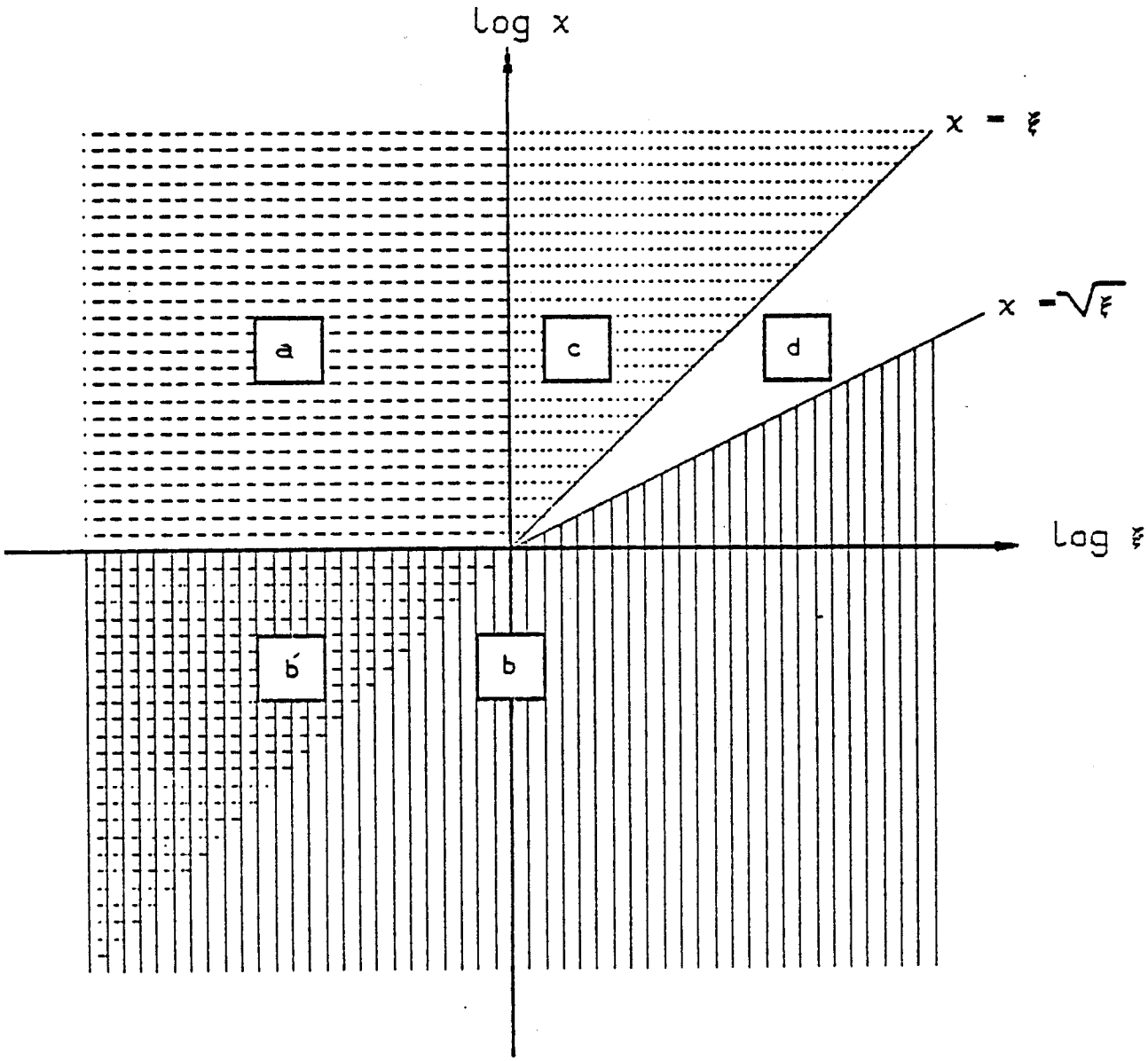

Fig 2-3. Schematic diagram showing the regions where the classical mechanics can be applied (horizontal hatching, c, a, b'). in terms of $\chi = \frac{b}{\lambda}$ and $\xi = \frac{b}{a}$, and where the simplified wave scattering (Born Approximation, vertical hatching b, b') can be used. The region d is where the quantum mechanics should be applied.

II-3-2. The Interatomic Potential

Unfortunately there is no single analytical expression for interatomic potential that can precisely describe the interaction between ions and/or atoms along all distances of separation between them. Because the subject of the interatomic potential is so relevant to many fields of study, one can find a large number of approximate formulae that have been devised to describe it. An extensive review for the theories and the approximations associated with these formulae has been made by Torrens [17].

The aproximation of the many-body interaction described in Eq. (2.8) by a simple central two-body potential, like Bohr potential (Eq. 2.9 and Eq. 2.10), can be justified in cases of large or very small distances of separation, i.e. when nucleus-nucleus interaction is predominant. In the case of intermediate distances of separation, when some degree of merging between the two particles' electrons occurs, the approximation is not as good.

The nature of the interaction between ions and/or atoms can be described qualitatively as follows. For high energy atomic collisions and small distances of separation the nuclear-nuclear repulsion plays the major role. If the atoms are just "touching", the nuclear repulsion is negligible compared to the interaction between the electron clouds. If the atoms are ionized, the interaction can be treated as if the ions are charges. For large separations, the interaction depends on the host medium. In a vacuum it arises from the polarizations that take place between the two atoms. In metals

the separated ions interact via the intervening electron charge clouds.

If the electron clouds are overlapping, a short range interaction arises due to the Pauli principle. In this case, as was mentioned previously, it is impossible to solve the collision problem accurately, and substantial approximations are required. In such cases, various approximate atomic models are combined with experimental data to yield reasonable pair-wise interatomic potentials in some ranges of atomic separation. Figure 2-4 shows a schematic diagram of a typical two-body interatomic potential. It should be mentioned that there is also a large amount of experimental data for the region of $r >> r_o$ and for the nuclear repulsion region, i.e. $r << r_o$, but there is a lack of information in the region between these two extremes. In this region the potential is constructed by extrapolation of either the high energy or equilibrium potentials.

Many of the existing forms of interatomic potentials have been theoretically based on the Thomas-Fermi model of the atom. In this model the atomic systems consist of one or more Coulomb nuclei, surrounded by an electron gas of variable density which is considered uniform on the microscopic scale [18]. The potential of a neutral atom in this model with charge number Z is given by

$$V(r) = \frac{Ze}{r} \Phi (r/a) \quad , \tag{2.29}$$

with

$$a = 0.8853 \, a_o \, Z^{-1/3} \quad , \tag{2.30}$$

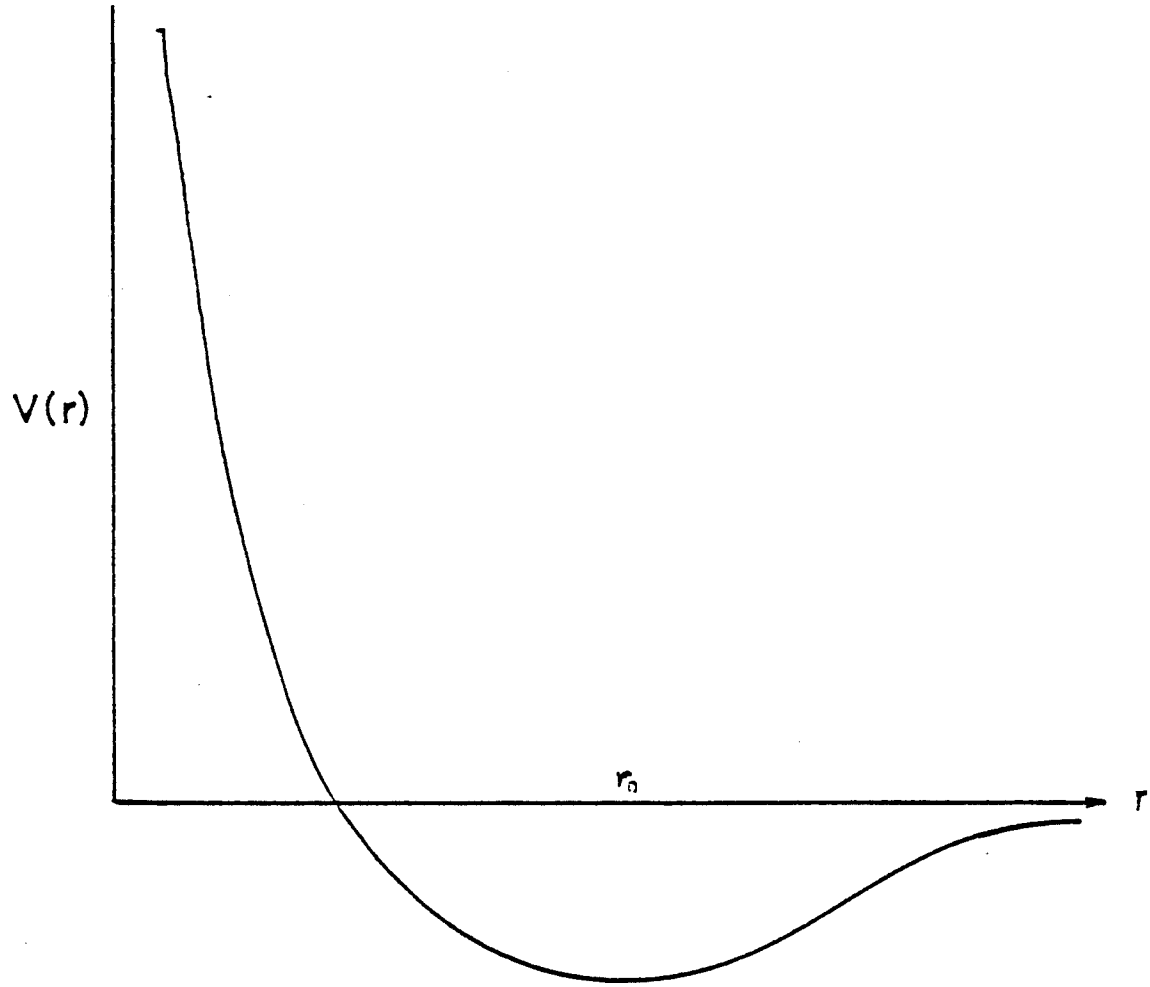

Fig. 2-4. Schematic representation of a simple interatomic two-body, potential.

and Φ (r/a) is the solution of the nonlinear differential equation

$$\frac{d^2\chi}{dx^2} = \chi^{3/2}/x^{1/2} \quad , \tag{2.31}$$

with χ = r/a, and with boundary conditions

$$\chi(0) = 1 \quad , \quad \chi(\infty) = \chi'(\infty) = 0 \quad , \tag{2.32}$$

where $\chi' = d\chi/dx$. The screening function Φ (r/a) can be approximated by [18]

$$\Phi \simeq 1 - 5.88\ x \quad , \quad \text{(for small x)} \quad ,$$
$$\text{and} \tag{2.33}$$
$$\Phi \simeq 144/x^3 \quad \text{(for large x)} \quad .$$

Numerous extensions have been applied to TF models of the atom because of the multitude of ways that the electron gas can be described. Also there are many analytical approximations to the approximate screening function Φ. Table 2-1 lists some of these approximate solutions [17]. Although TF potential describes the potential of a neutral atom it has been extended by Lindhard et al. [8] and Firsov [15] to describe the interaction between atoms or ions. Their results differ only in the choice of the screening parameter a (Eqs. 2.12 and 2.13). The screening functions based on either Lindhard or Firsov estimate of the screening length differ by 10%, i.e. they agree within the accuracy of TF approach.

There exist families of potential forms which are based on simple analytical expressions that may or may not be justified from

Table 2-1. [17]

Analytical Solutions of the TF Equation.

(All references are that of Ref. [17].)

Author	Analytical expression for the screening function $\Phi(x)$, $(x = r/a)$
1. Sommerfeld [20]	$\left[1 + \left(\frac{x}{12^{2/3}}\right)^{\lambda}\right]^{-3/\lambda}$ $\lambda = 0.772$ (Sommerfeld [20]) $\lambda = 0.8034$ (March [21]) $\lambda = 0.8371$ (Umeda [22])
2. Kerner [24]	$(1 + Bx)^{-1}$ $B = 1.3501$ (Kerner [24]) $B = 1.3679$ (Umeda [22])
3. Brinkman [25]	$Cx^{1/2}K_1(2Ax^{1/2})$
4. Tietz [26]	$(1 + (B/6^{1/2}) \cdot x)^{-2}$
5. Rozental [28]	$0.7345e^{-0.562x} + 0.2655e^{-3.392x}$
6. Rozental [28]	$0.255e^{-.0246x} + 0.581e^{-0.947x} + 0.164e^{-4.356x}$
7. Moliere [29]	$0.35e^{-0.3x} + 0.55e^{-1.2x} + 0.10e^{-6.0x}$
8. Csavinsky [30]	$(0.7111e^{-0.175x} + 0.2889e^{-1.6625x})^2$
9. Roberts [31,32]	$(1 + 1.7822x^{1/2})\ \exp\ [-1.7822x^{1/2}]$
10. Wedepohl [33]	$317x\ \exp\ [-6.62x^{1/4}]$
11. Lindhard [23]	$1 - x/(3 + x^2)^{1/2}$
12. Lindhard [23]	$1 - 1/2x$

theory, and which contain one or more parameters adjusted to experimental information. Some of these potentials are: the simple hard sphere potential, the square well potential and the following more realistic potentials:

i) Lennard-Jones Potential,

$$V(r) = \ell_n/r^n - \ell_m/r^m \quad , \tag{2.34}$$

ii) Morse Potential,

$$V(r) = D \exp(-2\alpha (r - r_o)) - 2D \exp(-\alpha (r - r_o)) \quad , \tag{2.35}$$

iii) Buckingham Potential,

$$V(r) = A \exp(-Br) - \ell/r^6 - \ell'/r^8 \quad . \tag{2.36}$$

All these potentials can be described schematically as in Fig. 2.4. They are repulsive at small r then decrease to an attractive minimum, then approach zero at very large r. Thus, they may describe potentials between atoms in equilibrium or for very low energy.

iv) Born-Mayer Potential,

$$V(r) = A \exp(-Br) \quad , \tag{2.37}$$

which may be valid only for a very small overlap of the closed shell since it does not contain a nuclear repulsion. The constants A and B are determined from the compressibility data. This potential can be used for energies less than the parameter A.

For high energies, the above mentioned potentials are usually inaccurate and other potentials are needed. Due to lack of experimental data in the high energy range of interest, different potentials, based on pure theoretical considerations, have been introduced. It should be mentioned that for energies above few electron

volts, the attractive part of the potential is of no importance and can be neglected.

Figure 2-5 shows the screening functions of some of the potentials mentioned above. The Thomas-Fermi potential (Eq. 2.29) describes the interaction at small distances of separation fairly well, but for larger separations it decays too slowly. A more accurate choice is the Moliere potential (Table 2-1) which decays more rapidly. Figure 2-6 shows the potentials of Thomas-Fermi, Born-Mayer, and Bohr compared to Coulomb potential. Figure 2-7 shows Thomas-Fermi screening function and different approximations by the inverse powers potential, $V(r) \alpha r^{-s}$ which has a screening function given by

$$\Phi\ (r/a) = \frac{\kappa_s}{s}\ (a/r)^{s-1} \quad . \tag{2.38}$$

where κ_s is a constant.

It should be mentioned that there are several sources of inaccuracy and uncertainty in the interatomic potential which are introduced by ionization or excitation of the atoms in collision. Most of these uncertainties cannot be taken into consideration in any of the above mentioned potentials.

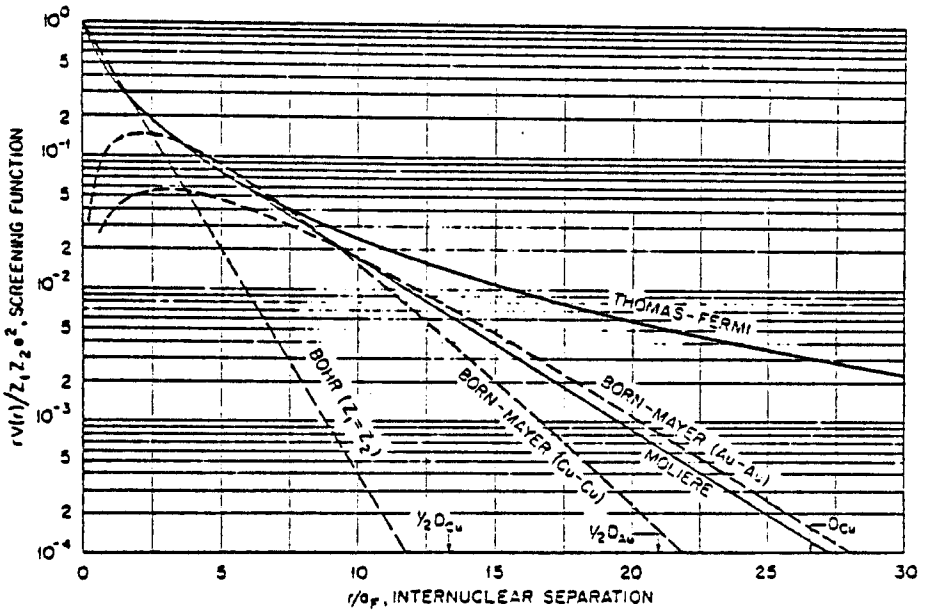

Fig. 2-5. Screening functions of Moliere, Thomas-Fermi, Bohr potentials and related functions for Cu-Cu and Au-Au BM potentials. The unit of distance is the Firsov screening length a_F; D represents the nearest-neighbor distance in the lattice [17].

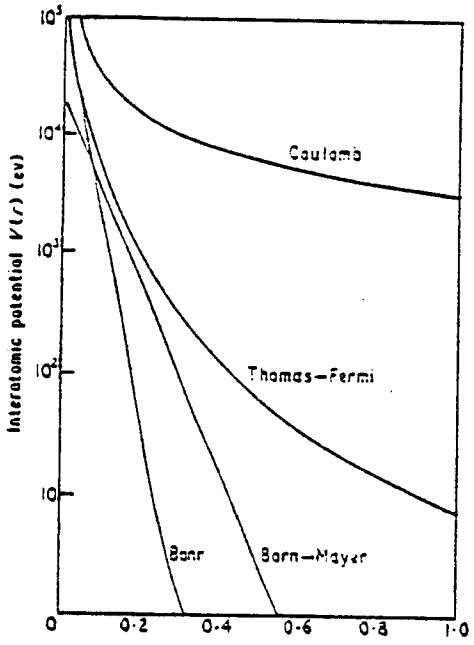

Fig. 2-6. Several commonly used approximations to the interatomic potential.

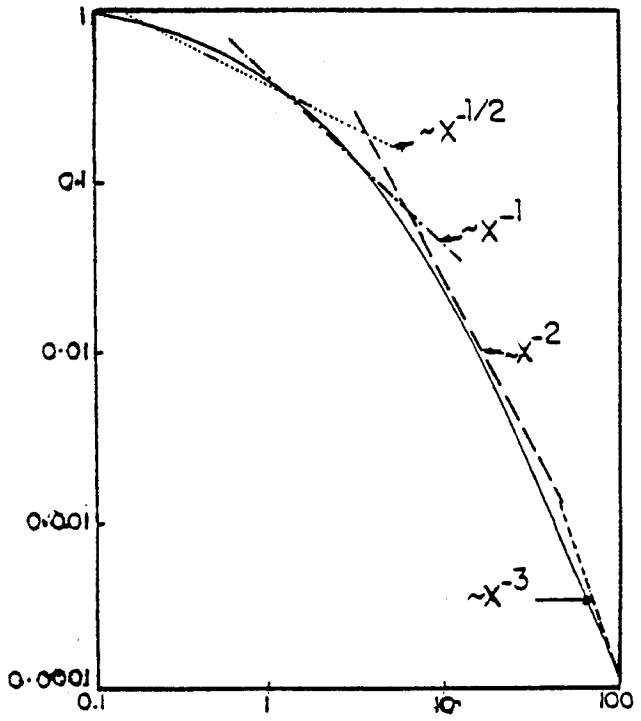

Fig. 2-7. Thomas-Fermi screening function and different approximations by inverse powers.

II-3-3. Scattering Cross Section

If we know the potential V(r), the impact parameter p, and energy of the incident particle E, then the scattering angle in the relative coordinate system can be determined. Thus,

$$\theta = \Theta\,(p, V(r), v_1, M_o) \quad , \tag{2.39}$$

where v_1 is the velocity of the incident particle, M_o is the reduced mass given by Eq. (2.15).

The differential cross section $d\sigma$ is defined as

$$\begin{aligned} d\sigma &= 2\pi p\, dp \\ &= 2\pi p \frac{dp}{d\theta}\, d\theta \quad , \end{aligned} \tag{2.40}$$

and with the information in Eq. (2.39), $d\sigma$ could be evaluated. Since the energy transfer is related to the scattering angle via

$$T = T_m \sin^2 \theta/2 \quad , \tag{2.41}$$

where T_m is the maximum energy transfer in the collision and equals

$$T_m = \frac{4\, M_1 M_2}{(M_1 + M_2)^2} E \quad , \tag{2.42}$$

the scattering cross section $d\sigma$ can also be stated as

$$d\sigma = \frac{d\sigma}{dT}\, dT \quad . \tag{2.43}$$

Lindhard et al. [8] obtained an approximate representation for the differential scattering cross section from the inverse power potential (Eq. 2.38). For this potential the differential scattering cross section is

$$d\sigma\ (T) = \frac{C_n}{T_{max}^{1-1/s}} \frac{dT}{T^{(1+1/s)}} \quad , \qquad \text{for } s > 1 \tag{2.44}$$

where

$$C_n \approx (1 - \frac{1}{s}) \frac{\pi^2}{2.718} \frac{e^2 a_o Z_1 Z_2 M_1}{(Z_1^{2/3} + Z_2^{2/3})^{1/2} (M_1 + M_2)} \quad . \tag{2.45}$$

If the TF potential is used, Lindhard et al. [8] showed that the differential cross section can be written as

$$d\sigma = \frac{1}{2} \pi a^2 \ t^{1/2} \ f(t^{1/2}) \ dt \quad , \tag{2.46}$$

where $t = \varepsilon^2 \sin^2 \theta/2$, ε is the reduced energy (defined in Eq. 2.15) and the function $f(t^{1/2})$ has been evaluated numerically by Lindhard et al. [8].

An approximate interpolated formula for $f(t^{1/2})$ used by Winterbon et al. [19] is

$$f(t^{1/2}) = \lambda t^{1/6} \ [1 + (2\lambda t^{2/3})^{2/3}]^{-3/2} \tag{2.47}$$

where $\lambda = 1.309$.

Figure 2-8 shows the function $f(t^{1/2})$ for the TF potential produced by Eq. (2.47) and that originally given by Lindhard. Another form of the function $f(t^{1/2})$ which can fit some of the potentials mentioned earlier is

$$f(t^{1/2}) = \lambda t^{1/2-m} \ (1 + (2\lambda t^{1-m})^q)^{-1/q} \quad , \tag{2.48}$$

where λ, m, and q are constants given in Table 2-2 for different potentials [20].

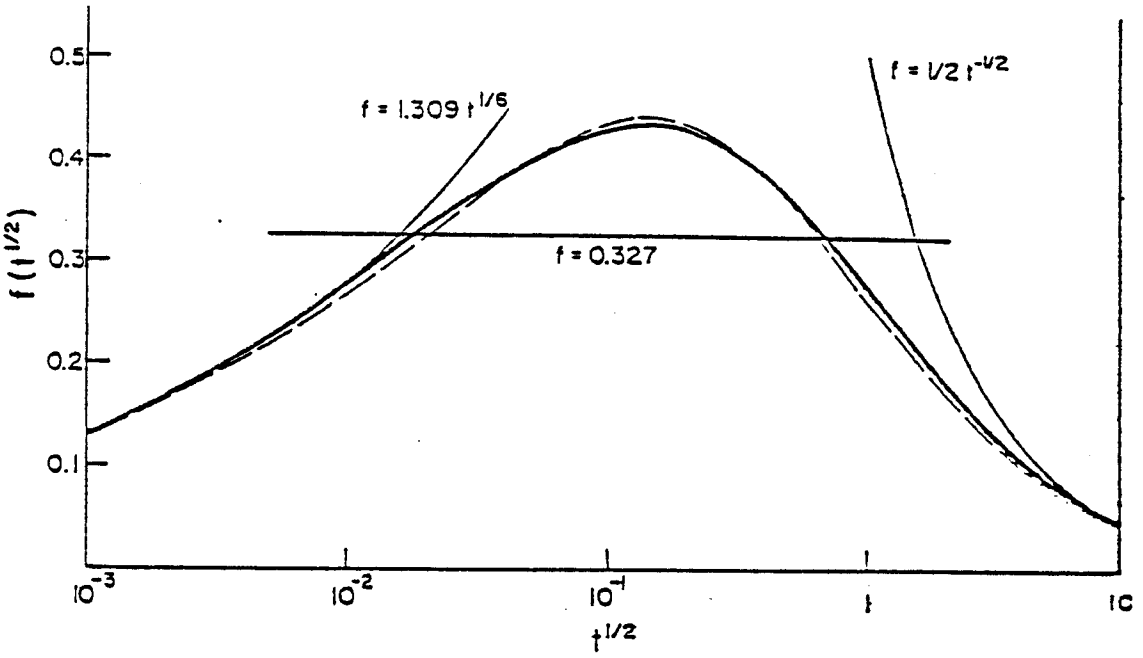

Fig. 2-8. Reduced differential cross sections from TF potential. Thick solid line: Lindhard's numerical result. Dashed line: Eq. (2.47). Thin solid lines: power cross section (Eq. 2.44). [19]

Table 2-2.

The Constants λ, m, and q for Different Potentials [24]

	λ	m	q
1. Thomas-Fermi-Sommerfeld	1.70	0.311	0.588
2. Bohr	2.37	0.103	0.570
3. Lenz-Jensen	2.92	0.191	0.512
4. Lindhard, $c^2 = 1.8$	0.625	0.333	1.24
5. Lindhard, $c^2 = 3$	0.879	0.333	1.24
6. Moliere	3.07	0.216	0.530
7. Thomas-Fermi [21]	3.3498	0.216	0.530

References for Chapter II

1. N. Bohr, Mat. Fys. Medd. Dan. Vid. Selsk. 18, No. 8 (1948).

2. M. T. Robinson, Proc. of Int. Conf. on "Radiation-Induced Voids in Metals," ed. J. W. Corbett and L. C. Ianniells, Albany, NY, June 1971, CONF-710601, 397 (1972).

3. H. A. Bethe, Z. F. Physik 76, 293 (1932); F. Bloch, Z. F. Physik 81, 363 (1933).

4. J. F. Ziegler and G. J. Iafrate, Rad. Eff. 46, 199 (1980).

5. W. Brandt, Proc. of the Int. Conf. on Atomic Collision in Solids, 5th, Gatlinburg, Tenn., 1973, ed. S. Datz, B. R. Appleton, and C. D. Moak, Plenum Press, NY, p. 261 (1975).

6. L. C. Northcliffe, Phys. Rev. 120, 1744 (1961).

7. M. T. Robinson, Consultant Symposium on the Physics of Irradiation Produced Voids, ed. Nelson, Harsell, U.K., 1974, AERE-R7934, p. 18 (1975).

8. J. Lindhard and M. Scharff, Phys. Rev. 124, 128 (1961).

9. O. B. Firsov, Zb. Eksp. Teor. Fiz. 36, 1517 (1959), [Soviet Phys. JETP 36, 1776 (1959)].

10. C. P. Bhalla, J. N. Bradford, and G. Reese, in Atomic Collision Phenomena in Solids, p. 361, ed. D. W. Palmer, M. W. Thompson, and P. D. Townsend, North-Holland, Amsterdam (1970).

11. D. K. Brice, Phys. Rev. 6, 1971 (1972).

12. L. C. Northcliffe and R. F. Schilling, Nucl. Data 7, 233 (1970).

13. G. Dearnaley, J. H. Freeman, R. S. Nelson, and J. Stephen, Ion Implantation, North-Holland, Amsterdam (1973).

14. J. Lindhard, M. Scharff, and H. E. Schiott, Mat. Fys. Medd. Dan. Vid. Selsk. 36, No. 10 (1968).

15. O. B. Firsov, Zb. Eksp. Teor. Fiz. 33, 696 (1957), [Soviet Phys. JETP 6, 534 (1958)].

16. N. F. Mott and H. S. W. Massey, "The Theory of Atomic Collisions," 3rd ed., Oxford University Press, London (1965).

17. I. M. Torrens, "Interatomic Potentials," Academic Press, NY (1972).

18. P. Sigmund, Rev. Roum. Phys. 17, 823, 962, and 1079 (1972).

19. K. B. Winterbon, P. Sigmund, and J. B. Sanders, Mat. Fys. Medd. Dan. Vid. Selsk. 37, No. 14 (1970).

20. K. B. Winterbon, Rad. Eff. 13, 215 (1972).

21. J. B. Biersack, private communication.

CHAPTER III

ION TRANSPORT

III-1. Introduction

There are two main functions of interest in any radiation damage study using ion bombardment techniques. The first is the penetration distribution function, which gives the spatial distribution of the ions after they come to rest in the target material. The second is the deposited energy distribution function, which describes the spatial distribution of the deposited energy in the material. If we consider a single ion history, we find that after the ion has penetrated the target surface, it may suffer a collision with a target atom at or close to the surface and will be deflected into a new direction. During its penetration the ion loses energy through electronic ionization and excitation. At the collision point, the amount of energy lost in collision will depend on the ion energy, the impact parameter with target atom at that point, and the interaction potential with this atom. The collision is generally inelastic, i.e. energy may be dissipated in excitation and ionization of the target atom during the collision itself. On its new trajectory, the ion may travel some distance, while losing energy to electrons before it encounters another target atom, again suffering a collision, some energy loss, and is deflected. This process is continued until the ion, which henceforth will be called the primary, no longer has enough energy to surmount the potential energy barriers offered by the target atoms. If this history is repeated with the same initial

conditions, the trajectory of the new primary may be different. Figure 3-1 shows two possible histories of a single primary.

For a large number of histories one can expect that the end points of the trajectories will have some spatial distribution, which is the penetration distribution function mentioned previously. Clearly all the information necessary to get this function can be obtained from the end points of the trajectories.

The deposited energy distribution functions, e.g. the nuclear energy loss or the electronic energy loss, are obtained along all the trajectories. To predict these distribution functions theoretically, some assumptions have to be made to get tractable solutions. These assumptions are discussed below.

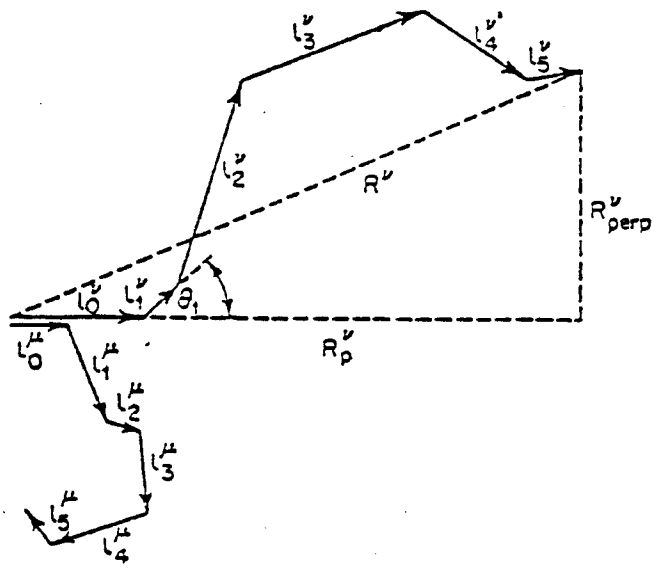

Fig. 3-1. The possible paths of two ions broken up into linear segments.

III-2. Assumptions of Theoretical Methods

Before reviewing the theoretical methods it is important to spell out the general approximations and assumptions which are usually used. These assumptions are:

(a) Homogeneity and infiniteness of the target.

These assumptions allow for integration over the space to reduce the number of variables in the equations governing the distribution function and its moments. These are basic assumptions in almost all analytical approaches except for the work of Williams [29] and Winterborn [31], where in some limited cases, the ion transport is considered in multi-layer targets.

(b) No allowance for damage overlap.

Damage caused by collisions between ions and lattice atoms will be in the form of atoms displaced from their normal lattice sites which, in turn, result in the formation of vacancies and interstitials. The displaced atoms, PKAs, may produce more damage. Damage is also caused by the ions themselves as interstitials after they come to rest in the lattice. The damage according to this assumption is additive, i.e. we consider the material for each ion as defect free with no account made for the damage caused by any preceding ions. The damage is then summed to constitute the overall damage in the material. However, the presence of vacancies, interstitials, and deposited ions will affect the trajectories of any subsequent injection of ions. This approach is justified by the assumption that

prior damage effect will not be important until an extremely large number of ions have entered the lattice, or for high dpa values.

(c) No annealing effect.

Some of the damage produced may be annealed out due to recombination of interstitials and vacancies, but this is difficult to treat theoretically because it requires a knowledge of the exact position of previously produced defects in relation to the trajectory of the injected ions.

(d) Randomization of the lattice.

All of the theoretical methods assume random lattices or amorphous solids. No account is made for the arrangement of the lattice atoms in solids, i.e. the lattice effects, channeling and focusing, are ignored.

The effect of channeling can be ignored for ion implantation along low-index directions in a crystalline target. Moreover, ion implantation for sufficient doses will produce enough defects to disrupt the crystallinity of the lattice, rendering it "semi-amorphous". Figure 3-2 shows a highly ordered Cu-Pd target before and after irradiation with Cu ions up to only 0.25 dpa. Apparently, irradiation has destroyed the long range order of the target.

(e) Mean free path assumption.

The use of the mean free path assumption in the kinetic theory of gases is justified since, in gases, there are large distances of separation between the gas atoms, compared to the small distance of influence at which interatomic forces play a role. In solids, how-

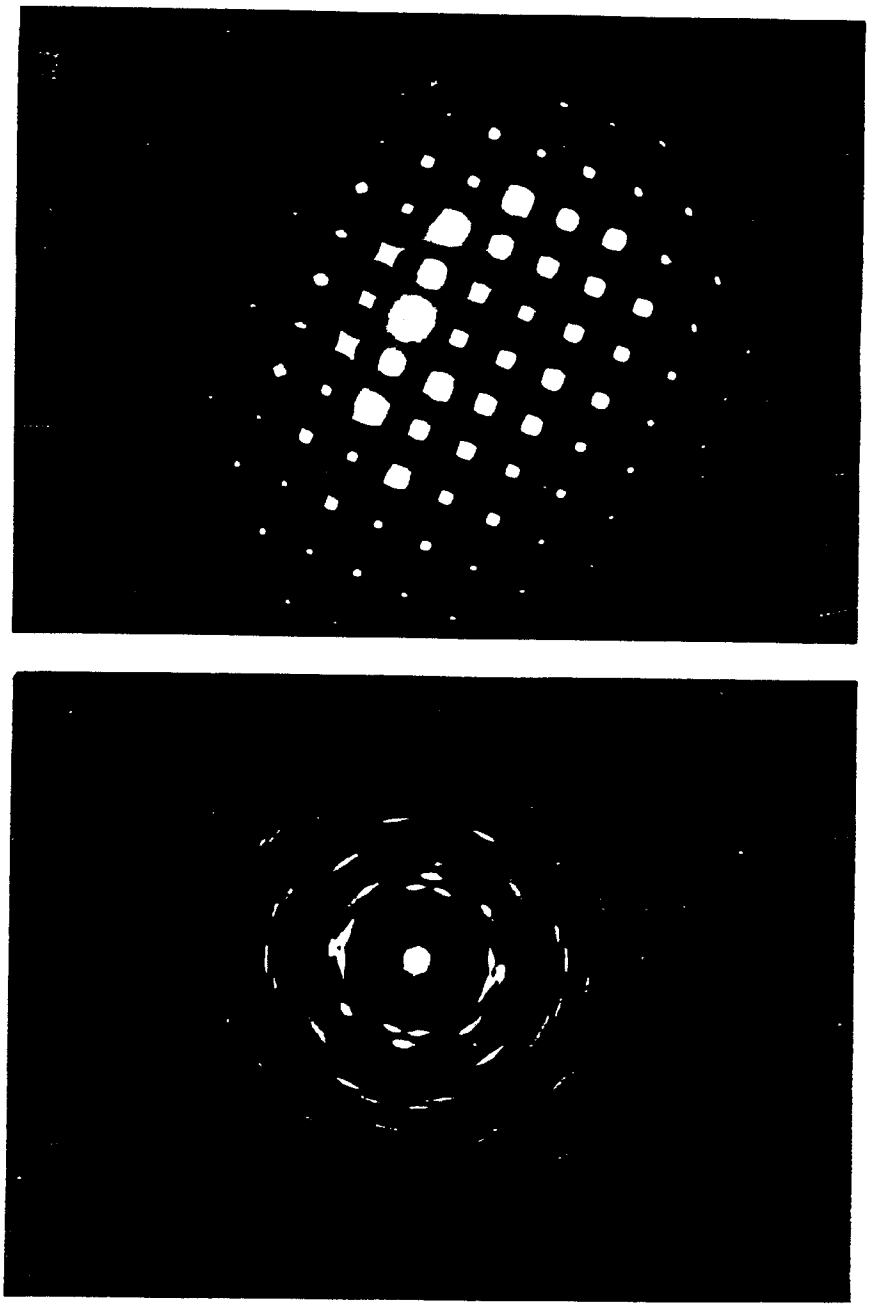

Fig. 3-2. The diffraction pattern of Cu-Pd before (Top) and after (bottom) irradiation with Cu for .25 dpa. The diffuse rings in the lower diffraction pattern indicate that irradiation has eliminated the long range order of the target.

ever, due to the smaller distance of separation between atoms, the interatomic forces affect the primary before, during and after the collision with any lattice atom. If $\sigma(E)$ is the total collision cross section and N is the atomic density then the average distance between collisions is given by

$$\lambda(E) = 1/(N\sigma(E)) \quad , \tag{3.1}$$

with the probability of having a path length between ℓ and $\ell + d\ell$ given by

$$P(\ell)\, d\ell = \frac{1}{\lambda(E)} \exp\left(-\frac{\ell}{\lambda(E)}\right) d\ell \quad . \tag{3.2}$$

With these equations, the length of the segments of the path, shown in Fig. 3-1, can be obtained.

(f) Two-body collision approximation.

As was mentioned in Chapter II, it is difficult to handle the real interaction of the primary, or any moving atom, with the lattice atoms when it is a many-body interaction in nature. However, due to the fact that the interaction force decreases rapidly when the distance of approach is beyond the order of an atomic diameter, this assumption is probably reasonable. For very low energy interaction, the cross section becomes large so that the moving atom interacts with more than one target atom simultaneously. The energy limit below which the many-body effects become of importance can be estimated by equating the velocity of the longitudinal sound waves in the solid to the velocity of the moving atom [1]. This energy limit

ranges from 5.5 eV for aluminum in aluminum to 28.4 eV for tungsten in tungsten. Such energies are less than the displacement threshold.

(g) Separation of nuclear and electronic interactions.

This assumption has been discussed in detail in the previous chapter.

(h) Continuous electronic stopping approximation.

The use of the Lindhard [2] or Firsov [3] formulae for the electronic stopping introduces all the inherent approximations of these formulae [4]. Unfortunately, experimental results show that these formulae do not have the correct dependence on the ion velocity, nor on the charges of the ion and the target atoms [4].

III-3. Specific Energy Loss Method - LSS Theory [5]

III-3-1. Range Distribution

With all the approximations mentioned in the previous section, Lindhard, Scharff, and Schiott [5] made a further assumption that the slowing down of the moving atom (ion or atom) is continuous. In this assumption, the primary loses its energy continuously along its path. Thus, the average energy loss per unit path length is equal to the average energy loss per collision times the average number of collisions per unit path. The first quantity is given by

$$T = 1/\sigma \int_0^{T_m} T \, d\sigma \, (T) \quad , \tag{3.3}$$

where: σ = total collision cross section,

T = energy transferred to the struck atom,

$d\sigma(T)$ = differential scattering cross section for energy transfer T,

and T_m = maximum energy transfer in the collision.

The average number of collisions per unit path length, using Eq. (3.1) is

$$1/\lambda = N\sigma(E) \quad . \tag{3.4}$$

Therefore,

$$dE/dR = N \int d\sigma\, T = NS \quad , \tag{3.5}$$

where $S = \int d\sigma\, T$ = stopping cross section per scattering center. The range is then obtained by integrating dE/dR to get

$$R(E) = \int_0^E dE'/(dE'/dR) = 1/N \int_0^E dE'/S(E') \quad . \tag{3.6}$$

The energy straggling in dR is given by

$$\overline{(\Delta E^2)} = N\, dR \int d\sigma\, T^2 = N\, dR\, \Omega^2 \quad . \tag{3.7}$$

The range straggling is related to $\overline{(\Delta E^2)}$ via

$$\begin{aligned} \overline{(\Delta R^2)} &= \overline{\Delta E^2}\,(dR/dE)^2 = N\, dR\, \Omega^2\,(dR/dE)^2 \\ &= N\Omega^2\, dE\,(dR/dE)^3 \quad . \end{aligned} \tag{3.8}$$

The straggling in the total path length is then given by

$$\begin{aligned} \overline{\Delta R^2} &= \int_0^E dE'\, N\, \Omega^2(E')(dR/dE')^3 \\ &= \int dE'\, \Omega^2(E')/(N^2 S^3(E')) \quad . \end{aligned} \tag{3.9}$$

We then introduce the reduced energy and the reduced range, given by

$$\varepsilon = EaM_2/[Z_1Z_2e^2(M_1 + M_2)] \quad ,$$

and (3.10)

$$\rho = RNM_2\ 4\pi a^2\ M_1/(M_1 + M_2)^2 \quad ,$$

where M_1, Z_1, M_2, and Z_2 are mass and charge of the primary and the target, respectively, and a = Thomas-Fermi screening radius given by

$$a = a_o\ .8853\ (Z_1^{2/3} + Z_2^{2/3})^{-1/2} \quad ,$$

a_o = Bohr radius = $\hbar^2/e^2m_e$ = 0.529 x 10^{-8} cm,

m_e = electron mass,

and e = electron charge.

With this notation, one obtains the universal differential cross section

$$d\sigma = 0.5\pi a^2\ t^{-3/2}\ f(t^{1/2})\ dt \quad , \tag{3.11}$$

where $t^{1/2}$ equals $\varepsilon \sin \theta/2$ and θ equals the deflection angle in the center of mass system. The function $f(t^{1/2})$ is shown in Fig. 3-3, for Thomas-Fermi potential and for a $(1/r^2)$ potential.

The nuclear stopping cross section, then, can be given by

$$(d\varepsilon/d\rho)_n = f(x)\ \varepsilon^{-1}\ dx \quad , \tag{3.12}$$

where $x = \varepsilon \sin(\theta/2)$. The electronic stopping cross section [2] can be written in ε and ρ units as

$$(d\varepsilon/d\rho)_e = K\varepsilon^{1/2} \quad , \tag{3.13}$$

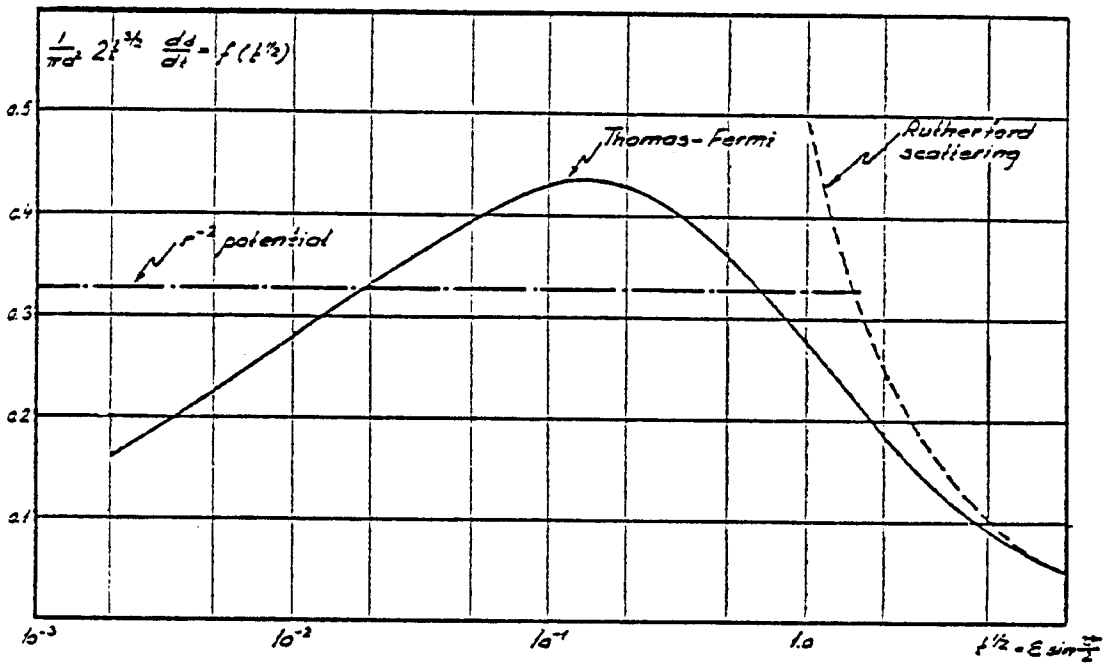

Fig. 3-3. The universal scattering function $f(t^{1/2})$ defined by Lindhard et al. [5].

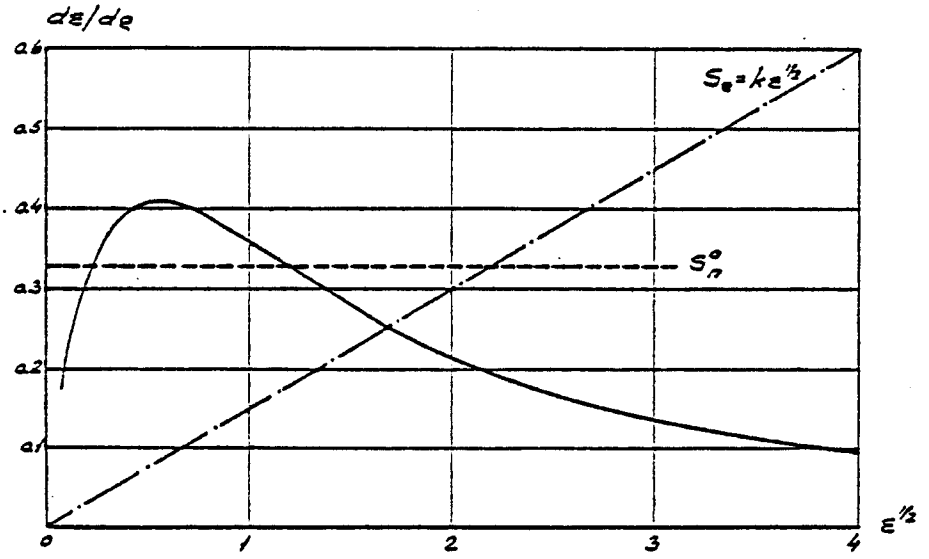

Fig. 3-4. The reduced nuclear and electronic specific energy loss as a function of energy [5].

where

$$K = \frac{\xi_e \; 0.973 \; Z_1^{1/2} \; Z_2^{1/2} \; (A_1 + A_2)^{3/2}}{(Z_1^{2/3} + Z_2^{2/3})^{3/4} \; A_1^{3/2} \; A_2^{1/2}} \quad ,$$

with A_1 and A_2 being the mass numbers for the primary and the target atoms, respectively, and ξ_e is a constant of the order of $Z_1^{1/6}$. Figure 3-4 shows S_e and S_n for k = 0.15.

If we take the effect of both nuclear and electronic stopping we get the total stopping

$$d\varepsilon/d\rho = (d\varepsilon/d\rho)_n + K\varepsilon^{1/2} \quad . \tag{3.14}$$

A numerical solution for the range ρ is shown in Fig. 3-5.

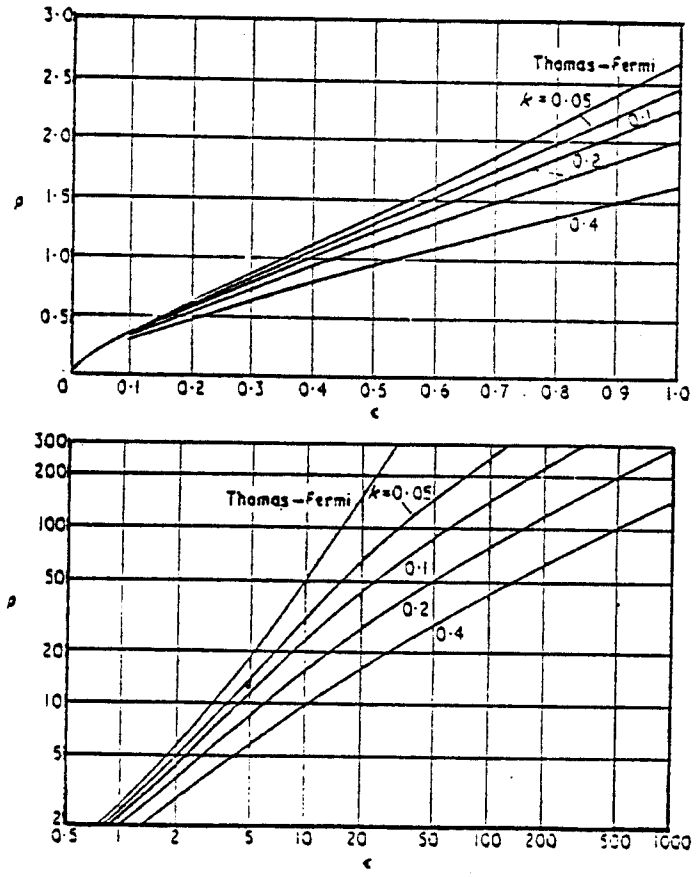

Fig. 3-5. Reduced range-energy plots for various values of the electronic parameter k [5].

To account for large fluctuations in ranges, the range distribution function p(R,E) dR, which specifies the probabilitiy of primaries with initial energy E reaching the path lengths between R and R + dR, is introduced. The function p(R,E) satisfies the following equations:

$$\int p(R,E)\, dR = 1 \quad , \quad \langle R^m \rangle = \int R^m\, p(R,E)\, dR \quad , \tag{3.15}$$

and

$$\partial p(R,E)/\partial R = \int N\, d\sigma_{n,e}\, [p(R,E-T_n-\Sigma_i T_{ei}) - p(R,E)] \quad , \tag{3.16}$$

where $\langle R^m \rangle$ is the m^{th} moment of the distribution p(R,E), and $d\sigma_{n,e}$ is the differential cross section for energy transfer T_n to struck atom and $\sum_i T_{ei}$ to electrons.

Equation (3.16) has been obtained from a simple and general argument. Consider the trajectories of many particles all at the start of their slowing-down process. Their range distribution is p(E,R). Let all the particles travel a small path length segment δR. Some of the particles may have undergone a collision, the probability of which is $N\delta R\, d\sigma_{n,e}$. The final range distribution cannot have changed, hence $p(E,R)_{initial} = p(E,R)_{after\,\delta R}$, i.e.

$$p(E,R) = N\delta R \int d\sigma_{n,e}\, p(R-\delta R, E-T_n-\Sigma_i T_{ei}) + (1 - N\delta R \int d\sigma_{n,e})\, p(R-\delta R, E) \quad .$$

The first term on the right hand side expresses the probability for a collision specified by elastic energy loss T_n and inelastic energy

loss $\sum_i T_{ei}$ to the target electrons, as well as the fact that the particles need to travel a length $R - \delta R$ to come to rest at R. The second term represents the complementary continuation probability for not making a collision. In the limit as $\delta R \to 0$, Eq. (3.16) is obtained. From Eq. (3.16) the moments of the range are obtained on multiplying by R^m and integrating by parts. The result is

$$m \langle R^{m-1}(E)\rangle = N \int d\sigma_{n,e} \left[\langle R^m(E)\rangle - \langle R^m(E - T)\rangle\right] \quad . \tag{3.17}$$

For m = 1,

$$1 = N \int d\sigma_{n,e} \left[R(E) - R(E - T)\right] \quad , \tag{3.18}$$

with $T = T_n + \sum_i T_{ei}$. When R(E - T) is expanded in powers of T then,

$$1 = N \int d\sigma_{n,e} \left[T\, dR/dE - 1/2\, T^2\, d^2R/dE^2 + \ldots\right] \quad . \tag{3.19}$$

If we keep only the first order terms, we get

$$1 = N(dR_1/dE) \int T\, d\sigma_{n,e} \quad , \tag{3.20}$$

and

$$dR_1/dE = 1/NS(E) \quad , \quad R_1 = \int (NS(E'))^{-1}\, dE' \tag{3.21}$$

where S = total stopping power = $S_e + S_n$, and R_n denotes the n^{th} approximation in R, i.e. n is the number of terms to be kept in Eq. (3.19).

Equation (3.21) is just the same as Eq. (3.6) derived without the aid of the distribution p(R,E). A higher order approximation for

$\langle R \rangle$ can be obtained by allowing more terms in the expansion of Eq. (3.19). For example, $\bar{R}_2$ is given by

$$\bar{R}_2(E) = \int dE'(NS(E'))^{-1}[1 + \frac{1}{2}\Omega^2(E')\, d(1/S(E'))/dE'] \quad . \quad (3.22)$$

The average square fluctuation in the range, i.e. $\overline{\Delta R^2} = \overline{R^2} - \bar{R}^2$, is obtained by multiplying Eq. (3.18) by $2\,\bar{R}(E)$ and subtracting the result from Eq. (3.17) with $m = 2$, i.e.

$$2\,\bar{R}(E) = N \int d\sigma_{n,e}\,[2\,\bar{R}^2(E) - 2\,\bar{R}(E)\,\bar{R}(E - T)] \quad (3.23a)$$

$$= N \int d\sigma_{n,e}\,[\bar{R}^2(E) - \bar{R}^2(E - T) + (\bar{R}(E) - \bar{R}(E - T))^2] \quad ,$$

and

$$2\,\bar{R}(E) = N \int d\sigma_{n,e}\,[\langle R^2(E)\rangle - \langle R^2(E - T)\rangle] \quad . \quad (3.23b)$$

This implies that

$$\int d\sigma_{n,e}\,(\overline{\Delta R^2}(E) - \overline{\Delta R^2}(E - T)) = \int d\sigma_{n,e}(R(E) - R(E - T))^2 \quad . \quad (3.23c)$$

Expanding the quantities of $(E - T)$ in powers of T, we get for the first approximation in $\overline{\Delta R^2}$

$$S(E)\,\frac{d(\overline{\Delta R^2})_1}{dE} = \Omega^2(E)\big(dR(E)/dE\big)^2 \quad , \quad (3.24)$$

with $\bar{R}(E) = \bar{R}_1(E)$. The second order approximation is obtained by the same procedure and is equal to

$$d(\overline{\Delta R^2})_2/dE = (\Omega^2(E)/S^3(E)N^2)\left(1 + \left(\frac{K}{\Omega^2 S} - \frac{5\Omega^2}{2S^2}\right)\frac{dS}{dE} + \frac{1}{2S}\frac{d\Omega^2}{dE}\right) \quad , \tag{3.25}$$

with $K = \int d\sigma\, T^3$.

It is important to notice that in all the expansions that have been made in powers of T, where T is the energy transfer to nucleus and electrons, it is assumed that T is small, a condition which is not justified when $M_1 = M_2$, since in this case T may take any value between E and 0. However, since the cross section is forward peaked, the average T is small which justifies the expansion.

Lindhard et al. [5] solved these equations for the power law scattering and did not take into consideration the electronic energy loss. Such an assumption allows for simple integrations. The projected range can be obtained by a similar procedure. The equation for the projected range similar to Eq. (3.18) is

$$1 = N \int d\sigma_{n,e}\, (\overline{R}_p(E) - \overline{R}_p(E - T)\cos\phi) \quad , \tag{3.26}$$

where ϕ is the deflection angle of the primary in the laboratory system. For small T, i.e. $M_1 \ll M_2$ or $M_2 \ll M_1$, Eq. (3.26) can be expanded in powers of T to give, for a first order approximation

$$1 = N(\overline{R}_{pl}(E) \int d\sigma_{n,e}\, (1 - \cos\phi) + d\overline{R}_{pl}(E)/dE \int T\, d\sigma_{n,e} \cos\phi) \quad . \tag{3.27}$$

Introducing the transport mean free path λ_{tr} and the transport stopping cross section S_{tr}, defined as

$$1/\lambda_{tr} = N \int d\sigma_{n,e} (1 - \cos \phi) \quad ,$$

and (3.28)

$$S_{tr} = \int d\sigma_{n,e} T \cos \phi \quad ,$$

Eq. (3.27) reduces to

$$1 = \bar{R}_{pl}(E)/\lambda_{tr}(E) + NS_{tr}(E) \, d\bar{R}_{pl}(E)/dE \quad , \tag{3.29}$$

which has the solution

$$\bar{R}_{pl}(E) = \int_0^E dE' \, (NS_{tr}(E))^{-1} \exp \left[\int_E^{E'} dE'' \, (\lambda_{tr}(E'') \, NS_{tr}(E''))^{-1} \right] . \tag{3.30}$$

Lindhard et al. [5] computed the first order correction from the average projected range to average range along the path, in the case when the mass ratio $\mu = M_2/M_1$ is small, i.e. for small angle of scattering, and with Thomas-Fermi potential, for various values of the electronic stopping constant k. Neglecting the electronic energy loss, and using power scattering law, $(1/r^s)$, the value $\bar{R}/\bar{R}_p$ is given by

$$\bar{R}/\bar{R}_p = 1 + \mu s^2/[4(2s - 1)] \quad . \tag{3.31}$$

Schiott [6,7] calculated this ratio, i.e. $\bar{R}/\bar{R}_p$, for $\mu \ll 1$ and $\mu \gg 1$, for different values of k. He calculated also the fluctuation in R_p. He showed that at low energies the range ratio $\bar{R}_p/\bar{R}$ and the relative straggling $\overline{\Delta R_p^2}/R_p^2$ are independent of the stopping substance when the reduced energy measure was used and are not strongly dependent on the atomic number of the projectile. He

found also that the distribution in the projected range was very broad.

The higher order moments for the projected range are difficult to be obtained in LSS theory. However, Sanders [8] generalized this method and used the inverse power-law potential to obtain more moments of the distribution. This will be reviewed under the WSS theory.

III-3-2. Integral Equations for the Damage

Lindhard et al. [9] developed an integral equation which governs the damage as represented by deposited energy, or number of vacancies, or any similar quantity associated with the irradiation process. Denoting such a quantity by ϕ, the final average of ϕ after irradiation with a particle of energy E, $\bar{\phi}(E)$, can be obtained, with all the assumptions of LSS theory, as follows. Suppose that a particle having the same mass and charge as the target atom, enters the target surface with energy E, and moves a distance dR. Then there is a probability $N\, dR\, d\sigma_{n,e}$ for collision after which the particle energy will be reduced to $E - T$, where $T = T_n + \sum_i T_{ei}$. The particle will have a $\bar{\phi}$-value of $\bar{\phi}(T_n - U)$, where U is the binding energy of the atom in the lattice. The electrons produced by collisions will have another contribution to $\bar{\phi}$, i.e. $\sum_i \bar{\phi}_e(T_{ei} - U_i)$, where U_i equals the ionization energy of the i^{th} ionized electron in the collision. There is also a probability $(1 - dR \int d\sigma_{n,e})$ that no collision happens in dR so that the particle leaves dR without change in its

energy E nor its $\bar{\phi}$. Summing all these quantities we get the following integral equation

$$\int d\sigma_{n,e} \left[\bar{\phi}(E - T) - \bar{\phi}(E) + \bar{\phi}(T_n - U) + \sum_i \bar{\phi}_e(T_{ei} - U_i)\right] = 0 \quad . \tag{3.32}$$

Usually the damage produced by the ionized electrons is small and can normally be neglected. In this case, the equation which describes the function $\bar{\phi}$ of the electrons, i.e. $\bar{\phi}_e$ is given by

$$\sum_i \int d\sigma_e' \left[\bar{\phi}_e(E - T_{ei}) - \bar{\phi}(E) + \bar{\phi}_e(T_{ei} - U_i)\right] = 0 \quad , \tag{3.33}$$

where $d\sigma_e'$ is the differential cross section of the collision of an electron with energy E with the target atom. This equation can be solved separately in $\bar{\phi}_e$, then the solution is used to solve Eq. (3.32) for $\bar{\phi}$.

If the ion is different from the target atom, i.e. $M_1 \neq M_2$ and $Z_1 \neq Z_2$, then the equation which describes its average $\bar{\phi}$ is given by

$$\int d\sigma_{1n,e} \left[\bar{\phi}_1(E - T) - \bar{\phi}_1(E) + \bar{\phi}(T_n - U) + \sum_i \bar{\phi}_e(T_{ei} - U_i)\right] = 0 \quad , \tag{3.34}$$

where $d\sigma_{1n,e}$ is the differential collision cross section of the incident ion with the target atom.

The following successive approximations are than made:

(a) the damage produced by electrons is neglected,

(b) the atomic binding energy U is neglected so that $\bar{\phi}(T_n - U)$ equals $\bar{\phi}(T_n)$,

(c) it is assumed that $\sum_i T_{ei}$ is small and after expanding $\bar{\phi}(E - T_n - \sum_i T_{ei})$ in powers of $\sum_i T_{ei}$, we keep only the first two terms. Then $\bar{\phi}(E - T_n - \sum_i T_{ei}) = \bar{\phi}(E - T_n) - \bar{\phi}'(E - T_n) \sum_i T_{ei}$, where $\bar{\phi}'$ denotes the differentiation with respect to E,

(d) the electronic and nuclear energy loss can be separated, i.e. $d\sigma_{n,e} = d\sigma_n + d\sigma_e$, and finally

(e) it is assumed that T_n is small compared to E, and often expanding $\bar{\phi}(E - T_n)$ in powers of T_n, only the first three terms are kept, i.e.

$$\bar{\phi}(E - T_n) = \bar{\phi}(E) - \bar{\phi}'(E)T_n + \frac{1}{2}\bar{\phi}''(E)T_n^2 \quad . \tag{3.35}$$

Applying these approximations, and using Eq. (3.5), we get

$$-\frac{1}{2}\bar{\phi}''(E)\,\Gamma_n(E) + \bar{\phi}'(E)\left(S_e(E) + S_n(E)\right) = \int d\sigma_n\,\bar{\phi}(T_n) + \int d\sigma_e \sum_i \bar{\phi}_e(T_{ei} - U_i) \quad , \tag{3.36a}$$

where $\Gamma_n(E) = \int d\sigma_n\, T_n^2$. For lower order approximations in Eq. (3.35), i.e. keeping only two terms in the series, Eq. (3.36a) reads

$$\bar{\phi}'(E)(S_e + S_n) = \int d\sigma_n\,\bar{\phi}(T_n) + \int d\sigma_e \sum_i \bar{\phi}_e(T_{ei} - U_i) \quad . \tag{3.36b}$$

$\bar{\phi}_e$ enters these equations as an inhomogeneous source term. Finding the solution for $\bar{\phi}_e$ from Eq. (3.33), and the solution of the homogeneous part of Eq. (3.35), the general solution for $\bar{\phi}$ can be obtained. $\bar{\phi}$ and $\bar{\phi}_e$ are then used to obtain the solution for $\bar{\phi}_l$ of the ion (Eq. 3.34).

Although Lindhard represented the probability distribution function from which higher order averages of ϕ (i.e. $\langle\phi^m\rangle$), can be obtained, he was concerned mainly with the second moment and the straggling in ϕ, i.e. $\langle\phi^2\rangle - \langle\phi\rangle^2$. To obtain this quantity, an equation similar to that of $\bar{\phi}$, Eq. (3.32), is deduced for $\langle\phi\rangle^2$ viz

$$\int d\sigma_{n,e} \left(-\langle\phi^2(E)\rangle + \langle\big(\phi(E - T) + \phi(T_n) + \sum_i \phi_e(T_{ei} - U_i)\big)^2\rangle\right) = 0 \quad . \tag{3.37}$$

Noting that $\langle\phi(E - T)\,\phi(T_n)\rangle = \langle\phi(E - T)\rangle\langle\phi(T_n)\rangle$, then

$$\int d\sigma_{n,e} \left[\Omega_\phi^2(E - T) - \Omega_\phi^2(E) + \Omega_\phi^2(T_n) + \sum_i \Omega_{\phi e}^2(T_{ei} - U_i)\right] = -\int d\sigma_{n,e} \left[\big(\bar{\phi}(E - T) + \bar{\phi}(T_n) + \sum_i \bar{\phi}_{ei}(T_{ei} - U_i)\big)^2 - \bar{\phi}^2(E)\right] \quad , \tag{3.38}$$

where $\Omega_\phi^2(E) = \langle\phi^2(E)\rangle - \bar{\phi}^2(E)$. Simple algebraic operations using Eqs. (3.32) and (3.37) produce

$$\int d\sigma_{n,e} \left[\Omega_\phi^2(E) - \Omega_\phi^2(T_n) - \Omega_\phi^2(E - T) - \sum_i \Omega_{\phi e}^2(T_{ei} - U_i)\right]$$

$$= \int d\sigma_{n,e} \left(\overline{\phi}(E - T) - \overline{\phi}(E) + \overline{\phi}(T_n) + \sum_i \overline{\phi}_e(T_{ei} - U_i)\right)^2 \quad . \tag{3.39}$$

An equation in $\Omega_{\phi e}^2$ can be obtained in the same way. Applying the five approximations mentioned above, we get

$$S_e(E) \frac{d\Omega_\phi^2(E)}{dE} = \int d\sigma_n \left(\Omega_\phi^2(E - T_n) - \Omega_\phi^2(E) + \Omega_\phi^2(T_n)\right)$$

$$+ \int d\sigma_n \left(\overline{\phi}(E - T_n) - \overline{\phi}(E) + \overline{\phi}(T_n)\right)^2 \quad . \tag{3.40}$$

For an ion which is different from the target, the average square straggling in ϕ_1, $\Omega_{\phi 1}^2$, is given by

$$S_{1e} \frac{d}{dE} \Omega_{\phi 1}^2(E) = \int d\sigma_{1n} \left(\Omega_{\phi 1}^2(E - T_n) - \Omega_{\phi 1}^2(E) + \Omega_\phi^2(T_n)\right)$$

$$+ \int d\sigma_{1n} \left(\overline{\phi}_1(E - T_n) - \overline{\phi}_1(E) + \overline{\phi}(T_n)\right)^2 \quad , \tag{3.41}$$

where $d\sigma_{1n}$ is the differential scattering cross section of the ion with the target atom.

Lindhard et al. [9] solved the above equations for the case of power-law potential and for $S_e \propto E^{1/2}$. This leads to a second order differential equation in $\overline{\phi}$, which has a solution in the form of a hypergeometric function. That solution was given for the case of $Z_1 = Z_2$ and $M_1 = M_2$. They also solved this case numerically for

Thomas-Fermi potential. They found that if $\overline{\phi}(E)$ equals the total deposited energy, where $\overline{\nu}(E)$ is the deposited energy in nuclear collision, and $\overline{\eta}(E)$ is the deposited energy into electronic collision, then $\overline{\phi}(E) = \overline{\nu}(E) + \overline{\eta}(E)$, and a simple formula can be used to fit the obtained solution. This formula in $\varepsilon - \rho$ units is

$$\overline{\nu}(\varepsilon) = \varepsilon(1 + k.g(\varepsilon))^{-1} \quad , \tag{3.42}$$

where $g \to 0$ as $\varepsilon \to 0$, and $g \to \varepsilon$ as $\varepsilon \to 10^3$. The value of $\varepsilon = 10^3$ corresponds roughly to the maximum of the electronic energy loss rate.

When $Z_1 \neq Z_2$, the energy is limited by the upper bound energy selected such that ε_1 or $\gamma\varepsilon_1$ equals 4.75, where ε_1 is the reduced energy of the ion and $\gamma = 4M_1M_2/(M_1 + M_2)^2$. This limit ensures that the electronic energy loss for both the ion and the recoil target atoms is proportional to $E^{1/2}$ and the nuclear stopping, for both, is $\propto E^{1-2/s}$ in case of the power law potential.

The LSS method is rather limited for obtaining higher moments. For example, the first and second moments for the range distribution enable one to construct a simple distribution function, e.g. a Gaussian. However, measured distributions show deviation from the simple Gaussian distribution.

III-4. WSS Method

The collective work of Winterbon, Sigmund, and Sanders, denoted here by WSS, represents a more accurate estimate for either ranges or damage distributions. The reason is that the WSS method enables one

to obtain more moments of the distributions, and in turn they can describe the distributions themselves more accurately. Also the formulation adopted in the method helps to predict the projected range distribution, which is the quantity that is measured experimentally rather than the path length.

II-4-1. Range Distribution

Sanders [8] generalized the LSS method, and he introduced the vector range probability distribution rather than the path length probability distribution defined in Eq. (2.16). In this treatment [8], he considered low energy projectiles, neglected the electronic energy loss, and used the inverse power potential. These assumptions, as usual, led to a closed form analytical solution.

Sigmund et al. [10] generalized this method even further to include electronic loss, assuming that it is continuous along the particle path. Sigmund et al. [10] then used numerical techniques to solve for only the first and the second moments. A very high numerical accuracy was required to obtain higher order moments. We will now concentrate on the Sanders [8] and Sigmund [10] treatment, which has been developed by Winterbon [12] to obtain up to the fifth moment, because it represents the basic idea of this method.

Consider for the first case, an incident ion of the same type as the target. Define a function $F(E,\bar{e},\bar{r})$ as the probability that an ion, with initial energy E, and velocity vector $\bar{v}$ is in direction of unit vector $\bar{e}$, i.e. $\bar{e} = \bar{v}/|\bar{v}|$, comes to rest at a vector distance $\bar{r}$ from its starting point $\bar{r} = 0$. Generalizing the argument that had

led to Eq. (3-16) we get an equation in F

$$- \bar{e}.\bar{v}\, F(E,e,r) = N \int d\sigma \,[F(E,\bar{e},\bar{r}) - F(E-T,\bar{e}',\bar{r})] + NS_e(E)\, \partial/\partial E \,(F(E,\bar{e},\bar{r})) \quad , \tag{3.43a}$$

with

$$\int d^3r\, F(E,\bar{e},\bar{r}) = 1 \quad , \tag{3.43b}$$

where $\bar{e}'$ is the velocity unit vector of the scattered ion, i.e.

$$\bar{e}.\bar{e}' = \cos \phi' \quad , \tag{3.44}$$

with ϕ' being the laboratory scattering angle.

Equation (3.43a) has been derived in a more rigorous way by Mazur and Sanders [13] on the basis of the hypothesis that the behavior of the penetrating ions can be considered as a Markoff process. The projected length R_p, the traverse distance R_l, the chord range R_c, and the penetration depth x are shown in Fig. 3-6 for a general incidence angle θ of the ion with the normal to the target surface.

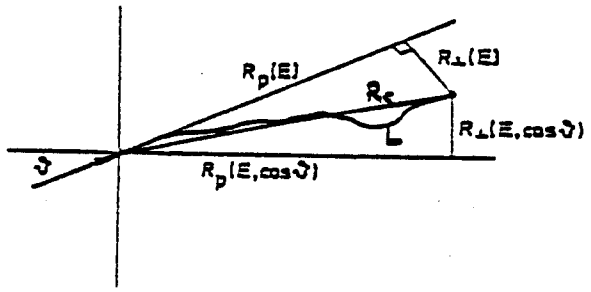

Fig. 3-6. Illustration of connection between different range concepts.

If we integrate Eq. (3-43a) over the z and y coordinates, the result will be

$$-\cos\theta\left[\frac{\partial}{\partial x}F(E,\bar{e},x)\right] = N\int d\sigma\left(F(E,\bar{e},x) - F(E-T,\bar{e}',x)\right) + NS_e(E)\left(\frac{\partial}{\partial E}F(E,\bar{e},x)\right) \quad , \tag{3.45}$$

where θ is the angle of incidence.

Due to the symmetry of the azimuthal angle, we have $F(E,\bar{e},x) = F(E,\cos\theta,x)$ or simply $F(E,\theta,x)$. To account for the back-scattering the normalization condition on $F(E,\theta,x)$ is

$$\int_{-\infty}^{+\infty} dx\, F(E,\theta,x) = 1 \quad . \tag{3.46}$$

Assuming that the penetrated material is isotropic, uniform, and infinite, the three variables E, θ, x, can be reduced to only one variable, that is E. This is done by expanding $F(E,\theta,x)$, first in Legendre polynomials, such that

$$F(E,\theta,x) = \sum_k (2k+1)\, P_k(\cos\theta)\, F_k(E,x) \quad . \tag{3.47}$$

Substituting Eq. (3.47) into Eq. (3.45) and noting that $\cos\theta = P_1(\cos\theta)$, we get

$$-k\frac{\partial}{\partial x}(F_{k-1}) - (k+1)\frac{\partial}{\partial x}(F_{k+1}) = (2k+1)\, S_e\frac{\partial}{\partial E}(F_k) + (2k+1)\, N\int d\sigma\,[F_k - P_k(\cos\theta)\, F_k(E-T)] \quad , \tag{3.48}$$

with $F_k = F_k(E,x)$. Taking the moments in x defined as

$$F_k^n(E) = \int dx\, x^n\, F_k(E,x) \quad , \tag{3.49}$$

one obtains

$$\delta F_k^n(E) = S_e \frac{\partial}{\partial E} \left(F_k^n(E)\right) + N \int d\sigma \left[F_k^n(E) - P_k(\cos\theta)\, F_k^n(E')\right] \quad , \tag{3.50}$$

where δF_k^n stands for

$$n\left(kF_{k-1}^{n-1}(E) + (k+1)\, F_{k+1}^{n-1}(E)\right)/(2k+1) \quad .$$

Due to mathematical constraints, F_k^n exists only for $n + k$ even, and $n > k$.

With the electronic loss included and with a realistic potential, e.g. Thomas-Fermi potential, very high numerical accuracy is required to go beyond the second moment, since small errors in the solutions of the lower moments accumulate in the higher ones.

Sigmund, Mathies, and Phillips [10] solved the above equation (Eq. 3-50) for the first and second moments only and for equal ion-target masses. Gibbons et al. [14] solved this equation for general ion-target combinations, and up to the third moment, but with a different numerical technique.

The last two groups of authors used a power series expansion in energy to solve for the moments. Winterbon [12,15] reduced the above equation of the moments to a set of algebraic equations and thus

attained more accuracy in the solution. Moreover, he obtained up to the fifth moment, with electronic energy loss included.

The basic idea in Winterbon's treatment [15] is to express Eq. (3.48) as a function of E and t = T/E. He then expands F_k^n as a double power series, one variable being the incident energy E, and the other being, essentially, the ratio of the strengths of the inelastic interaction, and the elastic interaction. The differential cross section $d\sigma$ is also expanded, for the inverse power cross section, as a power series in (Et) after factoring out a function of t. Substituting these expansions in Eq. (3.48), one gets a set of recursion relations for the unknown coefficients, $\alpha_{ij}(k,n)$ in the expansion of F_k^n. The resulting integrals over the variable t may then be evaluated by known methods [16]. Hence the coefficients of F_k^n, which are double power series in E and t, can be obtained to any desired degree of accuracy. Convergence of the series is expected to be good within a limited range of energies ε = 10-100.

It should be mentioned that there is not much difference between the case of equal ion and target masses and the case of different masses. In the former, the integration over the energy transfer T extends from 0 to E, the energy of the incident ion. In the latter, the integration extends from 0 to the maximum energy transfer $T_m = \gamma E$. Once the moments are obtained the density distribution can be constructed. This will be discussed later.

II-4-2. Damage Distribution [21,18,25]

The equations which govern the deposited energy can be obtained with the same arguments used previously in the LSS method review. Consider the function $F(\bar{r},\bar{v})$, which is defined so that $F(\bar{r},\bar{v})dr^3$ is the average amount of energy deposited in the volume element dr^3 around r, due to and after an ion had started its motion at time $t = 0$, at the point $r = 0$, with energy $= 1/2\ M_1|\bar{v}|^2$ in the direction $\bar{v}/|\bar{v}|$, where $\bar{v}$ is the initial velocity, and comes to rest at $t = \infty$. Then $F(\bar{r},\bar{v})$ must obey the condition

$$\int d^3r\ F(\bar{r},\bar{v}) = E \quad .$$

During time δt from the beginning the ion may undergo a collision with a probability $|\bar{v}\delta t|\ N \int d\sigma_1$, where N is the atomic density of the target, and $d\sigma_1$ is the differential collision cross section. Now there will be two particles in motion, the scattered particle and the struck atom, each of which has its own function F, i.e. $F(\bar{r},\bar{v}')$ of the scattered particle and $F_t(\bar{r},\bar{v}'')$ of the struck atom, where $\bar{v}'$ and $\bar{v}''$ are the velocities of each particle, respectively. There is also a probability that the incident particle will not suffer a collision; this probability equals $(1 - |\bar{v}|\ \delta t \int d\sigma_1)$. In this case, the particle's F function will be $F(\bar{r}-\bar{v}\delta t,v)$. Summing these probabilities we have on the average

$$F(\bar{r},\bar{v}) = |\bar{v}\delta t|\, N \int d\sigma_1\, [F(\bar{r},\bar{v}') + F_t(\bar{r},\bar{v}'')] + \left(1 - N|\bar{v}\delta t| \int d\sigma_1\right) F(\bar{r}-\bar{v}dt,\bar{v}) \quad . \tag{3.52}$$

Separating the electronic stopping from the cross section $d\sigma_1$, assuming it is continuous along the path with a well defined rate, i.e.

$$dE/dR = - S_e(E) \quad ,$$

or

$$M_1 |\bar{v}|\ \delta|\bar{v}|/\delta R = M_1\ dv/dt = - S_e(E) \quad , \tag{3.53}$$

then, according to this assumption, $\bar{v}$ in the last term of Eq. (3.52) is replaced by $v - \delta v = v - S_e\delta t/M_1$. Expanding the first term in (δt) and keeping only two terms, Eq. (3.52) becomes

$$\frac{-\bar{v}}{|\bar{v}|}\left(\frac{\partial F(\bar{r},\bar{v})}{\partial \bar{r}}\right) = N \int d\sigma_1\, [F(\bar{r},\bar{v}) - F(\bar{r},\bar{v}') - F_t(\bar{r},\bar{v}'')] + \frac{S_e}{|\bar{v}|}\left(\frac{\partial F(\bar{r},\bar{v})}{\partial |\bar{v}|}\right) \quad . \tag{3.54}$$

A similar equation that describes the recoil term F_t, which enters the above equation as a source term, is presented by

$$\frac{-\bar{v}}{|\bar{v}|}\left(\frac{\partial F_t(\bar{r},\bar{v})}{\partial r}\right) = N\int d\sigma_t\,[F_t(\bar{r},\bar{v}) - F_t(\bar{r},\bar{v}) - F_t(\bar{r},\bar{v}")] + \frac{S_{et}}{|\bar{v}|}\left(\frac{\partial F_t(\bar{r},\bar{v})}{\partial|\bar{v}|}\right) \quad , \tag{3.55}$$

where the suffix t denotes the associated quantities for the target. Clearly, if the incident ion is the same as the target atom, Eq. (3.55) is used alone.

Equation (3.54) is used as well for obtaining the range distribution. This is achieved by accompanying the recoil term F_t by a factor ζ, which is zero in case of range distribution, and unity for damage distribution. Making the same steps described after Eq. (3.43a) we obtain

$$\delta F_k^n(E) = S_e\left(\frac{\partial F_k^n}{\partial E}\right) + N\int d\sigma_1\,[F_k^n(E) - P_k(\cos\phi')\,F_k^n(E') - \zeta P_k(\cos\phi")\,F_{kt}^n(E")] \quad , \tag{3.56}$$

where ϕ', E', $\phi"$, and $E"$ are the laboratory scattering angle and the energy of the scattered and recoil atoms, respectively.

The solution of this equation follows the same procedure described above for the range distribution, except for the unequal target-projectile combination, where the solution of Eq. (3-55), for the target-on-target, is required first before solving for the ion. The fact that the deposited energy distributions are much less symmetric than the range distribution, and consequently require

moments much higher than that of the range, indicates the importance of the Winterbon method.

III-4-3. Construction of Distributions

Several methods can be used to obtain the distribution function, depending on the number of moments available. Due to the limitations on obtaining more than the second moment in the early studies, the only approximation that had been used for the distribution function was the Gaussian approximation [10], given by

$$F(x) \simeq \left(\frac{1}{2\pi\langle\Delta x^2\rangle}\right)^{1/2} \exp\left[\frac{-(x - \langle x\rangle)^2}{2\langle\Delta x^2\rangle}\right] \quad . \tag{3.57}$$

If the first n moments are known, one can improve Eq. (3.57) by

$$F(x) \simeq F_n(x) = \Psi(x) \sum_{m=0}^{n} C_m p_m(x) \quad , \tag{3.58}$$

where $p_m(x)$ form a set of orthogonal polynomials, and Ψ is given by Eq. (3.57). If the assumption that Ψ is Gaussian is correct, the proper polynomials p_m are the Hermite polynomials of the same argument as that of the exponential in $\Psi(x)$. Due to the slow convergence of the series in Eq. (3.58), Winterbon proposed also another method to obtain the distribution with a more rapid convergence [12].

III-5. Brice Method [17-22]

Brice first formulated the transport equations governing the ion distribution during the slowing down process and solved them for the first and second moments to obtain the spatial distribution of the ions as a function of their instantaneous energy. These distributions, which are all assumed to be Gaussian, are then used to calculate the depth distribution of the energy deposited into atomic processes (damage energy) or electronic processes. In the early work of Brice [17-19], the energy transported by the recoils was neglected, but he considered this effect in a more recent work [20-22].

III-5-1. First Step: Spatial Distribution as a Function of the Instantaneous Energy

In this method we need to define the following quantities:

(a) $P_3(E,E',\bar{r})\, d\bar{r}$ is the probability that an ion will be located in the volume element $d\bar{r}$, centered at $\bar{r}$, when its instantaneous energy is E'. The initial energy is E, and the initial velocity direction is parallel to the x-axis of the coordinate system. The initial condition on P_3 is $P_3(E,E,\bar{r}) = \delta(\bar{r})$ where δ is the three-dimensional Dirac delta function.

(b) $P_1(E,E',x)\, dx$ is the probability that an ion, with the same initial conditions described in (a) above, will be located in the interval x to x + dx when its energy is E'. P_1 is related to P_3 through the relation

$$P_1(E,E',x) = \int_{-\infty}^{+\infty}\int_{-\infty}^{+\infty} P_3(E,E',\bar{r})\, dydz \quad . \tag{3.59}$$

The initial condition for P_1 is: $P_1(E,E,x) = \delta(x)$.

(c) $P(E,E',R)\,dR$, the path length distribution function, is the probability that the ion will have traveled a path length lying in the interval R to R + dR, when its energy is E'.

(d) $p(E,E',x,\cos\theta)\,dx$ is the probability that an ion, with initial energy E and initial direction $\cos\theta$ with respect to the x-axis, will lie in the interval x to x + dx, when its energy is E'.

(e) $q(E,E',s,\cos\theta)\,2\pi s\,ds$ is the probability that the ion, with the initial conditions described in (d), will lie in the interval s, s + ds away from the x-axis when its energy is E' where $s = (y^2 + z^2)^{1/2}$. The probability P_1 is related to p by

$$P_1(E,E',x) = p(E,E',x,1) \quad . \tag{3.60}$$

The moments of the projected range distribution $\langle R_p^m \rangle$, can be obtained from

$$\begin{aligned} \langle R_p^m(E,E') \rangle &= \int_{-\infty}^{+\infty}\int_{-\infty}^{+\infty}\int_{-\infty}^{+\infty} x^m\, P_3(E,E',\bar{r})\; dxdydz \\ &= \int_{-\infty}^{+\infty} x^m\, P_1(E,E',x)\; dx \\ &= \int_{-\infty}^{+\infty} x^m\, p(E,E',x,1)\; dx \quad . \end{aligned} \tag{3.61}$$

Also the moment of the perpendicular range, $\langle R_\perp^m(E,E') \rangle$, can be obtained from

$$\langle R_{\perp}^{m}(E,E')\rangle = \int_{-\infty}^{+\infty}\int_{-\infty}^{+\infty}\int_{-\infty}^{+\infty} (y^2 + z^2)^{m/2}\, P_3(E,E',\bar{r})\, dxdydz$$

$$= 2\pi \int s^{m+1}\, q(E,E',s,1)\, ds \quad . \tag{3.62}$$

The moment of the path length distribution is

$$\langle R^{m}(E,E')\rangle = \int R^{m}\, P(E,E',R)\, dR \quad . \tag{3.63}$$

The equations which govern the distribution functions $P(E,E',R)$, $P_3(E,E',r)$, and $P_1(E,E',x)$ can be derived similarly as in the LSS and WSS methods. In these methods we were dealing with the same functions with $E' = 0$. Due to the condition imposed by the presence of E', the integration over $d\sigma_{n,e}$ should be taken only over the values of energy transfer T, $(T = T_n + T_e)$, such that the scattered particle energy $(E - T)$ should be greater than E'. Also another effect arises at the origin when it happens that the particle may attain the energy E' in a collision.

If we account for both of these effects the equation which governs the path length distribution $P(E,E',R)$ reads

$$-\frac{\partial P(E,E',R)}{\partial R} = N\Big(P(E,E',R)\int d\sigma_{n,e} - \int' d\sigma_{n,e}\, P(E-T,E',R)$$

$$- \delta^{+}(R)\int'' d\sigma_{n,e}\Big) \quad , \tag{3.64}$$

where the prime over the integral sign denotes the integration over only the energy transfer T such that $E - T > E'$, and the double

primed integral indicates the integration over T such that $(E - T) < E'$, and δ^+ is the Dirac delta function. The moments equation is

$$m \langle R^{m-1}(E,E')\rangle = N \langle R^m(E,E')\rangle \int d\sigma_{n,e} - N \int' d\sigma_{n,e} \langle R^m(E-T,E')\rangle \quad . \tag{3.65}$$

The integral equations governing the moments of $P_1(E,E',x)$ and $P_3(E,E',\bar{r})$ are obtained by deriving the equations which govern $p(E,E',x,\cos\theta)$ and $q(E,E',s,\cos\theta)$, both having been derived by Schiott [6], and then using Eqs. (3.61) and (3.62) with $\cos\theta = 1$. These steps lead to the first and second moments given by

$$1 = N[\langle R_p(E,E')\rangle \int d\sigma_{n,e} - \int' d\sigma_{n,e} \cos\phi \langle R_p(E-T,E')\rangle] \quad , \tag{3.66a}$$

$$2\langle R_p(E,E')\rangle = N\big(\langle R_r^2(E,E')\rangle \int d\sigma_{n,e} - \int' d\sigma_{n,e} \left(1 - \frac{3}{2}\sin^2\phi\right) R_r^2(E-T,E')\big) \quad , \tag{3.66b}$$

and

$$2\langle R_p(E,E')\rangle = N\Big(\langle R_c^2(E,E')\rangle \int' d\sigma_{n,e} - \int d\sigma_{n,e}\, \langle R_c^2(E-T,E')\rangle\Big) \quad , \tag{3.66c}$$

where

$$\langle R_c^2(E,E')\rangle = \langle R_p^2(E,E')\rangle + \langle R_\perp^2(E,E')\rangle \quad , \tag{3.67}$$

and

$$\langle R_r^2(E,E')\rangle = \langle R_p^2(E,E')\rangle - \tfrac{1}{2}\langle R_\perp^2(E,E')\rangle \quad , \tag{3.68}$$

with ϕ being the scattering angle in the laboratory system. For the path length moments, from Eq. (3.65) with m = 1, we get

$$1 = N\Big(\langle R(E,E')\rangle \int d\sigma_{n,e} - \int' d\sigma_{n,e}\, \langle R(E-T,E')\rangle\Big) \quad . \tag{3.69}$$

Equations (3.66) and (3.69) have the same form, and can be written in the general form

$$g(E,E') = N\Big[\int d\sigma_{n,e}\, X(E,E') - \int' d\sigma_{n,e}\, f(\phi)\, X(E-T,E')\Big] \quad , \tag{3.70}$$

where $f(\phi)$ is a function of the scattering angle ϕ in the laboratory system. It equals "cos ϕ" in Eq. (3.66a), "$(1 - 3/2 \sin^2\phi)$" in Eq. (3.66b), and "1" in Eqs. (3.66c) and (3.69).

The general form of the integral equation, Eq. (3.70), can be converted into a differential equation by expanding X(E-T,E') in

powers of T. This is justified by the fact that $d\sigma_{n,e}$ is forward peaked. The obtained equation is

$$g(E,E') = \sum_{m=0}^{\infty} B_m(E,E') \frac{d^m X(E,E')}{dE^m} \quad , \tag{3.71}$$

with

$$B_o(E,E') = N\left(\int d\sigma_{n,e} - \int' f(\phi)\, d\sigma_{n,e}\right) \quad , \tag{3.72}$$

and

$$B_1(E,E') = (-1)^{m+1} \left(\frac{N}{m!}\right) \int' T^m f(\phi)\, d\sigma_{n,e} \quad . \tag{3.73}$$

The solution of Eq. (3.71) can be obtained to any order in the series through an iterative process. Brice solved this equation only to the second order, and gave estimations for the third order correction to $\langle R_p(E,E')\rangle$ and $\langle R(E,E')\rangle$ to be ~ 1% of $\langle R_p(E,0)\rangle$ and $\langle R(E,0)\rangle$.

Brice assumed the separability of the electronic and nuclear contributions to the collision cross section $d\sigma_{n,e}$, i.e.

$$\int (\ )\, d\sigma_{n,e} = \int (\ )\, d\sigma_n + \int (\ )\, d\sigma_e \tag{3.74}$$

where $d\sigma_n$ and $d\sigma_e$ are the separate nuclear and electronic scattering cross sections, respectively. Moreover, due to the fact that the energy transfer to the individual electrons, T_e, is small and the scattering angle in this event is negligible ($\simeq 2m_e/M_1$), Brice considered the contribution of electrons only to the first order, i.e.

$$B_1(E,E') = N\left[\int' d\sigma_n \, Tf(\phi) + \int' d\sigma_e \, TF(\phi)\right]$$

$$\approx N \int' d\sigma_n \, Tf(\phi) + NS_e f(\phi) \qquad (3.75)$$

$$= N \int' d\sigma_n \, Tf(\phi) + NS_e \quad ,$$

where

$$S_e = \int T \, d\sigma_e \quad , \qquad (3.76)$$

assuming that $E - E'$ is greater than the maximum energy transfer to an electron.

At this stage the distributions P_1 and P_3 can be obtained, with the assumption that they are Gaussian. From the solutions of the above equations we can define

$$\Delta R_p = (\overline{R_p^2} - \overline{R}_p^2)^{1/2} \quad ,$$

and (3.77)

$$\Delta R_\perp = (\overline{R_\perp^2})^{1/2} \quad .$$

P_1 and P_3 are then readily obtained from

$$P_1(E,E',x) = (2\pi\Delta R_p^2)^{-1/2} \exp\left[\frac{-(x - R_p)^2}{2\Delta R_p^2}\right] \quad , \qquad (3.78)$$

and

$$P_3(E,E',\bar{r}) = P_1(E,E',x)(\pi\Delta R_\perp^2)^{-1} \exp\left[\frac{-(y^2 + z^2)}{\Delta R_\perp^2}\right] \quad . \qquad (3.79)$$

III-5-2. Second Step: Damage Distribution

Once the distribution functions P_1, P_3, and P are obtained, the damage distribution can be evaluated as follows. If the incident ions and the target atoms interact with some energy dependent cross section $d\sigma$ to produce some quantity of interest Q, the average amount of Q produced in a volume element $d\bar{r}$ around $\bar{r}$ is given by

$$d^3\bar{Q} = \int_E^0 \left(P_3(E,E',\bar{r})\ d\bar{r}\ N\left(\frac{d\bar{R}}{dE'}\right) \int q(T)\ d\sigma\ (E',T)\right) dE' \quad , \quad (3.80)$$

where the q(T) is the average amount of Q produced in the element dT of the differential cross section $d\sigma$ (E',T), and dR is the average distance moved by the ion with energy E' in losing an amount of energy dE'. Since dF is not a function of E', Eq. (3.80) can be written as

$$\frac{d^3\bar{Q}}{dr} = Q(E,r) = N \int_E^0 \left(P_3(E,E',r)\left(\frac{d\bar{R}}{dE'}\right) q(T)\ d\sigma\ (E',T)\right) dE' \quad , \quad (3.81)$$

which describes the spatial distribution of Q, Q(E,r). The depth distribution of Q can be obtained similarly as

$$Q(E,x) = N \int_E^0 \left(P_1(E,E',x)\left(\frac{dR}{dE'}\right) q(T)\ d\sigma\ (E',T)\right) dE' \quad . \quad (3.82)$$

The derivative $d\bar{R}/dE'$ is obtained from Eq. (3.63), i.e.

$$\frac{d\bar{R}}{dE'} = \frac{d\langle R(E,E')\rangle}{dE'} = d\left(\int_E^0 RP(E,E',R)\ dR\right) / dE' \quad . \quad (3.83)$$

For fixed E, we have

$$\left(\frac{dR}{dE'}\right) dE' = \left(\frac{dR}{dR_p}\right).\left(\frac{dR_p}{dE'}\right).dE' = \left(\frac{dR}{dR_p}\right) dR_p \quad . \tag{3.84}$$

Q(E,r) and Q(E,x) can then be written as

$$Q(E,r) = \int_0^{R_p(E,0)} P_3(E,E',\bar{r})\left(\frac{dR}{dR_p}\right) \Sigma\,(E')\, dR_p \quad , \tag{3.85}$$

and

$$Q(E,x) = \int^{R_p(E,0)} P_1(E,E',x)\left(\frac{dR}{dR_p}\right) \Sigma\,(E')\, dR_p \quad , \tag{3.86}$$

with

$$\Sigma\,(E') = N \int q(T)\, d\sigma\,(E',T) \quad . \tag{3.87}$$

Equations (3.84) and (3.85) do not consider the effect of recoils, i.e. the quantity dQ was assumed to be deposited at the point of interaction [17,18]. To account for the recoil effect, Brice considered only the depth distribution, i.e. Q(E,x), and assumed that all ions travel parallel to the x-axis. Then the initial deposition of the quantity dQ in the interval x to x + dx will be distributed in the depth, x', with a normalized distribution D(E',x'-x). The relative depth distribution of dQ, for all ions which have instantaneous energy E', is given by S(E,E',x') where

$$S(E,E',x') = \int_{-\infty}^{+\infty} P_1(E,E',x)\, D(E',x'-x)\, dx \quad . \tag{3.88}$$

The final depth distribution is then obtained by substituting S(E,E',x) in Eq. (3.82) in place of $P_1(E,E',x)$, i.e.

$$Q(E,x) = \int_0^E S(E,E',x)\, \Sigma\,(E')\, \left(\frac{dR}{dE'}\right) dE' \quad . \tag{3.89}$$

To solve the above equation, $S(E,E',x)$ should be known. The first few moments of S were used to construct an approximate representation of S, which is then used to solve Eq. (3.89). Using the following definitions for the spatial moments of the distributions P_1, D, S, and Q:

$$M_{np}(E,E') = \langle R_p^n(E,E') \rangle$$

$$= \int x^n P_1(E,E',x)\, dx \quad , \tag{3.90}$$

$$M_{nD}(E') = \int x^n D(E',x)\, dx \quad , \tag{3.91}$$

$$M_{nS}(E,E') = \int x^n S(E,E',x)\, dx \quad , \tag{3.92}$$

and $$M_{nQ}(E) = \int x^n Q(E,x)\, dx \quad , \tag{3.93}$$

and combining Eqs. (3.91) and (3.88), we get

$$M_{nS}(E,E') = \sum_k^n C_{nk}\, M_{kp}(E,E')\, M_{(n-k)D} \quad , \tag{3.94}$$

where C_{nk} are binomial coefficients. Hence, the moments $M_{ns}(E,E')$ depend on $\langle R_p^n(E,E') \rangle$ of the ion, which is already known from the first step calculations, and the moments of the recoil atom $M_{nD}(E')$. These moments are evaluated by a weighted average over the interaction cross section $d\sigma\,(E',T)$ via

$$M_{nD}(E') = \frac{\int M'_{nQ}(T,\eta)\, q(T)\, d\sigma\,(E',T)}{\left(\int q(T)\, d\sigma\,(E',T)\right)} \quad , \tag{3.95}$$

where η is the direction cosine with respect to the x-axis of the initial velocity vector of a target atom recoiled with energy T, and

$M'_{nQ}(T,\eta)$ is the n^{th} moment of the depth distribution of the deposited quantity of interest by the recoil atom.

In the calculation of the damage distributions, $q(T)$ and $Q(E,x)$ are, respectively, the damage energy of a recoil atom with initial energy T (the portion of T which will ultimately be deposited into atomic process), and the depth distribution of energy deposited into atomic process. Brice used two moments to calculate the moments of the depth distribution of the damage energy of the recoil atom, M'_{nQ}. In the first method [29], he assumed that the recoil atoms deposit their damage energy, as well as the ionization energy, uniformly along a straight line from the position of the initial interaction and the position at which the atoms come to rest. If $R_p(T)$ is the average projected range of a recoil initially with kinetic energy T, and $\Delta R_p(T)$ along with $\Delta R_t(T)$ are the standard deviations in the parallel and the transverse directions with respect to the initial direction of the recoil, then the first and second moments are

$$M'_{1Q}(T,\eta) = \frac{1}{2}\,\eta R_p(T) \quad ,$$

and

$$M'_2(T,\eta) = \frac{1}{3}\left[(\eta R_p(T))^2 + (\eta \Delta R_p(T))^{1/2} + (1-\eta^2)(\Delta R_t(T))^2\right] \quad , \tag{3.96}$$

respectively.

In the second method, Brice made use of the results obtained by Sigmund et al. [10] and which were exact for the case of $M_1 = M_2$, which is certainly the case of the recoil atom in the target. In this calculation [10], the ratio of the average projected $\langle x_R \rangle$ to the average damage depth $\langle x_D \rangle$ ranged from 1.2 to 1.27 for ε in the range of 0.01 to 1.0. This range of the reduced energy includes most of the primary recoils. Consequently, Brice [20] used for the average and the standard deviation of the damage distribution (of the recoils) the estimates

$$M'_{1Q}(T) = 0.8\, R_p(T) \quad ,$$

$$\text{and} \quad M'_{2Q}(T) - (M'_{1Q}(T))^2 = 0.8 \left(\langle R_p^2 \rangle - (\langle R_p(T) \rangle)^2 \right) \quad . \tag{3.97}$$

However, in his recent treatment [20] he averaged first over the projected range of the recoils and then used an expression similar to Eq. (3.97). This can be described as follows.

Let $R_p(T,0)$, $\Delta R_p(T,0)$ and $\Delta R_\perp(T,0)$ be the range and the straggling parameters of the recoiling target atom of energy T, and let η be the cosine of the recoil angle in the laboratory coordinates, relative to the direction of the ion before the collision which created the recoil atom. Then define

$$r_p(T) = \eta R_p(T,0) \quad , \tag{3.98}$$

and

$$r_{p2}(T) = [\eta R_p(T,0)]^2 + [\eta \Delta R_p(T,0)]^2 + (1 - \eta^2)\, \Delta R_\perp^2(T,0)/2] \quad . \tag{3.99}$$

Then

$$G_1(E) = \int_0^{T_m} r_p(T)\, q(T)\, \sigma(E,T)\, dT \;/\; \int_0^{T_m} q(T)\, \sigma(E,T)\, dT \quad , \tag{3.100}$$

and

$$G_2(E) = \int_0^{T_m} r_{p2}(T)\, q(T)\, \sigma(E,T)\, dT \;/\; \int_0^{T_m} q(T)\, \sigma(E,T)\, dT \quad , \tag{3.101}$$

represent the weighted averages of the recoil range and its square projected on the direction of motion of the incident ions, which are related to $M'_{1Q}(T)$ and $M'_{2Q}(T)$ by the approximations

$$M'_{1Q}(T) = 0.8\, G_1 \quad , \tag{3.102}$$

and

$$M'_{2Q}(T) - (M'_{1Q}(T))^2 = 0.64\, [G_2 - G_1^2] \quad . \tag{3.103}$$

These values are then used in Eq. (3.93) to obtain $M_{nD}(E')$ which are used in turn in Eq. (3.92) along with $R_p(E,E')$ and $\langle R_p^2(E,E'')\rangle$ of the incident ion to obtain $M_{nS}(E,E'')$. This latter term is used to construct the required distribution $S(E,E',x)$. The same procedure is used to evaluate the distribution of the energy deposited into ionization and excitation.

III-6. Other Analytical Methods

Thus far we have considered methods which have reasonable assumptions and approximations, which make them the most popular in the field. However, there are many other methods which can be used to attack the problem. Most of these methods used the assumption of the hard sphere potential and neglected entirely the electronic energy loss, and sometimes were restricted to special cases such as the case of equal ion and target masses.

These methods were developed initially when the nature of radiation damage had not been well explored and understood. Among these methods is that of Baroody [23-25], whose calculations were based directly on the moments form of the Boltzmann transport equation to obtain a range distribution. Leibfried [26] also developed the so-called operator method to get the averages of the range distributions. A review of such methods was made by Carter et al. [27].

Finally, very recently Williams [28-30] attacked the problem using a completely different method. He derived a set of linear, coupled Boltzmann transport equations which describe the projectile and recoil atoms distribution in space, time, and energy. He showed that Lindhard transport equation which has been derived based on the simple argument led to Eq. (3.16), is just a partially adjoint equation in energy and direction to the usual or the forward form of the Boltzmann equation. He showed the merits of using the forward form, which is familiar and well understood in the neutron transport field. One of the advantages of using the forward form is the applicability

of the method to multi-layers problems [29,31]. Williams reviewed his ideas in an intensive and extensive review article [30]. The reader may refer to it for further information.

References for Chapter III

1. M. T. Robinson and I. M. Torrens, Phys. Rev. B, 9, 12, 5008 (1974).

2. J. Lindhard and M. Scharff, Phys. Rev. 124, 128 (1961).

3. O. B. Firsov, Zh. Eksp. Teor. Fiz. 36, 1517 (1959) [Sov. Phys. - JETP 36, 1076 (1959)].

4. M. T. Robinson, Proceeding of Int. Conf. on "Radiation-Induced Voids in Metals," ed. J. W. Corbett and L. C. Ianniells, Albany, NY, June 1971. CONF-710601, 397 (1972).

5. J. Lindhard, M. Scharff and H. E. Schiott, Mat. Fys. Medd. Dan. Vid. Selsk. 33, 14 (1963).

6. H. E. Schiott, Mat. Fys. Medd. Dan. Vid. Selsk. 35, 9 (1966).

7. H. E. Schiott, Can. J. Phys. 46, 449 (1968).

8. J. B. Sanders, Can. J. Phys. 46, 455 (1968).

9. J. Lindhard, V. Nielsen, M. Scharff, and P. V. Thomson, Mat. Fys. Medd. Dan. Vid. Selsk. 33, 10 (1963).

10. P. Sigmund, M. T. Mathies, and D. L. Philips, Rad. Eff. 11, 39 (1979).

11. P. Sigmund, Rev. Roum. Phys. 17, 823, 969, and 1079 (1972).

12. K. B. Winterbon, Ion Implantation Range and Energy Deposition Distributions, Vol. 2, IFI/Plenum, NY, 1975.

13. P. Mazur and J. B. Sanders, Physica 44, 444 (1969).

14. J. F. Gibbons, W. S. Johnson, and S. W. Mylrorie, Projected Range Statistics, Powden, Hutc. & Ross, Inc. (1975).

15. K. B. Winterbon, Rad. Eff. 13, 215 (1972).

16. K. B. Winterbon, P. Sigmund, and J. B. Sanders, Mat. Fys. Medd. Dan. Vid. Selsk. 37, 14 (1970).

17. D. K. Brice, Appl. Phys. Letters 16, 1034 (1970).

18. D. K. Brice, Rad. Eff. 6, 77 (1970).

19. D. K. Brice, Rad. Eff. 11, 227 (1971).

20. D. K. Brice, J. Appl. Phys. 46, 3385 (1975).

21. D. K. Brice, SAND75-0622; Sandia Laboratories, Albuquerque, New Mexico, (1977).

22. D. K. Brice, Ion Implantation Range and Energy Depostion Distributions, Vol. 1, IFI/Plenum, NY, (1975).

23. E. M. Baroody, J. Appl. Phys. 35, 2074 (1963).

24. E. M. Baroody, J. Appl. Phys. 36, 3565 (1965).

25. E. M. Baroody, J. Appl. Phys. 40, 2555 (1969).

26. G. Leibfried, Z. Physik 171, 1 (1963).

27. G. Carter and J. S. Colligon, Ion Bombardment of Solids, American Elsevier, NY, (1968).

28. M. M. Williams, J. Phys. A, 9, 771 (1976).

29. M. M. Williams, Rad. Eff. 37, 131 (1978).

30. M. M. R. Williams, Prog. Nucl. Energy 3, 1 (1979).

31. K. B. Winterbon, Rad. Eff. 39, 31 (1978).

CHAPTER IV

COMPUTER SIMULATION

IV-1. Introduction

Computer simulation has played a significant role in the present understanding of radiation damage and the directional effects in crystals. The difficulties of analytical methods increase very rapidly if one tries to remove any of its basic simplifying approximations (Section III-2). This fact makes computer simulation techniques the only alternative for a wider and deeper understanding of radiation damage in materials.

Computer simulation techniques can be categorized into two basic types, depending on how they handle the collision of atoms in materials. The first type, and the older one, is usually known as the dynamic or the many-body integration (MBI) method, and was developed by Vineyard and his co-workers [1-3]. The second type was introduced by Yoshida [4], Robinson and Oen [5,11,12] and Beeler [6,7], and is usually known as the binary collision approximation (BCA) method.

IV-2. Many-Body Integration Method [1-3]

This method deals only with crystalline solids. A crystal contains a few hundred to a few thousand atoms, each atom interacting with other atoms through a two-body central interatomic potential. The material surrounding the crystal is simulated by special forces on the atoms comprising the boundaries of the crystal. These forces simulate the reaction forces of atoms beyond the boundaries caused by any displacement of atoms in the crystal. Practically, these forces

are represented by a spring force proportional to the displacement of the surface atom, a viscous force, proportional to the velocity of the surface atom, and constant forces which are chosen so that the set of atoms can be in a static equilibrium.

The Newtonian equations of motion are written for each atom yielding 3 x N equations, where N is the number of atoms in the crystal. An event may be initiated by starting one atom in motion with a specified velocity vector, simulating a "primary knock on event." A simple central difference procedure is then used to integrate these equations of motion until an equilibrium position is reached, or until the collision process of interest has reached the crystal boundary. Vineyard's computer program, which was the first to embody this method, is called GRAPE.

The calculations are considered fully dynamic since all degrees of freedom are allowed to vary at once in accordance with the requirements of the interaction forces and the Newtonian laws of dynamics. This many-body integration approach has proven to be very useful in demonstrating directional effects such as focusing and channeling in low index directions of the crystal. The limitations of this method come from the allowable speed and memory capacities of computers, and as a result, only a few hundred eV primary knock ons can be simulated.

IV-3. Binary Collision Approximation Method

Beeler [6] introduced the assumption that the atomic collision cascade can be described as a branching sequence of binary collision

events. Only moving atoms with kinetic energies above a certain threshold energy are considered in the cascade, and those which have kinetic energies below another threshold energy are considered as interstitials. Recombination between interstitials and vacancies produced in the cascade is assumed to occur when the distance of separation between a vacancy and an interstitial lies within a recombination spacing determined from a separate fully dynamic calculations.

Beeler's calculations [6] start with a single knock-on endowed with a momentum in an arbitrary direction. The atom is then followed to its first encounter with a lattice atom, at which the collision is treated by two-body classical considerations with a realistic inter-atomic potential. The products of this collision are then followed to their collision, and so on. A bookkeeping scheme is used to keep track of the currently moving atoms in the cascade. Allowance is made for moving atoms to interact with interstitials already produced in preceding collisions, so that interference between different branches in the cascade can occur. The cascade is considered to be terminated when no moving atom has energy greater than some critical threshold energy. These calculations enabled scientists to study cascades produced by PKAs of energies in the order of KeV.

The fate of a beam of ions impinging on a target material can be simulated. The target may be amorphous or crystalline. In the latter case, a simple system can be used for creating a small section of the crystal for each target atom and thereby avoiding the storage

of the whole crystal. Like Beeler's method, binary collision is assumed, and the cascades developed by the ions are followed sequentially. For energies in excess of about 1 keV electronic loss is included. The incident beam can be simulated by selecting many ions with initial conditions sampled from the overall distribution of possible systems parameters, then each ion is simulated individually in the interaction with the target. The distribution of the outcomes is constructed by adding them together. This sampling procedure is known as Monte Carlo and will be discussed in the following section. Recent reviews on the MBI and BCA methods have been made by Beeler [8] and Jackson [9].

IV-4. Monte Carlo Technique

The Monte Carlo method may briefly be described as an artificial device of studying a stochastic model of a physical or mathematical process. This is achieved by a sampling process from the probability laws which govern the process under consideration. The physical process of interest in this study is the transport of ions in a heterogeneous material.

The Monte Carlo method has been applied to ion transport by many authors. This will be briefly reviewed at the end of this chapter. First we introduce the method and some necessary definitions, then simple examples will be given to illustrate the concept of the method.

IV-4-1. Definitions

If a random variable x takes any value in the range (a,b) according to a certain function p(x), and if p(x) is normalized, i.e.

$$\int_a^b p(x)\, dx = 1 \quad , \tag{4.1}$$

then p(x) is called the probability density function (PDF). The cumulative distribution function (CDF) for a continuous random variable x, $F(x_o)$, is defined to be the fraction of all x values lying in the range $a < x < x_o$. The PDF p(x) describes the local density of the x values in the increment dx in the range (a,b), so that the probability that the variable x will have the value between x_o and $x_o + dx_o$ is $p(x_o)\, dx_o$. This means that $p(x_o)\, dx_o$ gives the fraction of all values of x in the interval dx_o around x_o.

The CDF F(x) is related to the PDF p(x) through the relation

$$F(x) = \int_a^x p(x_o)\, dx_o \quad , \tag{4.2}$$

with $p(x_o) = 0$ for $b < x_o < a$ and $p(x_o) > 0$ for $a < x_o < b$.

From the definition of F(x) we can state the following properties of F(x):

(a) F is monotonic nondecreasing function of x;

(b) $F(a) = 0$ and $F(b) = 1$;

(c) $F(x_2) - F(x_1)$ = probability that x lies in the interval $x_1 < x < x_2$.

We should note that the random variable may be continuous or discrete. In the latter case if x takes the discrete values

$x_1, x_2, \ldots$, with the probabilities p_1, p_2, ..., so that $\sum_i p_i = 1$, then $F(x)$ is

$$F(x) = \sum_{x_i < x} p_i \quad . \tag{4.3}$$

In such a case, the CDF is not continuous, but a step function with a step height p_i at the point x_i. On the other hand, if the random variable x is continuous, the derivative of $F(x)$ exists and from Eq. (4.2) we have:

$$dF(x) = p(x)\, dx \quad . \tag{4.4}$$

If $g(x)$ is a function of x, then the mean value (the expectation value) of g is

$$\overline{g} = \int g(x)\, dF(x) \quad . \tag{4.5}$$

For a continuous random variable (RV) one gets

$$\overline{g} = \int g(x)\, p(x)\, dx \quad . \tag{4.6}$$

Sometimes we may transform the variable x to another variable y which is related to x by a one-to-one relation, i.e.

$$x = f(y) \quad , \quad y = f^{-1}(x) \quad . \tag{4.7}$$

Hence, the CDF $F(x)$ may take the form

$$F(x) = \int_a^x dF = \int_a^{x(y)} p(u)\left(\frac{du}{dy}\right) dy \quad , \tag{4.8}$$

from which we get

$$dF = p(x(y))\ (dx/dy)\ dy$$
$$= p(x(y))\ (df/dy)\ dy \quad . \tag{4.9}$$

The function $p(x(y))(df/dy)$ is actually the PDF of the random variable y which describes the probability density function of the same set of events which has been described by the random variable x.

More information about the properties of PDF and CDF can be found in any standard statistical textbook [10].

IV-4-2. Sampling Technique [11-14]

The basic idea of the Monte Carlo (MC) method is to select samples which are distributed according to a certain probability law. In other words, how can the values of a certain RV-x be selected so that these values of x are distributed according to the PDF or the CDF of x.

Consider a RV-η with PDF $p(x)$ and consider also a sequence of random numbers (RN) $\rho_1, \rho_2, \ldots$ which satisfy the condition $0 < \rho_i < 1$ and which are drawn independently from a uniform density on the unit interval (0,1). The PDF of these sequences of RNs can be described as

$$g(\rho) = \begin{cases} 1 & 0 < \rho < 1 \\ 0 & \text{otherwise} \end{cases} \quad . \tag{4.10}$$

Let $F(x)$ be the CDF of η, then

$$F(x) = P[\eta < x] = \int_{-\infty}^{x} f(t)\ dt \quad , \tag{4.11}$$

where the notation P[ ] means the probability described by the conditions between the brackets, and we assume that x extends from $-\infty$ to $+\infty$. Consider the equation

$$F(x) = \rho \quad . \tag{4.12}$$

From the properties of the CDF F(x), as x varies from $-\infty$ to $+\infty$, ρ ranges from 0 to 1. Now if we define a uniform function $\phi(\rho)$ such that

$$\phi(\rho) = x \tag{4.13}$$

then it is clear that $\phi(F(x)) = x$ so that (Fig. 4-1)

$$\phi(\rho) < x \quad \text{if and only if } \rho < F(x) \quad . \tag{4.14}$$

The functions ϕ and F are the inverses of each other.

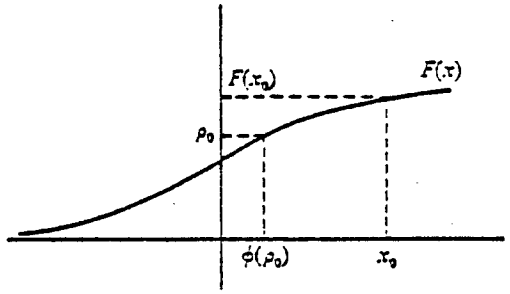

Fig. 4-1.

For the sequence of RNs $\rho_1,\rho_2,\ldots$, the numbers $t_1,t_2,\ldots$ are defined as

$$t_i = \phi(\rho_i) \quad , \tag{4.15}$$

and will be sampled from the density p(x), since

$$P[t_i,x] = P[\phi(\rho_i) < x] = P[\rho_i < F(x)] = F(x) \quad . \tag{4.16}$$

To illustrate this procedure consider the PDF f(x) given by

$$\begin{aligned} f(x) &= \Sigma\, e^{-\Sigma x} \qquad 0 < x < \infty \\ &= 0 \qquad\qquad\quad x < 0 \end{aligned} \quad , \tag{4.17a}$$

which describes the probability that a particle will travel a distance x before having its first collision between x and x + dx in an infinite medium of material with a total macroscopic cross section Σ. Then the CDF F(x) is

$$F(x) = \int_0^x \Sigma\, e^{-\Sigma x}\, dx = 1 - e^{-\Sigma x} \quad . \tag{4.17b}$$

To select a sample from f(x) with uniformly distributed RNx, ρ, we can find the inverse function $\phi(\rho)$, as follows:

$$\rho = F(x) = 1 - e^{-\Sigma x} \quad , \tag{4.18}$$

and hence

$$x = \phi(\rho) = -\left(\frac{1}{\Sigma}\right) \ln (1 - \rho) \quad . \tag{4.19}$$

Then, for the RNs ρ_i, the numbers $\phi(\rho_i)$ will be exponentially distributed according to Eq. (4.17a).

Thus, in principle, once we know the PDF or the CDF of the RV, according to this inversion procedure, we can select a set of values which obeys the prescribed PDF. There exist other methods for sampling and a good review of them is given in Reference [12].

IV-4-3. Accuracy of Monte Carlo Method [13]

It can be shown by statistical analysis that the error in the Monte Carlo solution δ for the mean value of a distribution is of the order

$$\delta \sim \frac{1}{\sqrt{N}} \quad , \tag{4.20}$$

where N equals the number of trials or the number of points in the sample. This means that the mean value predicted from the sample is approaching the mean value of the distribution with increasing N. It can also be shown that the variance σ_o^2 of the arithmetic mean of a RV predicted from the sample is related to the variance of the distribution σ^2 by

$$\sigma_o = \frac{\sigma}{\sqrt{N}} \quad . \tag{4.21}$$

It is clear from Eqs. (4.20) and (4.21) that, for example, if a tenfold increase in the accuracy is required a hundredfold increase in the number of trials N is required, which means increasing the computational time by the same amount.

However, the Monte Carlo method remains the only way one can use to solve multi-dimensional complicated problems when one cannot solve them by any other tools.

IV-5. Applications of Monte Carlo Method in Radiation Damage Studies

Yoshida [4] and Oen et al. [15,16] were the first to use the Monte Carlo technique in radiation damage studies. Since the trajectory of a moving particle in the material can be thought of as a recurrence of a basic cycle, which in turn consists of a step length and a deflection, the simulation of the deflection, i.e. the scattering event, and the step length between collisions differs from one model to another. For example, Yoshida assumed that the collisions of the PKAs produced by neutron irradiation with target atoms are isotropic. Thus, if E_{i-1} is the energy of the moving particle after the $(i-1)^{th}$ collision, then its energy after the i^{th} collision is

$$E_i = \xi E_{i-1} \quad , \tag{4.22}$$

where ξ is the random number. The scattering angle in the i^{th} collision is then readily evaluated to be

$$\theta_i = \cos^{-1} \sqrt{E_i / E_{i-1}} \quad , \tag{4.23}$$

The azimuthal scattering angle is

$$\phi_i = 2\pi\xi \quad . \tag{4.24}$$

Yoshida used exponential distribution for the step length, i.e.

$$p(\ell_i)\, d\ell_i = \frac{1}{\lambda_i} \exp\left(-\frac{\ell_i}{\lambda_i}\right) d\ell_i \quad . \tag{3.2}$$

ℓ_i can then be obtained from

$$\ell_i = -\lambda_i \log \xi \quad , \tag{4.25}$$

where λ_i is the mean free path given by

$$\lambda_i = \frac{1}{N} \pi R_i^2 \tag{4.26}$$

where N is the number of atoms per unit volume, and R_i is the distance of closest approach. R_i was obtained by equating the PKAs energy to Bohr potential

$$E_i = \left(\frac{Ze}{R_i}\right)^2 \exp\left(-\frac{R_i}{a}\right) \quad . \tag{4.27}$$

In the model of Oen et al. [15,16], the target was assumed to consist of touching spheres of influence surrounding each atom. The diameter of each sphere is equal to the distance of the nearest neighbor ($2R_c$). The CM scattering angle was calculated from

$$\Theta = \pi - 2s \int_0^{U_o} \frac{du}{\left\{1 - [V(u)/E_{rel}] - s^2u^2\right\}^{1/2}} \quad , \tag{4.28}$$

where s ≡ the impact parameter which was selected from the distribution

$$P(s)\, ds = \frac{2s\, ds}{R_c^2} \qquad 0 \leq s < R_c$$

$$= 0 \qquad \text{otherwise} \quad , \tag{4.29}$$

$u \equiv 1/r$, where r equals the relative separation, E_{rel} is the relative energy in CM $\equiv M_2E/(M_1 + M_2)$, M_1 and M_2 are the masses of the target atom and the moving particle respectively, and u_o is the value of u for which the denominator of the integrand of Eq. (4.28) vanishes.

The azimuthal scattering angle was evaluated from Eq. (4.24). Oen et al. used the hard sphere potential and Bohr potential. They used a screening length equal to Bohr's screening length multiplied by a factor to permit a closer fit to experimental results. In the evaluation of the step length they introduced the concept of the "free flight distance", $\bar{\ell}_{ff}$ which is the average distance travelled by the moving particle in the unoccupied space between the atom spheres. This distance was added to the path of the primary along with the segments ℓ_1 and ℓ_2 of the asymptotes of the primary at each collision (Fig. 4-2). The value of $\bar{\ell}_{ff}$ is chosen so that the effective mean free path arising from the calculation matches the ordinary analytical mean free path (Eq. 4.26), whose value is given by

$$\bar{\ell}_{ff} = \left(1/n\pi R_c^2\right) - \frac{4}{3} R_c \quad . \tag{4.30}$$

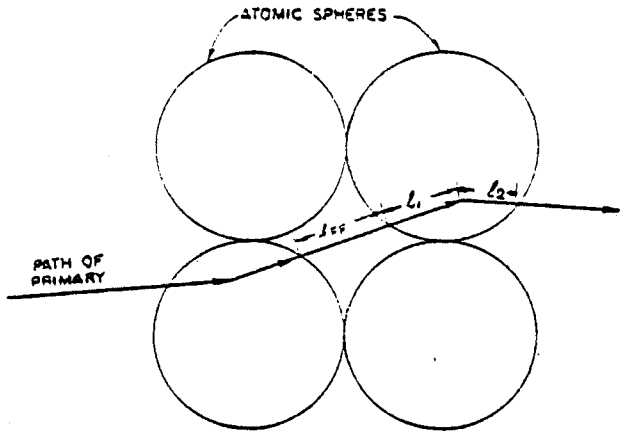

Fig. 4-2. Path of a primary atom showing a typical "free flight" distance ℓ_{ff}[15].

The electronic energy loss was neglected in the above models, which are given here in some detail to illustrate the method. Pavlov et al. [17] calculated the distribution of defects formed during the ion bombardment, including the electronic energy loss, and assumed it was continuous along the path. They followed all the moving atoms in the cascade and recorded all types of events that may take place in the collision, i.e. displacement, replacement, reflection, etc.

Skoog et al. [18-19] considered only the nuclear energy loss and used the universal scattering cross section Eq. (2.10), i.e.

$$\frac{d\sigma}{d\eta} = -\pi a^2 \frac{f(\eta)}{\eta^2} \quad , \tag{4.31}$$

where $\eta = t^{1/2} = \varepsilon \sin(\theta/2)$. From this equation the CDF $F(\eta)$ can be obtained for the variable η. They assumed constant path length given by

$$\ell = \frac{1}{\pi r_o^2 N} \tag{4.32}$$

where r_o is the maximum allowed impact parameter defined by $\pi r_o^2 = N^{-2/3}$ where N is the atomic density of the target. The function $f(t^{1/2})$ is assumed to be approximated to TF potential by

$$\begin{aligned} f(\eta) &= 0.25\ \eta^{-1/3} \qquad \eta > 0.158 \\ &= 0.86\ \eta^{1/3} \qquad \eta < 0.158 \end{aligned} \tag{4.33}$$

The function that was used is shown in Fig. 4-3. The total cross section, due to the restriction of a binary collision, is normalized to

$$F(\eta)_{max} = \int_{\eta_o}^{\varepsilon} \left(\frac{d\sigma}{d\eta}\right) d\eta = \pi r_o^2 \quad . \tag{4.34}$$

Skoog et al. [18] were interested in studying the angular distribution of ions incident on a thin layer as well as the angular and thickness dependences of the nuclear stopping cross section.

Many other authors [20-36] used the Monte Carlo technique to study the range, damage, backscattering, and sputtering of the ions in solids, and the reader is urged to review those papers for more information.

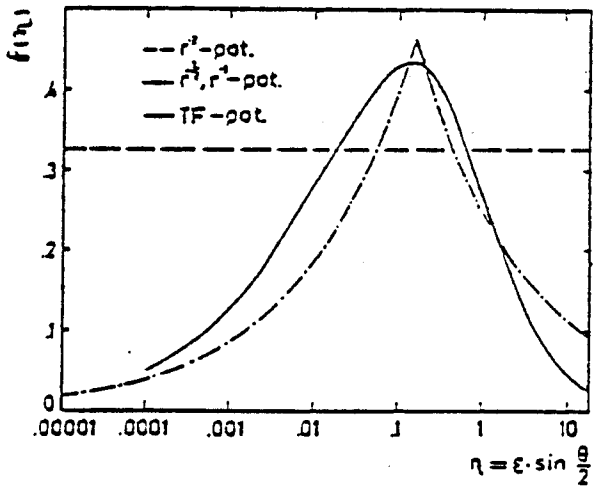

Fig. 4-3. The scaling function f(η) of the TF, used by Skook et al. [18].

References for Chapter IV

1. G. H. Vineyard, J. B. Gibson, A. N. Goland, and M. Milgram, Bull. Am. Phys. Soc. 5, 26 (1960).

2. J. B. Gibson, A. N. Goland, M. Milgram, and G. H. Vineyard, Phys. Rev. 120, 1229 (1960).

3. G. H. Vineyard, "Interatomic Potentials and Simulation of Lattice Defects," eds. P. C. Gehlen, J. R. Beeler, Jr., and R. I. Jaffee, Plenum Press, New York, 13, (1972).

4. M. Yoshida, J. Phys. Soc. Jap. 16, 44 (1961).

5. M. T. Robinson and O. S. Oen, Phys. Rev. 132, 2385 (1963).

6. J. R. Beeler, Jr. and D. G. Besco, J. Appl. Phys. 34, 2873 (1963).

7. J. R. Beeler, Jr., Phys. Rev. 150, 470 (1966).

8. J. R. Beeler, Jr., "Advances in Materials Research," Vol. 4, ed. H. Herman, John Wiley & Sons, Inc., (1970), p. 295.

9. D. P. Jackson, Proc. Int. Conf. on Atomic Collisions in Solids, 5th, Gatlinburg, Tenn., 1973. Eds. S. Datz, B. R. Appleton, and C. D. Moak, Plenum, New York, (1975), p. 185.

10. M. G. Kendall and A. Stuart, "The Advanced Theory of Statistics," Vol 1. 3rd ed., Charles Griffein & Comp. Lim., London (1969).

11. J. Spanier and E. M. Gelbard, "Monte Carlo Principles and Neutron Transport Problem," Adison Wesley (1969).

12. J. H. Hammersley and D. C. Handscomb, "Monte Carlo Methods," Methuen & Co. LTD, London (1964).

13. N. P. Buslenko, D. I. Golenko, Yu. A. Schreider, I. M. Sobol, and V. G. Sragovich, "The Monte Carlo Method 'The Method of Statistical Trials'," ed. Yu. A. Schreider, Pergamon Press, London (1966).

14. E. D. Cashewell and C. J. Everett, "A Practical Manual on the Monte Carlo Method, for Random Walk Problems," Pergamon Press, (1959).

15. O. S. Oen, D. K. Holmes, and M. T. Robinson, J. Appl. Phys. 34, 302 (1962).

16. O. S. Oen and M. T. Robinson, J. Appl. Phys. 35, 2515 (1964).

17. P. V. Pavlov, D. I. Tele'baum, E. I. Zorin, and V. I. Aleksew. Sovit Physico - Solid State 8, 2141 (1967).

18. R. Skoog and G. Hagberg, Rad. Eff. 22, 277 (1974).

19. R. Skoog, Comp. Phys. Comm. 7, 392 (1974).

20. M. J. Berger, Methods in Computational Physics, Vol. 1, 135 (1963).

21. T. Ishitani, K. Murata, and R. Shimizu, Japan J. Appl. Phys. 10, 1464 (1971).

22. T. Ishitani, R. Shimizu, and K. Murata, Japan J. Appl. Phys. 11 125 (1972).

23. T. Ishitani, R. Shimizu, and K. Murata, Phys. Stat. Sol. (b) 50, 681 (1972).

24. T. Ishitani and R. Shimizu, Phys. Letters 46A, 487 (1974).

25. T. Ishitani, R. Shimizu, and H. Tamura, Japan J. Appl. Phys. Suppl. 2, Pt. 2, (1974).

26. T. Ishitani and R. Shimizu, Appl. Phys. 6, 241 (1975).

27. J. E. Robinson and S. Agamy, Proc. Int. Conf. on Atomic Collision in Solids, 5th, Gatlinburg, Tenn., 1973. Eds. S. Datz, B. R. Appleton, and C. D. Moak, Plenum, New York (1975), p. 215.

28. J. E. Robinson, Rad. Eff. 23, 29 (1974).

29. D. A. Thompson and J. E. Robinson, J. Nucl. Instrum. Methods 132, 261 (1976).

30. K. Guttner and G. Munzenberg, Proc. Int. Conf. on Atomic Collision in Solids, 5th, Gatlinburg, Tenn., 1973. Eds. S. Datz, B. R. Appleton, and C. D. Moak, Plenum, New York (1975), p. 201.

31. K. Guttner, H. Ewald and H. Schmidt, Rad. Eff. 13, 111 (1972).

32. K. Guttner, Z. Naturforsch 26a, 1290 (1971).

33. L. G. Haggmark and W. D. Wilson, SAND77-8755, (1978).

34. G. Betz, R. Dobrozemsky, and F. Vienbock, Int. J. Mass Spectrom. Ion Phys. 6, 451 (1971).

35. J. H. Ormrod, J. R. MacDonald, and H. E. Duckworth, Can J. Phys. 43, 275 (1965).

36. R. S. Walker and D. A. Thompson, Rad. Eff. 37, 113 (1978).

CHAPTER V

THE COMPUTATIONAL MODEL

V-1. Introduction

To study the effect of the microstructure on the range and damage of implanted ions in the materials, a three-dimensional Monte Carlo Code called HERAD (Heterogeneous Radiation Damage) was developed which is capable of predicting the range and the damage in homogeneous or inhomogeneous materials, e.g. materials which contain voids or bubbles. Even though most of the time spent on this thesis involved adapting various theoretical models to the computer, only an outline of the code is given here. Future reports [22] will document the code in more detail.

V-2. Assumptions

The model is based on the following assumptions:

(a) the moving particle interacts with one atom at a time, i.e. the elastic binary collision approximation is assumed;

(b) the target is assumed amorphous, i.e. we neglect any lattice effects;

(c) the moving particle loses energy to electrons continuously while it travels between successive collisions;

(d) the magic formula of Lindhard [1] is used to evaluate the scattering angle;

(e) the steps between successive collisions are assumed exponentially distributed according to Eq. (3.2), i.e. the mean free path assumption is taken;

(f) the moving particle is assumed to be stopped when its energy falls below a cutoff energy (~ 25 eV).

V-3. Calculation Procedure

V-3-1. Nuclear Energy Loss in a Scattering Event

The universal differential scattering cross section given by Lindhard et al. [1] is

$$d\sigma = \frac{1}{2}\,\pi a^2\, t^{-3/2}\, f(t^{1/2})\, dt \quad , \tag{5.1}$$

where a is the screening length given by

$$a = 0.8853\, a_o \frac{k}{g(Z_1,Z_2)} \quad . \tag{5.2}$$

a_o is Bohr radius = $.529 \times 10^{-8}$ cm, and $g(Z_1,Z_2)$ is obtained either from Lindhard's formula

$$g(Z_1,Z_2) = (Z_1^{2/3} + Z_2^{2/3})^{1/2} \quad , \tag{5.3}$$

or from Firsov's formula

$$g(Z_1,Z_2) = (Z_1^{1/2} + Z_1^{1/2})^{2/3} \quad . \tag{5.4}$$

The factor k in Eq. (5.2) is introduced to study the effect of the screening length on the calculations results. $t^{1/2}$ is given by $t^{1/2} = \varepsilon \sin \theta/2$, where θ is the CM scattering angle, ε is the reduced energy

$$\varepsilon = E \frac{M_2}{M_1 + M_2} \frac{a}{Z_1 Z_2 e^2} \quad , \tag{5.5}$$

M_1 and Z_1 are the mass and the atomic number of the moving particle,

M_2 and Z_2 are the mass and the atomic number of the target atom, E is the energy of the moving particle and e is the electronic charge. $f(t^{1/2})$ is given by Winterbon [2] as

$$f(t^{1/2}) = \lambda t^{1/2-m} [1 + (2\lambda t^{1-m})^q]^{-1/q} \quad , \tag{5.6}$$

which is valid for $0.001 < t^{1/2} < 10$, and approaches a simple analytical form

$$f_L(t^{1/2}) = \lambda t^{1/2-m} \quad , \tag{5.7}$$

for small values of $t^{1/2}$. For large values of $t^{1/2}$ ($t^{1/2} > 10$), we use the expression

$$f_U(t^{1/2}) = 0.5\ t^{-1/2} \quad , \tag{5.8}$$

which corresponds to Rutherford scattering [3]. The three different regions for $f(t^{1/2})$ are shown in Fig. 5-1 for the Thomas-Fermi and Moliere potentials. For very low energies where the screening effect is excessive, we use the Born-Mayer potential. The function $f(t^{1/2})$ of the Born-Mayer potential is given by Sigmund [4] as

$$f_{BM}(t^{1/2}) = 24t^{1/2} \quad . \tag{5.9}$$

The differential cross section is given by

$$d\sigma = (\pi a_{BM}^2) \frac{(24t^{1/2})}{2t^{3/2}}\, dt \quad , \tag{5.10}$$

where a_{BM} equals 0.219 Å. Sigmund [4] estimated a limiting energy E_{BM} given by

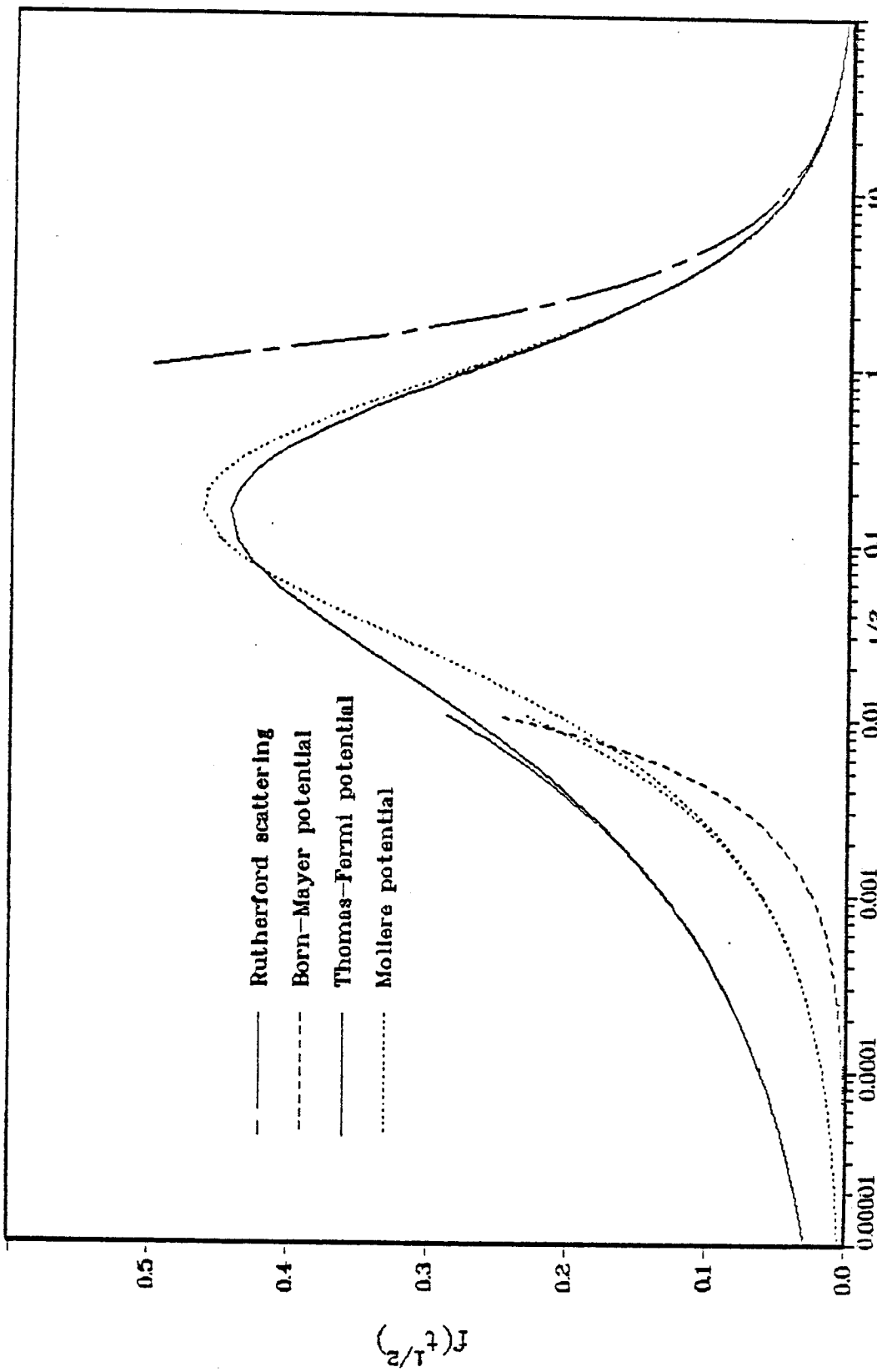

Fig. 5-1. The universal scattering function for Thomas-Fermi, Mollere, and Born-Mayer potentials.

$$E_{BM} = k_{BM} \left[0.0234 \frac{M_1 + M_2}{M_2} \left(\frac{a_{12}}{a_{BM}}\right)^3 \cdot \frac{Z_1 Z_2 e^2}{a_{12}}\right] , \tag{5.11}$$

below which Eq. (5.10) can be used. a_{12} is the screening length for the colliding atoms given by Eq. (5.2) and we introduce the factor k_{BM} to allow for the change of E_{BM}. Alternatively, E_{BM} can be assigned an input value.

Another choice for very low energy scattering is assuming isotropic scattering in the CM [5] with

$$d\sigma = \frac{\sigma_g}{2} \sin\theta \, d\theta , \tag{5.12}$$

where σ_g is the total effective cross section given by

$$\sigma_g = \pi P_c^2 , \tag{5.13}$$

where $2P_c$ is the average distance between the target atoms.

The total scattering cross section is given by

$$\sigma_T = \int_{t_{min}^{1/2}}^{t_{max}^{1/2}} d\sigma , \tag{5.14}$$

where $d\sigma$ is given by either Eq. (5.1) together with Eqs. (5.6), (5.7), and (5.8), Eq. (5.10), or Eq. (5.12), depending on the energy of the particle, the choice of the potential and the value of $t_{min}^{1/2}$,

$t_{min}^{1/2} = \varepsilon \sin(\theta_{min}/2)$,

$t_{max}^{1/2} = \varepsilon$,

and θ_{min} is the minimum angle of scattering which can be calculated from Eqs. (2.23), (2.24), (2.25), and (2.26), or assigned a constant value (~ 2°).

The scattering angle is determined from the expression

$$\int_{t_{min}^{1/2}}^{t^{1/2}} d\sigma/\sigma_T = \rho \quad , \tag{5.15}$$

where ρ is a random number uniformly distributed from 0 to 1. The actual value of the scattering angle, θ, is then evaluated from the value of $t^{1/2}$ which satisfies Eq. (5.15) via

$$\theta = 2. \sin^{-1} \left(\frac{t^{1/2}}{\varepsilon}\right) \quad . \tag{5.16}$$

The nuclear energy loss is given by

$$\Delta T = \gamma E \sin^2 \frac{\theta}{2} \quad , \tag{5.17}$$

where $\gamma = 4M_1M_2/(M_1 + M_2)^2$, and E is the energy of the particle before collision.

The polar scattering angle of the scattered particle in the laboratory, ψ_1, can be obtained from the familiar relation

$$\tan \psi_1 = \frac{A \sin \theta}{(1 + A \cos \theta)} \quad , \tag{5.18}$$

where $A = M_2/M_1$. The corresponding angle of the struck particle is

$$\psi_2 = \frac{\pi}{2} - \frac{\theta}{2} \quad . \tag{5.19}$$

Since the scattering in the azimuthal plane is isotropic, the

azimuthal scattering angle θ is uniformly distributed from 0 to π, and is determined from

$$\phi = 2\pi\rho \quad , \tag{5.20}$$

where ρ is another random number.

The directions of the scattered particle and the target atom (the scatterer) after any collision can be determined from the above quantites as described below. Consider that the particle moves along the vector $\overline{H}$ (see Fig. 5-2) before the collision and has direction cosines a_1, b_1, and c_1. If no scattering event occurs, the particle will continue to move along $\overline{H}$. Suppose that the particle at any point P along $\overline{H}$ suffers a collision which results in a deflection of its path with respect to $\overline{H}$ by the angle ψ_1 given by Eq. (5.18), and suppose that the particle continues to travel a unit length S. The end point of S, due to the fact that the scattering can happen in any plane containing H, may be at any point along the perimeter of the base of a cone whose altitude is the extension of $\overline{H}$.

The altitude of the cone L and its base radius will be

$$L = \cos \psi_1 \quad ,$$

and (5.21)

$$R = \sin \psi_1 \quad ,$$

respectively. The coordinates of the center of the cone base x_o, y_o, and z_o with respect to the point of collision P are given by

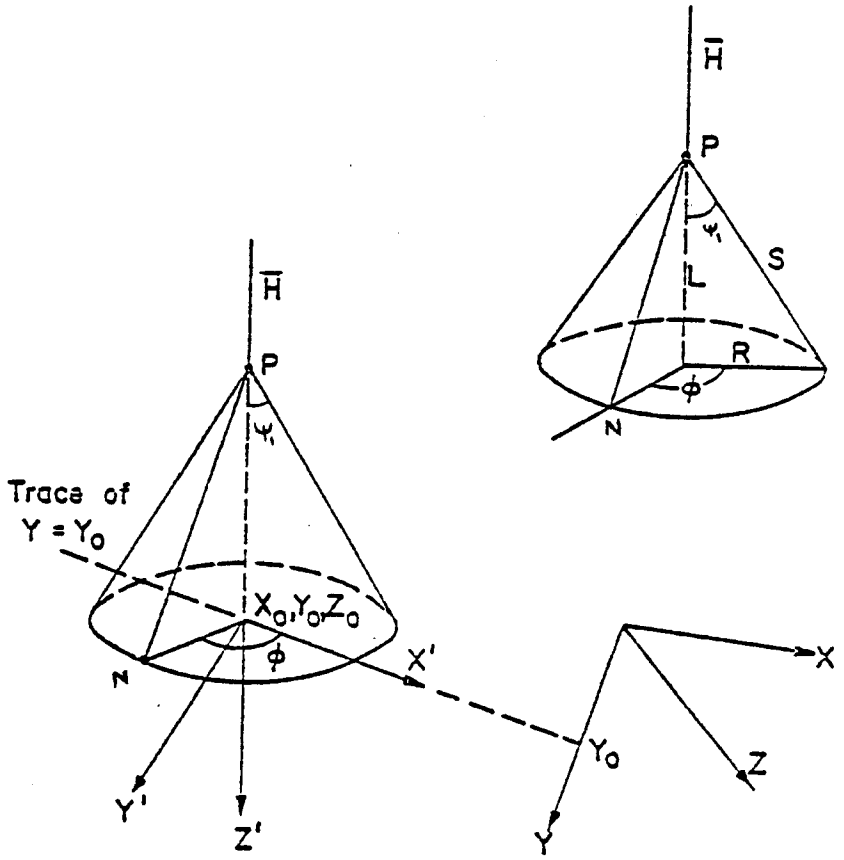

FIGURE 5-2. COORDINATE SYSTEMS USED TO LOCATE THE POINT OF COLLISION.

$$x_o = L \cdot a_1 \quad ,$$

$$y_o = L \cdot b_1 \quad , \tag{5.22}$$

$$z_o = L \cdot c_1 \quad .$$

A new coordinate system is used with axes X', Y', Z' chosen such that the X'Y' plane contains the base of the cone, and Z' coincides with $\overline{H}$, i.e.

$$a_{Z'} = a_1 \quad , \quad b_{Z'} = b_1 \quad , \quad \text{and} \quad c_{Z'} = c_1 \quad . \tag{5.23}$$

Since the X' axis is arbitrary, it is chosen to be the line of the intersection of the plane of the base with the plane $Y = y_o$. The equation of the cone base in terms of the direction cosines of the normal to it ($\overline{H}$), and a point in the plane (x_o, y_o, z_o) is then

$$a_1 x + b_1 y + c_1 z - (a_1 x_o + b_1 y_o + c_1 z_o) = 0 \quad . \tag{5.24}$$

Note that the collision point P is considered as the origin of the original coordinate system XYZ. The line of intersection of the base with the plane $Y = y_o$ is

$$a_1 x + c_1 z - (a_1 x_o + c_1 z_o) = 0 \quad , \tag{5.25}$$

which leads to an equation for the line of the intersection (X'), given by

$$z = \left(-\frac{a_1}{c_1}\right)x + \left(\frac{a_1}{c_1}\right)x_o + Z_o \quad . \tag{5.26}$$

Therefore, the direction cosines of the X' axis with respect to the

original axes are

$$a_{X'} = \cos\,(\arctan\,(-a_1/c_1)) \quad ,$$

$$b_{X'} = \cos\,(\pi/2) = 0 \quad , \tag{5.27}$$

and $$c_{X'} = \cos\,(\arctan\,(-c_1/a_1)) \quad .$$

The direction cosines of the Y' axis, knowing that of X' and Z' are

$$a_{Y'} = b_{Z'}c_{X'} \quad ,$$

$$b_{Y'} = c_{Z'}a_{X'} - c_{X'}a_{Z'} \quad , \tag{5.28}$$

$$c_{Y'} = -a_{X'}b_{Z'} \quad .$$

The azimuthal angle ϕ is chosen with respect to X' axis by Eq. (5.20). Then the coordinates of the point N (Fig. 5-2) in the X'Y'Z' system are

$$x'_N = R\cos\,\phi$$

$$y'_N = R\sin\,\phi \tag{5.29}$$

$$z'_N = 0 \quad ,$$

which can be transformed back to the original system XYZ whose origin is the point P to give

$$x_N = a_X, x'_N + a_Y, y'_N + x_o \quad ,$$

$$y_N = b_X, x'_N + a_Y, y'_N + y_o \quad , \tag{5.30}$$

$$z_N = c_X, x'_N + a_Y, y'_N + z_o \quad .$$

Finally the new direction cosines of the scattered particle are

$$a_n = x_n/D \quad , \quad b_n = y_n/D \quad , \quad c_n = z_n/D \quad , \tag{5.31}$$

where

$$D = (x_N^2 + Y_N^2 + Z_N^2)^{1/2} \quad . \tag{5.32}$$

The direction cosines of the scatterer are obtained by solving the vector equations

$$\bar{s} \cdot \bar{P}_1 = \cos \psi_2 \quad ,$$

$$\bar{s} \cdot \bar{P}_2 = \cos (\psi_1 + \psi_2) \quad , \tag{5.33}$$

and $$(\bar{P}_1 \times \bar{P}_2) \cdot \bar{s} = 0 \quad ,$$

where $\bar{P}_1$ is a unit vector in the direction of the moving particle before collision, $\bar{P}_2$ is a unit vector in the direction of the particle after collision, $\bar{s}$ is a unit vector in the direction of the displaced atom, ψ_1 is the laboratory scattering angle given by Eq. (5.18), and ψ_2 is the laboratory scattering angle of the scatterer and is given by Eq. (5.19). Figure 5-3 shows the directional relations among the three vectors.

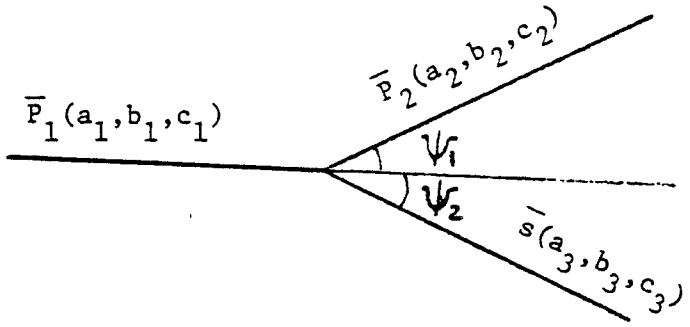

Fig. 5-3. Schematic diagram showing the directions of the moving particle before collision $\bar{P}_1$, after collision $\bar{P}_2$ and the direction of the recoil atom $\bar{s}$.

Equation (5.33) can be put in the following form

$$
\begin{aligned}
a_s a_1 &+ b_s b_1 &+ c_s c_1 &= \cos\psi_1 \\
a_s a_2 &+ b_s b_2 &+ c_s c_2 &= \cos(\psi_1 + \psi_2) \\
a_s(b_1c_2 - c_1b_2) &+ b_s(c_1a_2 - a_1c_2) &+ c_s(a_1b_2 - b_1a_2) &= 0
\end{aligned}
\tag{5.34}
$$

where (a_1,b_1,c_1) are the direction cosines of $\bar{P}_1$, (a_2,b_2,c_2) are the direction cosines of $\bar{P}_2$, and (a_3,b_3,c_3) are the direction cosines of $\bar{s}$.

V-3-2. Step Length Between Two Successive Collisions and the Electronic Energy Loss

The step length, ℓ, between two successive nuclear collisions is assumed to be exponentially distributed, i.e.

$$p(\ell) = \frac{1}{\sigma_T N} \exp\left(-\frac{\ell}{\sigma_T N}\right) \quad , \tag{5.35}$$

where N is the atomic density of target, and σ_T is the total scattering cross section which is obtained from Eq. (5.14). The value of ℓ is then evaluated from

$$\ell = -\frac{1}{N\sigma_T} \ln(\rho) \quad , \tag{5.36}$$

where ρ is a random number uniformly distributed between 0 and 1.0.

A truncated exponential distribution, which limits the minimum step and/or the maximum step, can also be used. Another constraint on the step length is made such that the electronic energy loss of the particle along the step does not exceed some fraction (~ 5%) of the energy of the particle at the beginning of the step. Such constraint was also used by Biersack [6].

The electronic energy loss is assumed to be continuous along the path of the particle. If the step length is ℓ and the energy of the particle is E_i at the beginning of the step, then the energy of the particle, E_f, at the end of the step ℓ is given by

$$E_f = E_i - \int_0^{\ell} \left(\frac{dE}{d\ell}\right)_e d\ell \quad , \tag{5.37}$$

and for the first order approximation one gets

$$E_f = E_i - \left(\frac{dE}{d\ell}\right)_e (E_i)\ell \quad . \tag{5.38}$$

The Lindhard [7] or Firsov [8] formulas, Eq. (2.6) and Eq. (2.7) respectively, can be used for $(dE/d\ell)_e = S_e N$, where N is the atomic

density. The Brice [9] formula for S_e can be used also, and is given by

$$S_e = A(Z_1 + Z_2)\, f_b(U)\left[U^{1/2}\left(\frac{(30U^2 + 53U + 21)}{(3 + 3U^2)}\right)\right.$$
$$\left. + (10U + 1)\arctan\left(U^{1/2}\right)\right] , \tag{5.39}$$

where: $A = 0.60961 \times 10^{-15}$ eV cm^2/atom,

$U = E/(Z^2 M_1 E_1)$,

$E_1 = 99.20$ KeV

$f_b(U) = [1 + (4Z^2\, a'^2\, U)^{n/2}]^{-1}$,

and Z, a', and n are the three parameters for projectile target combination.

V-3-3. The Displacement Model

The computer program HERAD is designed to study the range distribution as well as the damage distribution of ions in materials. In the first case, only the incident ions are followed. An approximate estimate of the damage energy, i.e. the amount of energy that results in displacement and defect production, can be made. If ΔT is the energy loss by the incident ion upon a collision with a target atom, E_d is the threshold energy of the displacement, and ΔT is less than E_d, ΔT is assumed to be dissipated into phonons, i.e. heat. If ΔT is greater than E_d, ΔT is partitioned according to Lindhard [10] to a damage energy T_D which ultimately goes to displacement and

electronic energy T_e which is lost to electrons. T_D and T_e are given by

$$T_D = \Delta T/(1 + kg(x)) \quad ,$$

and (5.40)

$$T_e = \Delta T - T_D \quad ,$$

where

$$k = (0.1334\ Z_2^{2/3})/A_2^{1/2} \quad , \tag{5.41}$$

$$x = \Delta T/(0.02693\ Z_2^{7/3}) \quad , \tag{5.42}$$

and [11]

$$g(x) = x + 0.4024\ x^{3/4} + 3.4008\ x^{1/6} \quad . \tag{5.43}$$

The damage energy T_D is supposed to be deposited at the point of collision, such that the spatial distribution of T_D will not include the recoil effect. The number of defects, ν, according to the Kinchin and Pease displacement model [12] is

$$\nu = \frac{T_D}{2E_d} \quad , \tag{5.44}$$

which is based on the hard sphere potential. For more realistic potentials, Eq. (5.44) becomes [11]

$$\nu = \eta \frac{T_D}{2E_d} \quad , \tag{5.45}$$

where η ($\sim$ 80%) is the displacement efficiency which is a function of the interatomic potential.

A more precise estimate of the damage can be made by following the primary knock atoms. In this case, T_D given by Eq. (5.40) is deposited at the end of the PKA trajectory when its energy is less than $2E_d$, i.e. no longer able to produce further displacements. Finally, the defect distribution can be estimated by following every atom in the cascade capable of displacing a target atom. Figure 5-4 shows and explains the displacement model adopted in the calculations. The cutoff energy E_c may be either E_d or $2E_d$ and in both cases a binding energy U_{bin} may be optionally included to account for the amount of energy the recoil atom may expend in breaking its bonds in the lattice. The value of the cutoff energy E_c can also take any pre-assigned value which allows us to compare our results with other calculations that employ different values for E_c, E_d, and U_{bin}.

V-4. Inhomogeneous Target

In dealing with an inhomogeneous material, i.e. a material containing voids or bubbles, we assume that the cavities are randomly distributed in the material with known distributions of the number density and the average diameter, or the distributions of the void fraction of the cavities. It is known [14-16] that

$$V_V = L_L \quad , \tag{5.46}$$

where V_V is the volume fraction of the second phase, and L_L is the

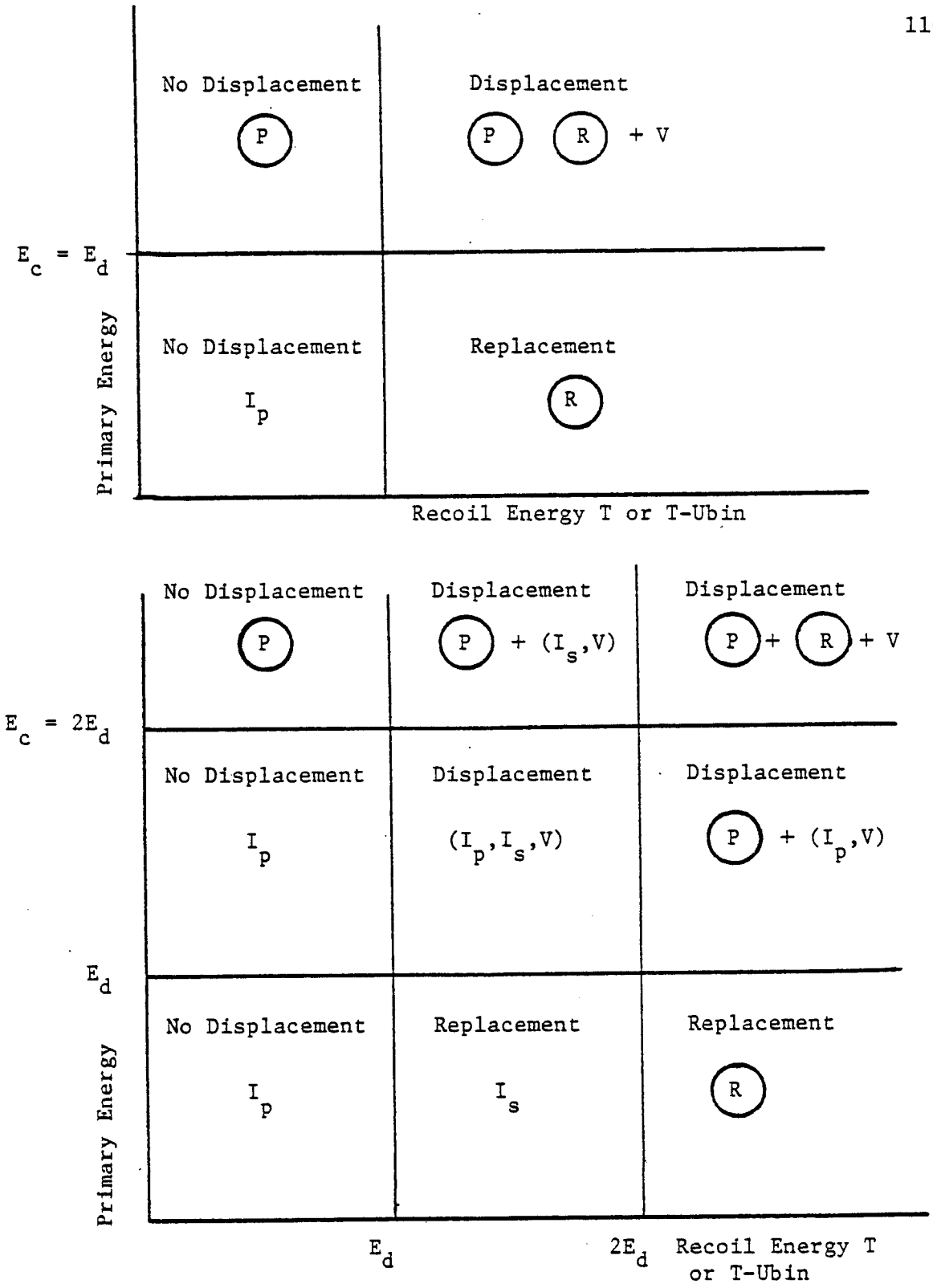

Fig. 5-4. a) The displacement model when the cutoff energy = E_d; b) when the cutoff energy = $2E_d$; P = primary, R = recoil, I_p = interstitial results from a primary, I_s = interstitial results from a secondary; ( ) near defect, ◯ = energetic particle to be followed.

lineal fraction, i.e. the length of lineal intercepts per unit length of a random test line.

This fact has been used by Odette et al. [17] to estimate the effect of voids on the range and damage of ions in materials, but in that work no difference was made between the path of the ion and its projected range. In our calculations the steps between collisions, Eq. (5.36), were increased according to Eq. (5.46) by

$$\Delta\ell = \ell \cdot V_V \quad , \tag{5.47}$$

and the particle energy remains the same as it transverses the void. Thus, in this model the actual path of the moving particles will be affected by the presence of the cavities, rather than the projected range as in the model of Odette et al. [17].

V-5. The Computer Code HERAD

Figure 5-5 shows a block diagram of the computer program HERAD. The name "HERAD" stands for "Heterogeneous Radiation Damage". The following is a brief description of the code and the function of the procedures used in it.

MAIN. MAIN is the starting procedure. It calls ZCRAYF, AINITIAL, and AMAINX.

ZCRAYF. ZCRAYF handles the input/output files according to the computer environments, i.e. if the program is to be run on a CRAY-1 or CDC-7600 machine.

AINITIAL. This subroutine is called twice, first by MAIN to set the physical constants needed in the calculations, and second by

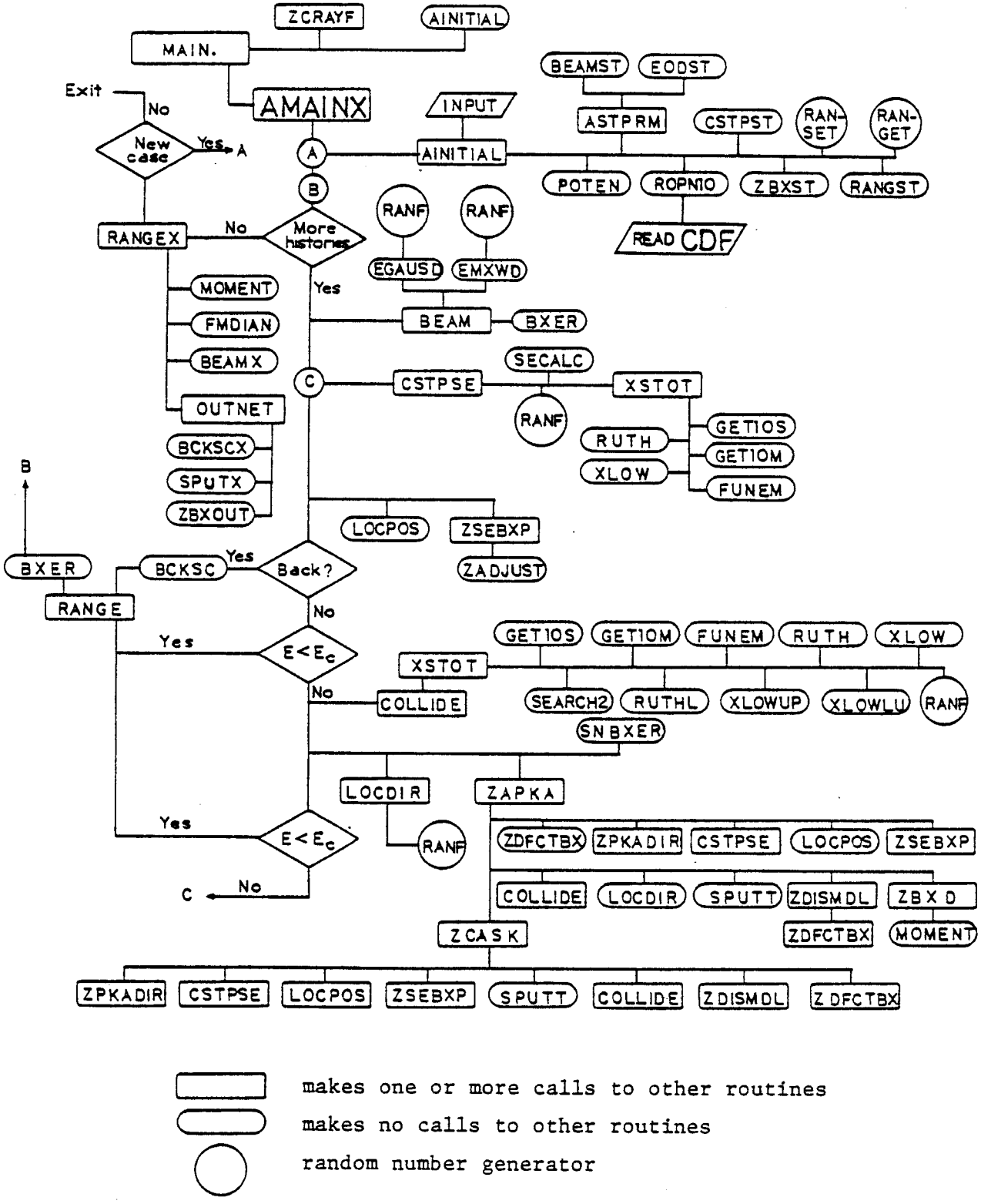

Fig. 5-5. Flow diagram of HERAD.

AMAINX to set some of the input data to their default values and read the input data. AINITIAL calls POTEN, ROPNIO, ZBXST, ASTPRM, and CSTST.

AMAINX. This is the main controller of the program. AMAINX follows the incident ions only, and it calls ZAPKA to follow the PKAs if that is requested.

POTEN. POTEN is used to set the potential constants, used in the calculation of the cross section, λ, m, and q in Eq. (5.6).

ROPHIO. ROPHIO is an entry point in the subroutine ENTRYS, and is called to read the CDF of the potential which resides on an input file produced by the program POTSET.

ASTPRM. ASTPRM calculates most of the parameters and constaints used in other procedures. Also, it calls the setting entry points BEAMST and EODST.

BEAM. BEAM provides the energy of the incident beam of ions. Three different distributions may be used for the incident beam, mono-energetic, Gaussian, or Maxwellian. In the case of the Gaussian distribution the function EGAUSD is used, and in the case of Maxwellian distribution the function EMXWD is used. In both cases a call to BXER is made to record the energy.

EGAUSD. The function EGAUSD uses the Monte Carlo method to sample a Gaussian distribution knowing its mean and its standard deviation. The method employed is known as the sine-cosine method [18,19].

EMXWD. This function also uses the Monte Carlo method to sample a Maxwellian distribution [18].

BXER. BXER is used to record a variable into its associated histogram.

CSTPSE. This procedure outputs the step length between two collisions and the electronic energy loss of the particle along this step. It calls XSTOT, the random number generator RANF, and in case that the Brice formula is used for the electronic energy loss it calls SECALC.

SECALC. SECALC calculates the electronic energy loss according to the Brice formula (Eq. 5.39).

XSTOT. XSTOT calculates the total scattering cross section and the scattering angle.

LOCIR, LOCPOS. LOCDIR determines the direction cosines of the scattered partcle after scattering knowing the angle of scattering. LOCPOS determines the coordinates of the next collision of the particle giving the step length and the direction cosines.

ZSEBXP. ZSEBXP is used to record the electronic energy loss in a histogram.

COLLIDE. Calculates the laboratory scattering angle and the nuclear energy loss in the collision.

ZAPKA. This routine follows the PKAs if requested.

SNBXR. Records the nuclear energy loss of the incident ions in the collisions with respect to the space.

BCKSC. Records the energy of the backscattered particles.

DEEFF. Calculates the partition of the PKA energy into electronic and nuclear energy according to Lindhard, Eqs. (5.40)-(5.42).

ENTRYS. It has the entry points, ROPNIO which was mentioned before, GETIOS, and GETIOM. GETIOS and GETIOM return the values of CDF and the PDF of the scattering cross section.

SPUTT. Calculates the energy distribution of sputtered atoms.

EMEDIAN. Returns the median of a distribution.

FUNEM. Calculates the minimum angle of scattering.

MOMENT. Calculates the average, the standard deviation, the skewness, and the kortosis of a distribution.

RANGE. Calculates the vector range, the projected range, the spread, and the total path at the end of a history and calls BXER to record all the above quantities in their histograms. At the end of all histories the energy points, RANGEX is called to print out these histograms, to call MOMENT, and to print the statistics.

RUTH, XLOW. Calculates the upper and the lower limit of the scattering function, respectively.

SEARCH2. Searches for the value of $t^{1/2}$ which satisfies Eq. (5.15).

ZADJUST. Is called by any scoring routine when the score is out of the limit of the histogram; it then doubles the histogram interval and adjusts the scores in the histogram.

ZBXD. Calculates the distribution of the damage energy transported by the PKAs and the statistics of this distribution.

ZCASK. This routine is called from ZAPKA if all the displaced atoms are to be followed. It follows a displaced atom by a PKA. During the slowing down of this atom, the secondary, ZCASK stores the coordinates, the direction cosines, and the energy of any displaced atom capable of producing more displacements. After the energy of the moving atom falls below the cutoff energy, ZCASK retrieves the latest stored coordinates, directions, and energy and starts another branch in the cascade. This is done until all the stored information is processed.

ZDISMDL. This routine is called by ZAPKA and ZCASK. It employs the displacement model in the collisions and scores the resulting defects by calling ZDFCTBX.

ZPKADIR. Calculates the direction of a recoil atom in a collision.

OUTNET. This is the main output routine. It calculates and prints out a complete energy partition, different energy distributions, collisions distribution, and defects distributions. If plotting is requested, OUTNET writes the desired information on an output file to be processed by the plotting programs.

HERAD can be compiled to include graphic routines which help one to watch the paths of the moving particles, projected on any plane, on a display terminal. This was mainly used as a debugging tool instead of having a huge amount of print output describing the trajectories of the particles at each collision. An example of this output is shown in Fig. 5-6.

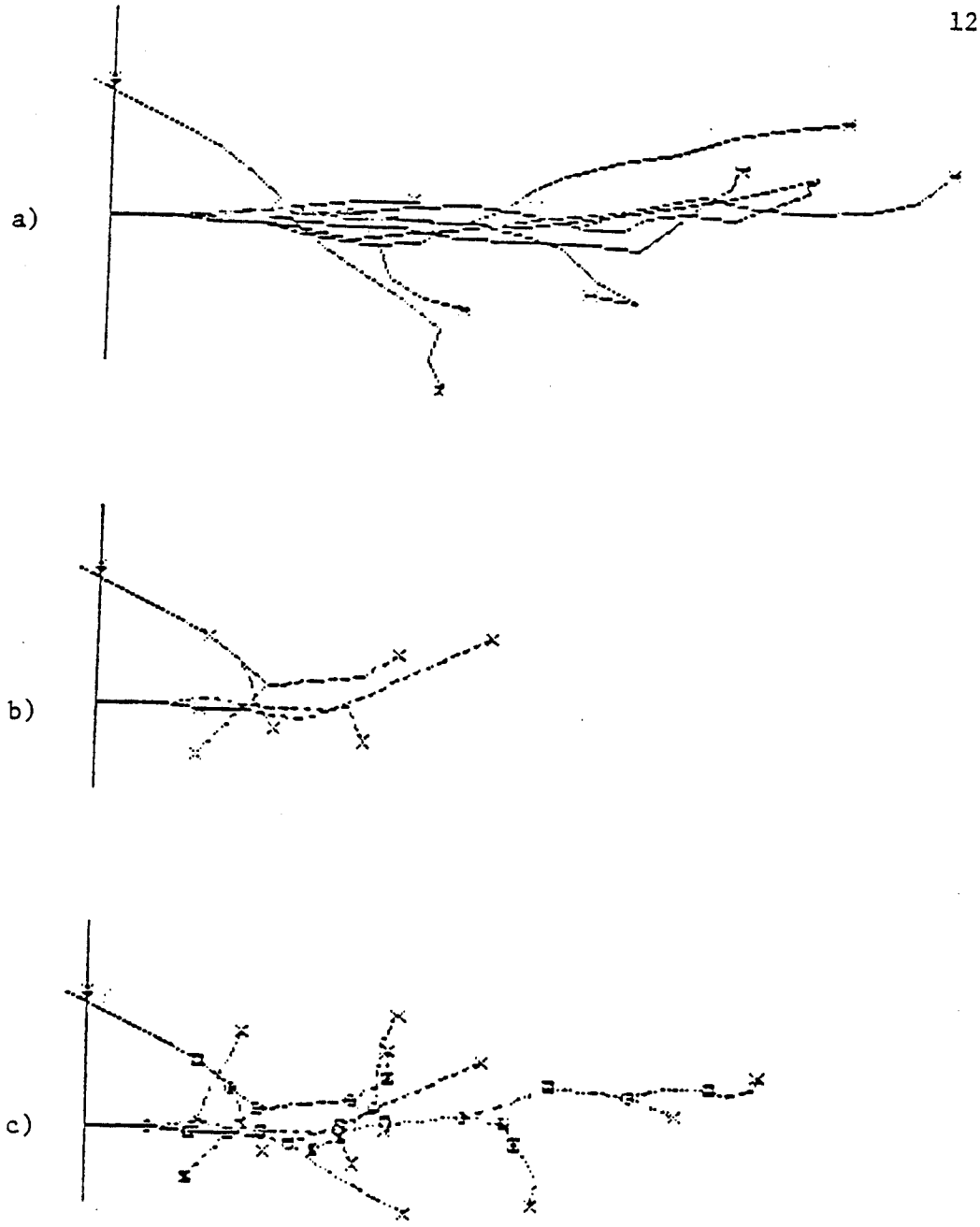

Fig. 5-6. Display output from HERAD: a) 10 histories of 2 KeV Cu-Ni; b) trajectories of PKAs produced by one history of 2 KeV Cu ion in Ni; c) the complete cascade developed by one history of 2 KeV Cu ion in Ni.

There are other programs which have been developed to work with HERAD. These are:

POTSET. Which has been mentioned early, computes the CDF of the used potential. POTSET uses the cautious adaptive Romberg extrapolation method to integrate the differential scattering cross section. An interval of 0.001 in units of the variable $t^{1/2}$ is used to produce total of 10,000 values each of which is corresponding to the value of the integral $\int_{.001}^{t^{1/2}} d\sigma$ where $t^{1/2}$ is taken as a multiple of the interval .001 from .001 up to 10.

The output of POTSET (the CDF) is a binary file which can be read by HERAD from the ENTRY point RROPN10. Alternatively, POTSET can be used as a subroutine in HERAD where it can be called from the same ENTRY point.

REG. This program performs a simple linear regression analysis. If one for example runs HERAD with all the parameters having their default values, then for each parameter involved in this analysis an additional run of HERAD is required with this parameter increased by an increment. The outputs of HERAD are then fed to REG together with experimental results, for example, of the projected range and/or the straggling, etc. From these data REG constructs the so called information, or the Fisher matrix, and solves for the new values of the chosen parameters which are input again to HERAD. For more information see Refs. 20 and 21.

RUNPLT. This is the major plotting routine, it reads the output of HERAD and other programs (e.g. MARLOWE, TRIM, BRICE, E-DEP-1,

see next chapter for the discussion and the references of these codes). If experimental data are readily available RUNPLT reads them too and makes the required graphs.

DIGITIZE. This program was first written in BASIC computer language, using the HP-9872 plotter with HP-System 45 computer. The function of this program is to digitize the experimental data which are available only through graphs. Another version of DIGITIZE was written in FORTRAN to be used on CRAY-1 computer with the Tektronix 4662 plotter and the Tektronix 4006-1 graphic terminal. DIGITIZE produces an output file which is readable by RUNPLT. Figure 5-7 shows the communication between the above mentioned codes.

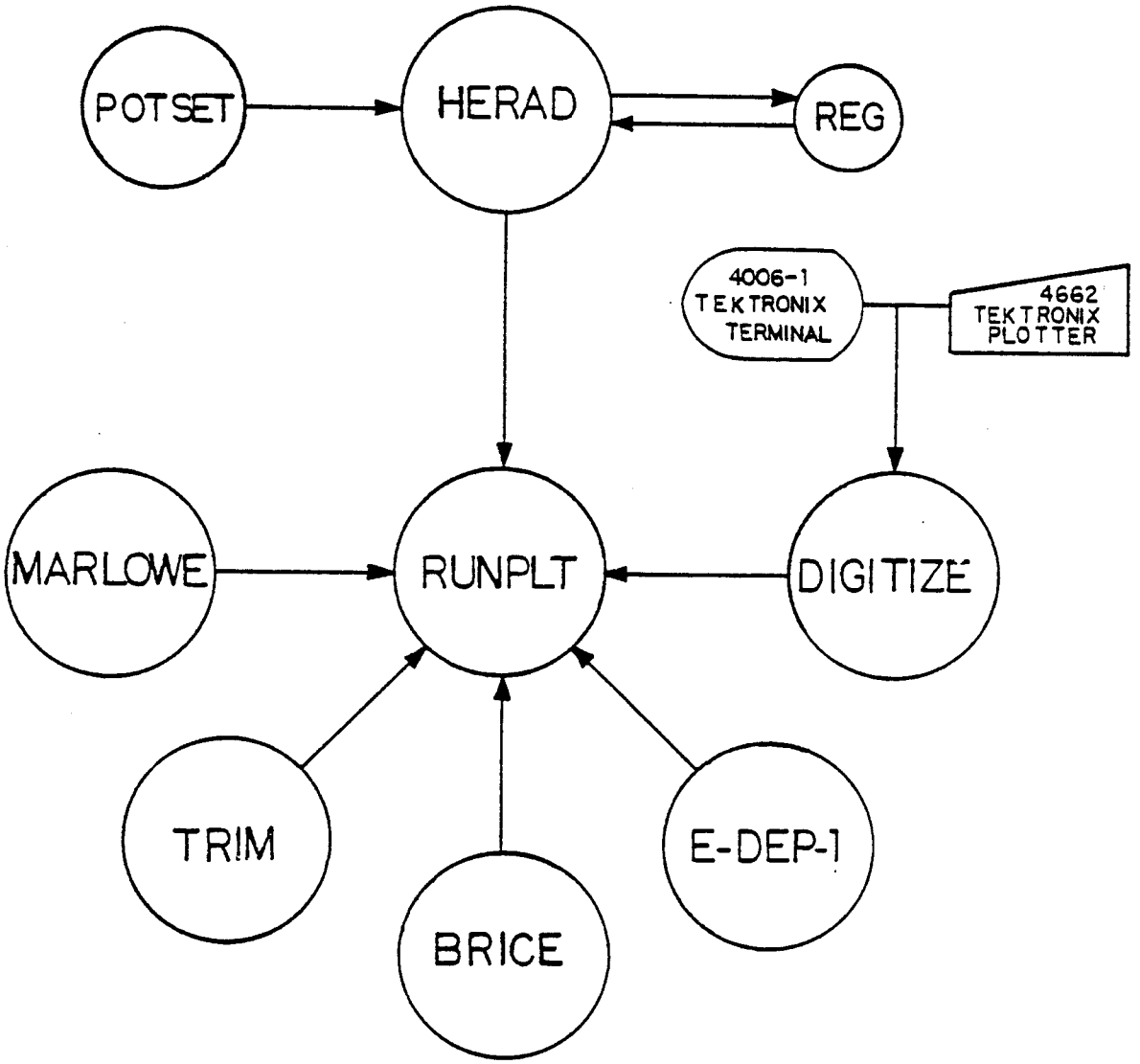

Fig. 5-7. Schematic diagram showing the communications between HERAD and other codes.

References for Chapter V

1. J. Lindhard, V. Nielsen, and M. Scharff, Mat. Fys. Meddn. Dan. Vid. Selsk. 36, No. 10 (1968).

2. K. B. Winterbon, Proc. Int. Conf. on Atomic Collision in Solids IV, held in Gausdal, Norway, 1971. Gordon and Breach, London, 429 (1972).

3. K. B. Winterbon, P. Sigmund, and J. B. Sanders, Mat. Fys. Meddn. Dan. Vid. Selsk. 37, No. 14 (1970).

4. P. Sigmund, Phys. Rev. 184, 383 (1969).

5. N. Bohr, Mat. Fys. Meddn. Dan. Vid. Selsk. 18, No. 8 (1948).

6. J. P. Biersack and L. G. Haggmark, Nucl. Inst. Meth. 174, 257 (1980).

7. J. Lindhad and M. Scharff, Phys. Rev. 124, 128 (1961).

8. O. B. Firsov, Zb. Eksp. Teor. Fiz. 36, 1517 (1959), [Soviet Phys. JETP 36, 1076 (1959)].

9. D. K. Brice, Phys. Rev. 6, 1971 (1972).

10. J. Lindhard, V. Nielson, M. Scharff, and P. V. Thomsen, Mat. Fys. Meddn. Dan. Vid. Selsk. 33, No. 10 (1963).

11. M. T. Robinson, Proc. Int. Conf. on Radiation-Induced Voids in Metals, Albany, NY (1971).

12. G. H. Kinchen and R. S. Pease, Rep. Prog. Phys. 18, 1 (1955).

13. D. McLean, Grain Boundaries in Metals, Oxford University Press, London, 110 (1957).

14. E. E. Underwood, Quantitative Stereology, Addison-Wesley Pub. Comp., 25-29 (1970).

15. R. L. Fullman, Trans AIME 197, 447 (1953).

16. J. W. Cahn and R. L. Fullman, Trans. AIME 206, 610 (1956).

17. G. R. Odette, D. M. Schwartz, and A. J. Ardell, Rad. Eff. 22, 217 (1974).

18. D. E. Knuth, The Art of Computer Programming, Vol. II, Addison-Wesley, Reading, Mass., 1969.

19. J. H. Ahrens and U. Dieter, Comm. ACM 15 873 (1972).

20. C. W. Maynard, in Symp. on "Neutron Cross Section from 10 to 40 MeV, " held at Brookhaven Nat. Lab., NY, 1977, BNL-NCS-50681, 375 (1977).

21. V. V. Federov, "Theory of Optimal Experiments," Academic Press, NY, 33 (1972).

22. H. Attaya and G. L. Kulcinski, Univ. of Wisconsin Fusion Design Memo, UWFDM series.

CHAPTER VI

RESULTS AND DISCUSSION

VI-1. Introduction

The final object of this work is to verify the damage-depth relation accurately as much as possible, and to study the effect of inhomogeneities introduced in the material during the course of irradiation. These inhomogeneities could result from the formation of cavities or change in the size distribution precipitates. Differences between the observed damage distribution (i.e. swelling) versus the depth and the calculated damage distribution have been observed for both light ion [1] and heavy ion [2] irradiation.

The work of Whitley [2] shows that the peak of swelling and the end of the range in nickel targets implanted with different ions (Ni, Cu, Al, C) at different energies is deeper than that of the calculated damage distribution by a factor of 15-20%. Fenske et al. [1] observed, for nickel implanted with 500 keV He ions, that the peak swelling occurs at depths ~ 8-15% deeper than the peak in the calculated projected range profile and 15-25% deeper than the peak in the calculated damage profile. A larger difference, up to 50-90% has been also observed by Fenske et al. [3] for nickel implanted with 25 keV He ions.

Differences between the calculated and observed damage profile have also been observed in void free material [4]. Here the damage is measured in terms of the loop density, and it was also found to be deeper than that calculated by the computer code E-DEP-1 [5] which

does not take into account the effect of recoils in the damage energy distribution. Different electronic energy loss models were used in that work to match the calculated damage with observed damage.

As a first step to study the damage depth relation, one needs to reconsider the range of ions in the material, which is the prime factor in any damage calculations, and to test the models against experimental data that is available. With respect to the experimental data, one finds a wide spread of uncorrelated data especially for low energy and high energy heavy ions. Helium and hydrogen have enjoyed much more systematic investigations, especially in the high energy region.

There is almost no information about the ranges of heavy ions in Ni, especially in the energy range of interest (10-15 MeV). Furthermore, even for the existing data there is no satisfactory agreement between theoretical ranges and the observed ranges. A brief review of the situation is given below.

VI-2. Experimental Results

Because of the need for the experimental information on the range of heavy ions in nickel we have irradiated different, high purity nickel samples with copper and carbon ions in the U.W. tandem Van De Graaff accellerator. The Cu ions energies were 15, 13.97, 12.96, and 12.13 MeV. The C ions energies were 16, 12.51, 10, and 5 MeV. These energies were selected to be as close as possible to the energies used by Whitley in his work. The samples were analyzed by the Materials Research Laboratory of the University of Illinois. The

Secondary Ions Mass Spectroscopy (SIMS) method was used to determine the range of the ions in the nickel targets. The experiment was repeated again with higher doses on a nickel single crystals. In either case we were not able to obtain any consistent results. The problem was mainly the instrument drift over the long period of time it takes to sputter to the depth of the implanted ions (several microns), and also the difficulties of measuring and calibrating the depth of the crater. Because of these factors, the depth calibration with the sputtering time was not possible. Figure 6-1 shows a typical example of the obtained ion count versus the sputtering time for the 13.97 Cu Ions in nickel. We had hoped to get accurate results to compare it with our Monte Carlo results, and with the other computer codes results, but we were unsuccessful in this regard.

VI-3. Ion Range

In this section we present the results of the ranges of different ions in different targets as predicted by the code HERAD. The cases considered here are Cu-Ni, C-Ni and some cases which have been studied previously either experimentally or by other computational methods. With respect to the other computational methods, we have converted most of the range-damage computer codes to run on three different computer systems, the UNIVAC 1110, CDC 7600, and CRAY-1 systems. The codes that were considered are E-DEP-1 [5], BRICE [6], TRIM [7], and MARLOWE [8]. This task required some modifications and additions, in which we tried to unify as much as possible the input and the output data format so that our comparison would be easier

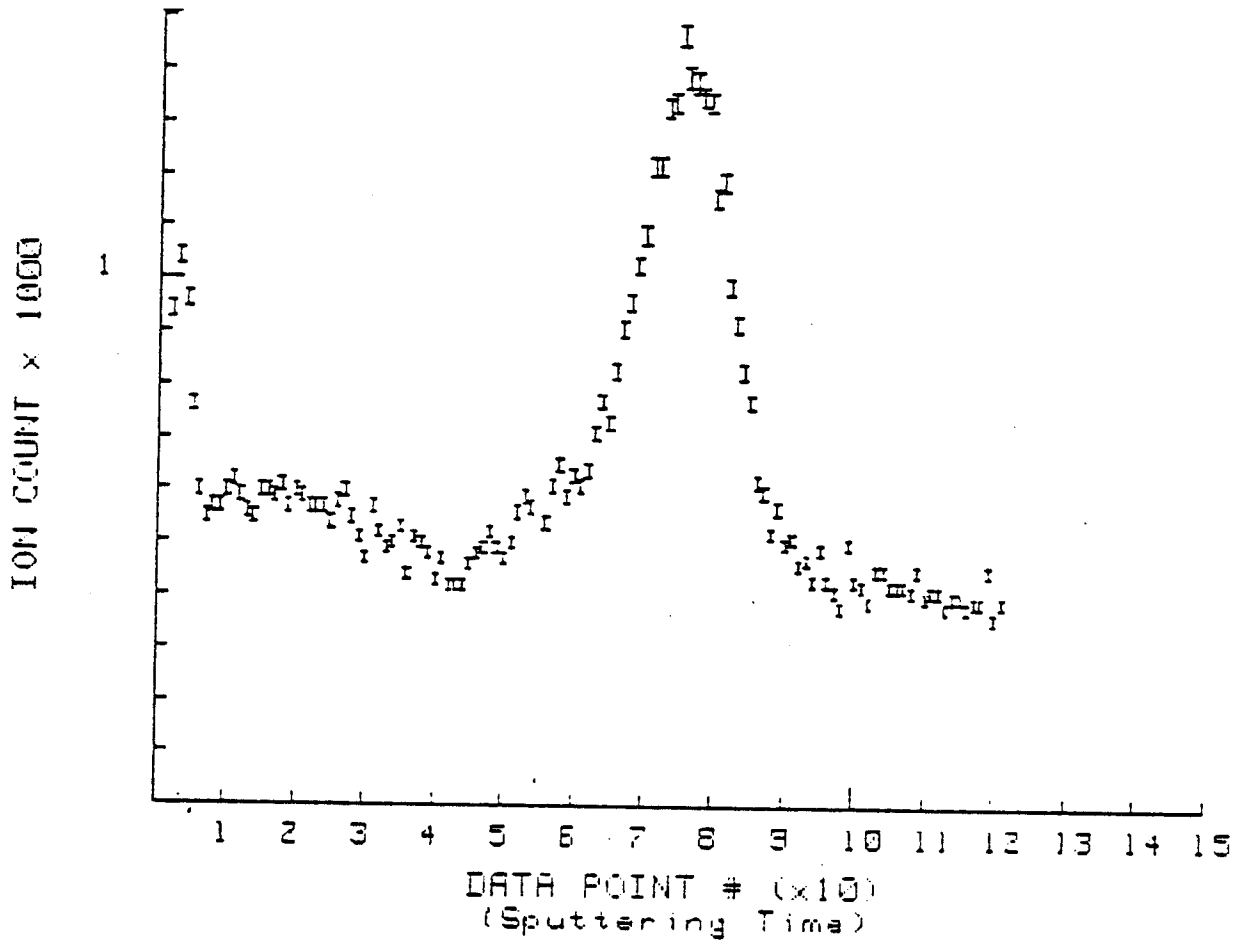

Fig. 6-1. Results obtained by SIMS method for 13.97 MeV Cu-Ni.

and would not involve any effect which may arise because of the different way each code interprets the input data.*

VI-3-1. Cu in Ni

Figures 6-2, 6-3, 6-4, and Table 6-1 show the results of the HERAD calculations compared to those from E-DEP-1, BRICE, TRIM and MARLOWE. The potential used in HERAD and E-DEP-1 as well as BRICE is the Thomas-Fermi potential. The Moliere potential is used in MARLOWE and TRIM and the electronic energy loss used in the first three codes are the same and is that of LSS. TRIM uses LSS for reduced energies (ε) less than 10. Above $\varepsilon = 10$. TRIM uses the formula:

$$\frac{1}{S_e} = \frac{1}{S_{e_{LSS}}} + \frac{1}{S_{e_{B.B}}}$$

where $S_{e_{LSS}}$ is LSS electronic stopping and $S_{e_{B.B}}$ is the Bethe-Bloch stopping. For MARLOWE the electronic stopping is more complicated and is divided into two parts; non-local, which is independent of the impact parameter and could be taken either that of LSS or of Firsov, and a local part which depends on the impact parameter in each collision and which is given by Firsov's formula. The fraction assigned for each part is optional and, as was recommended by Robinson [9], we chose the local and the non-local electronic stoppings with equal weight, i.e. 50% of the total electronic stopping is calculated as local and the other 50% as non-local. Figure 6-5 shows the

* As an example, each code uses different parameters to calculate the target density, e.g. BRICE uses the lattice constant, TRIM uses the gram density, and E-DEP-1 uses the atomic density.

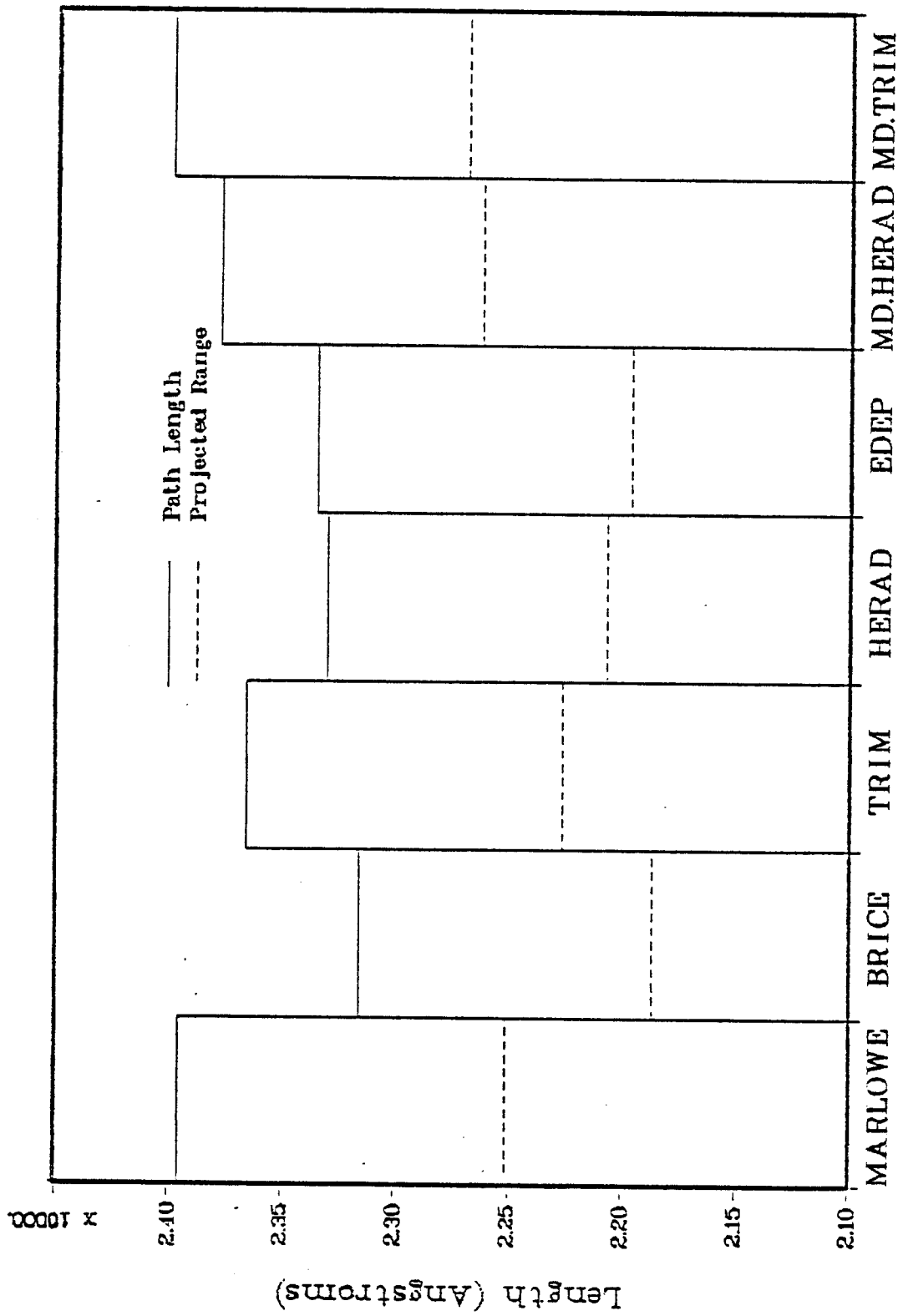

Fig. 6-2. The path length and projected range as obtained using different computer codes for 15 MeV Cu-Ni; MD means the median.

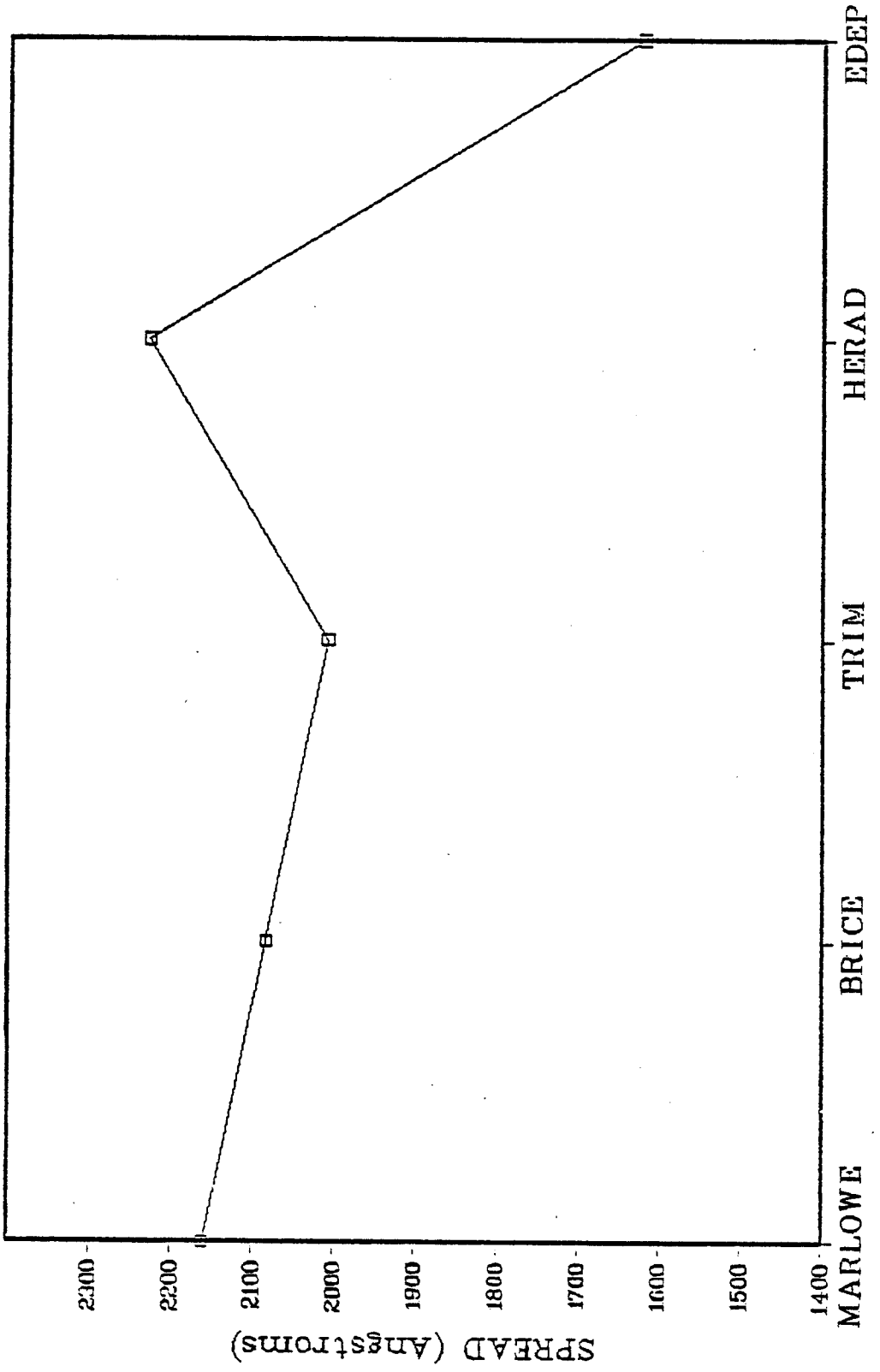

Fig. 6-3. The straggling in the projected range for 15 MeV Cu-Ni as obtained using different computer codes.

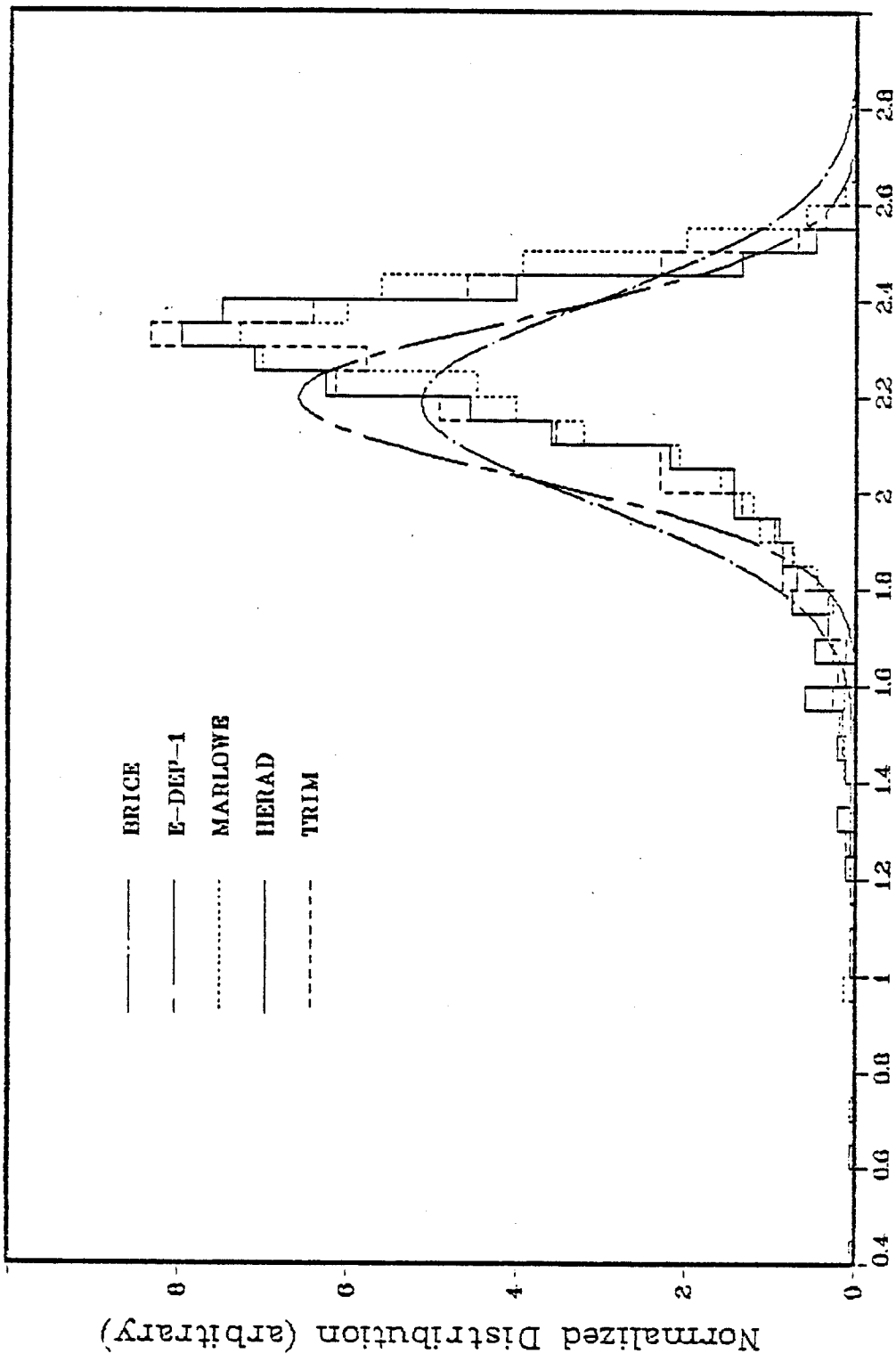

Fig. 6-4. The depth distribution for 15 MeV Cu-Ni, as predicted by the different computer codes.

TABLE 6-1

Results of Range Calculation from Different Computer Codes for 15 MeV Cu-Ni (Units in Angstroms)

Ranges	Code	Mean	Median	Std. Dev.	Skewness	Kurtosis	Error	# Hist.
1) Depth	BRICE	21868.		2082.				
	E-DEP-1	21960.		1621.				
	MARLOWE	22511.		2160.	-2.01	7.44	76.	800
	TRIM	22265.	22687.	2006.	-1.70	5.00	63.	1000
	HERAD	22069.	22617.	2226.	-2.30	9.16	70.	1000
2) Path	BRICE	23158.						
	E-DEP-1	23341.		1622.				
	MARLOWE	23953.		1859.	-2.36	10.96	66.	800
	TRIM	23655.	23989.	1673.	-2.03	7.24	53.	1000
	HERAD	23296.	23774.	1895.	-2.26	8.36	60.	1000
3) Perpendicular	BRICE			3925.				
	MARLOWE	3664.		1989.	0.70	0.29	70.	800
	HERAD	3420.	3205.	1852.	0.75	0.82	59.	1000
4) Vector Range	MARLOWE	22908.		1999.	-2.07	8.26	71.	800
	HERAD	22426.	22909.	2055.	-215	7.37	65.	1000

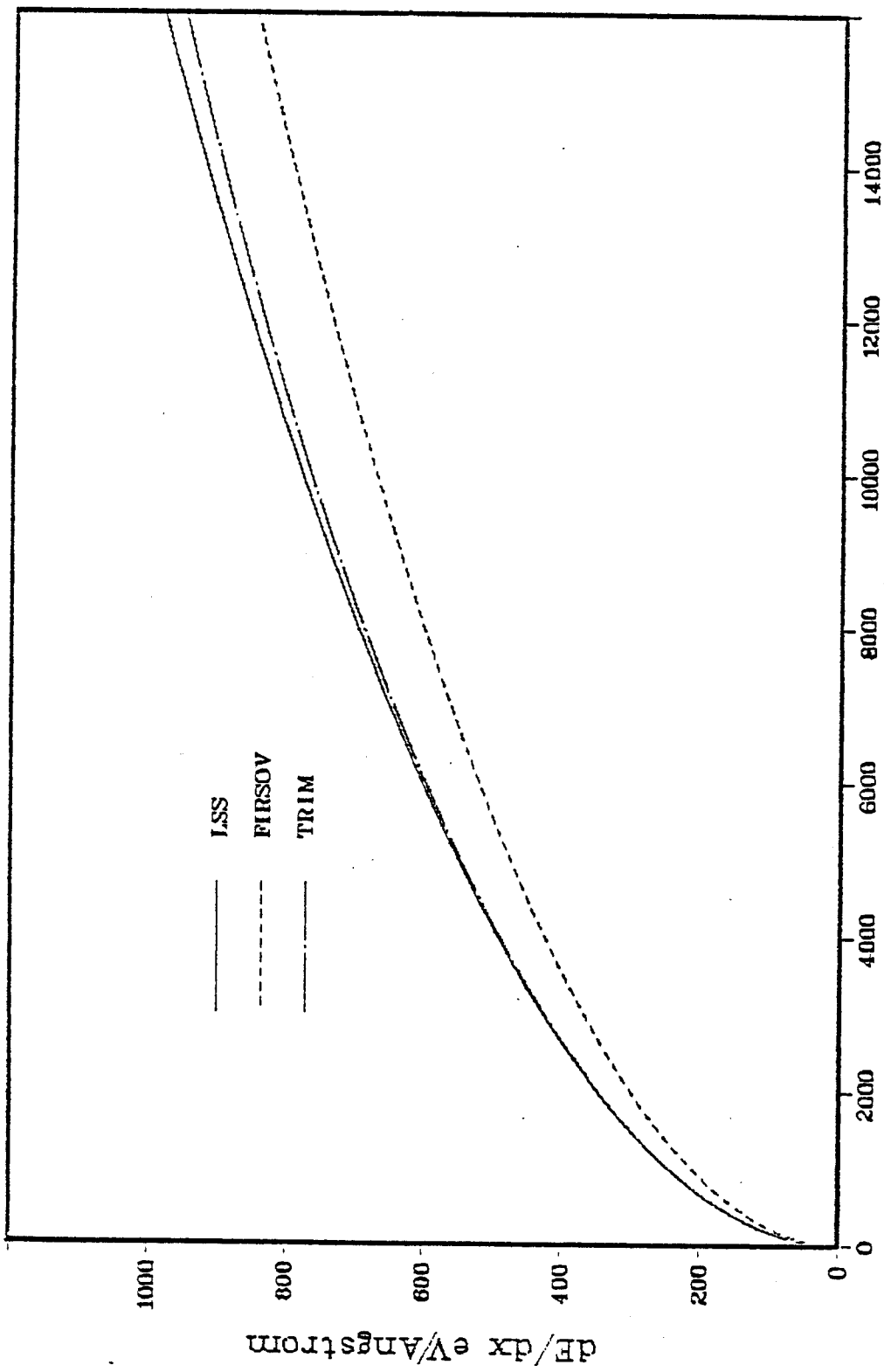

Fig. 6-5. The electronic energy loss for Cu ions in Ni.

electronic energy loss as a function of the energy of the copper ion and as calculated using LSS and Firsov, and the model used in TRIM. It is seen that in this case Firsov gives the value of S_e lower than that of LSS by a factor of about 10-15%. TRIM values of Se are slightly less than LSS values. There is a good agreement of the results of HERAD with other codes. Almost all the codes agree within 3.1% with respect to path length where the highest values are given by MARLOWE and the lowest are given by BRICE. HERAD gives the highest value of the straggling in the projected range, while EDEP gives the lowest value. The shape of the projected range distributions is also in good agreement among the Monte-Carlo codes. HERAD agrees very well with MARLOWE in the value of the perpendicular range. The high value of straggling in this parameter given by the Brice code is due to the fact that the perpendicular range is considered, in Brice's theory, as a vector quantity whose mean value is zero, while in MARLOWE or HERAD the perpendicular range is a scalar quantity for which an average value exists. However, it can be proven from the elementary statistical analysis that the variance of the perpendicular range as a vector , V_v, is related by the variance of the scalar perpendicular range V_s as

$$V_v = V_s + R_m^2$$

where R_m is the mean of the scalar perpendicular range. Using this equation we get a value of 4169 Å for MARLOWE and 3910 Å for HERAD which are in a good agreement with Brice (which is 3925 Å).

The slight differences between the codes' results could be related to the different potential and much more to some intrinsic features of each code. We used also Moliere potential in this case but we couldn't get noticable differences from the results obtained by Thomas-Fermi potential. For high energy there is almost no difference between the two potentials. Figure 6-6 shows different potentials, and it is hard to see any difference between Thomas-Fermi and Moliere potentials up to six units of interatomic separation. The use of the magic formula of Lindhard in this energy region is quite satisfactory. Robinson [10] compared this formula with the exact Thomas-Fermi potential and found an excellent agreement between them. His results are shown in Fig. 6-7. There exists other differences among these codes which are related to the choice of the screening length, and the maximum impact parameter and the minimum angle of scattering. The effect of these and other parameters on the results of HERAD will be discussed later.

The computer time, in minutes on the CRAY-1 computer, for each code to perform the calculations summarized in Table 6-1 are as follows:

a) MARLOWE 82.5 (800 histories)

b) TRIM 2.1 (1000 histories)

c) HERAD .8

d) BRICE .4

e) EDEP .1.

The computer time of HERAD is different from that given in Ref. 11

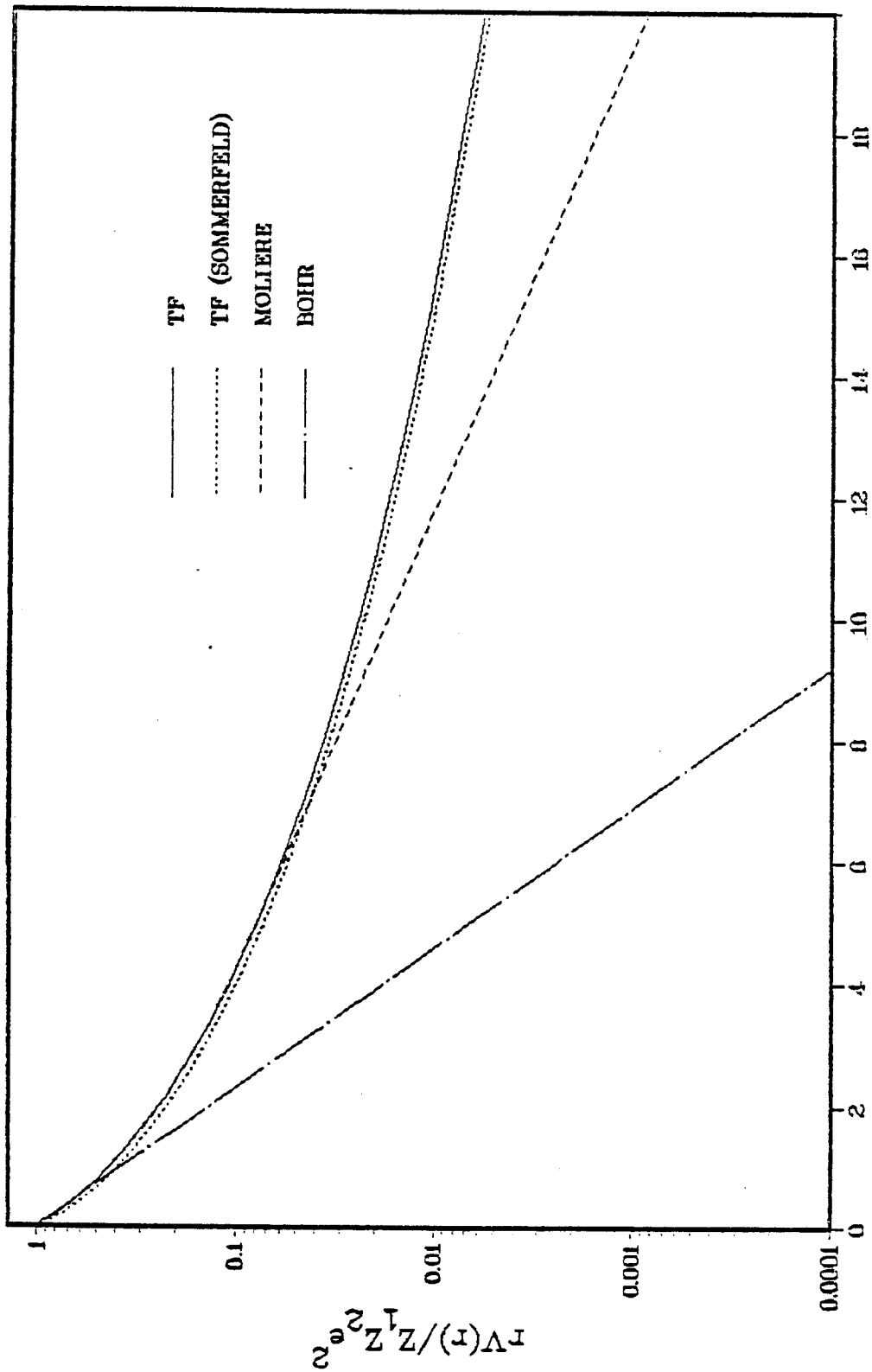

Fig. 6-6. The screening function of different potentials as a function of the interatomic separation.

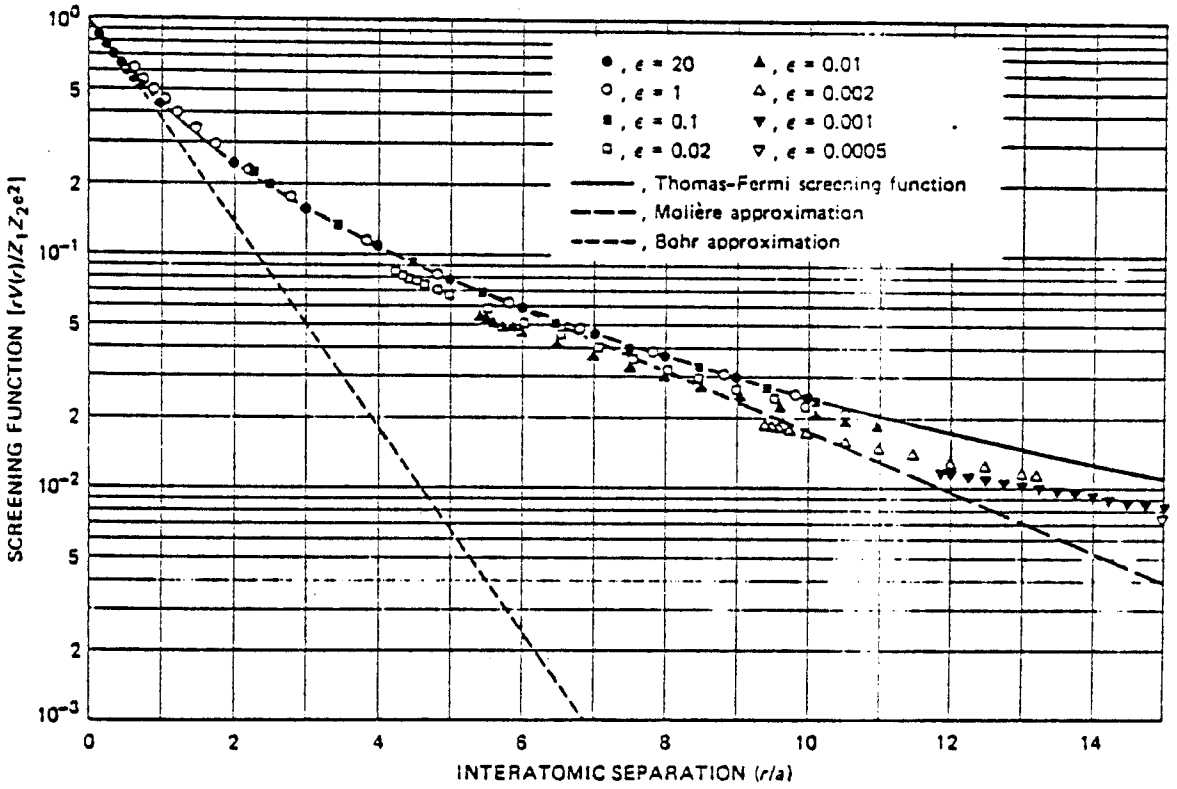

Fig. 6-7. The screening function deduced from Lindhard's differential scattering cross section at various energies as compared with the Thomas-Fermi, Moliére, and Bohr screening functions (after Robinson [10]).

for an old version of HERAD, because of the inclusion of many recent modifications and extensions.

The conclusion of this case is that HERAD is proven to be in very good agreement with other codes and with a very considerable reduction in the computation cost with respect to MARLOWE and TRIM. Also it provides more statistical information than the analytical codes and TRIM, with much more flexibility is the choice of the potential or the electronic energy loss law.

Tables 6-2 - 6-4 show the results obtained for Cu-Ni with different energies, and the conclusions are very much the same as in the 15 MeV case.

VI-3-2. Carbon in Nickel

Table 6-5 and Figs. 6-8 - 6-10 show the comparison for the obtained results for 5 MeV C ions in nickel. The 5 MeV energy was chosen because it is the minimum energy one can obtain for carbon in the U.W. tandem Van De Graaff accellerator, which was used in irradiating one of the nickel samples mentioned in the preceding section. This case is interesting because it shows the effect of the various electronic energy models on the range of the carbon. Figure 6-11 shows the electronic energy loss for C-Ni as a function of the energy of the carbon, for different electronic energy loss laws, and Fig. 6-12 shows them as a function of the square root of the energy of the carbon ion. The arrows in both figures are pointed to the energy estimated by Lindhard to be the upper limit for the LSS formula. Note that in this case, Firsov's formula gives higher stopping rates

TABLE 6-2

Results of Range Calculation from Different Computer Codes for 12.96 MeV Cu-Ni (Units in Angstroms)

Ranges	Code	Mean	Median	Std. Dev.	Skewness	Kurtosis	Error	# Hist.
1) Depth	BRICE	19739.		2023.				
	E-DEP-1	19836.		1575.				
	MARLOWE	20490.		2129.	-2.24	9.40	75.	800
	TRIM	20136.	20531.	2037.	-1.77	5.30	64.	1000
	HERAD	19965.	20487.	2303.	-2.49	10.44	73.	1000
2) Path	BRICE	21003.						
	E-DEP-1	21180.		1589.				
	MARLOWE	21866.		1820.	-2.62	12.67	64.	800
	TRIM	21496.	21860.	1667.	-1.90	6.23	53.	1000
	HERAD	21142.	21587.	2053.	-2.81	13.38	65.	1000
3) Perpendicular	BRICE			3736.				
	MARLOWE	3391.		1832.	0.72	0.22	65.	800
	HERAD	3208.	3028.	1713.	0.60	0.11	54.	1000
4) Vector Range	MARLOWE	20866.		1954.	-2.23	9.07	69.	800
	HERAD	20308.	20796.	2170.	-2.51	10.67	69.	1000

TABLE 6-3

Results of Range Calculation from Different Computer Codes for 12.13 MeV Cu-Ni (Units in Angstroms)

Ranges	Code	Mean	Median	Std. Dev.	Skewness	Kurtosis	Error	# Hist.
1) Depth	BRICE	18832.		1995.				
	E-DEP-1	18929.		1553.				
	MARLOWE	20490.		2129.	-2.24	9.40	75.	800
	TRIM	19130.	19482.	1985.	-1.76	5.92	63.	1000
	HERAD	19208.	19616.	1885.	-1.92	7.42	60.	1000
2) Path	BRICE	20081.						
	E-DEP-1	20256.		1574.				
	MARLOWE	21866.		1820.	-2.62	12.67	64.	800
	TRIM	20472.	20805.	1646.	-1.91	7.01	52.	1000
	HERAD	20351.	20704.	1632.	-2.01	8.43	52.	1000
3) Perpendicular	BRICE			3650.				
	MARLOWE	3391.		1832.	0.72	0.22	65.	800
	HERAD	3154.	3023.	1677.	0.62	0.26	53.	1000
4) Vector Range	MARLOWE	20866.		1954.	-2.23	9.07	69.	800
	HERAD	19549.	19933.	1760.	-1.84	6.82	56.	1000

TABLE 6-4

Results of Range Calculation from Different Computer Codes for 13.97 MeV Cu-Ni (Units in Angstroms)

Ranges	Code	Mean	Median	Std. Dev.	Skewness	Kurtosis	Error	# Hist.
1) Depth	BRICE	20810.		2054.				
	E-DEP-1	20905.		1599.				
	MARLOWE	21505.		2109.	-1.83	5.67	75.	800
	TRIM	21282.	21699.	2042.	-2.14	8.75	65.	1000
	HERAD	21210.	21683.	1973.	-1.97	6.90	62.	1000
2) Path	BRICE	22088.						
	E-DEP-1	22268.		1606.				
	MARLOWE	22910.		1783.	-1.91	6.32	61.	800
	TRIM	22636.	22942.	1674.	-2.33	10.75	53.	1000
	HERAD	22379.	22761.	1684.	-2.21	10.09	53.	1000
3) Perpendicular	BRICE			3834.				
	MARLOWE	3466.		1858.	0.71	0.52	66.	800
	HERAD	3275.	3120.	1736.	0.60	0.18	55.	1000
4) Vector Range	MARLOWE	21877.		1942.	-1.74	4.96	69.	800
	HERAD	21544.	21957.	1823.	-1.99	7.57	58.	1000

TABLE 6-5

Results of Range Calculation from Different Computer Codes for 5 MeV C-Ni (Units in Angstroms)

Ranges	Code	Mean	Median	Std. Dev.	Skewness	Kurtosis	Error	# Hist.
1) Depth	BRICE	20957.		1568.				
	E-DEP-1	22638.		1265.				
	MARLOWE	23832.		1535.	-1.81	5.92	54.	800
	TRIM	25044.	25365.	1429.	-1.81	6.10	45.	1000
	HERAD	20825.	21117.	1485.	-1.76	5.36	47.	1000
2) Path	BRICE	23012.						
	E-DEP-1	24855.		501.				
	MARLOWE	26266.		541.	-1.53	4.79	19.	800
	TRIM	27385.	27466.	499.	-1.59	4.88	16.	1000
	HERAD	23174.	23247.	578.	-2.37	14.98	18.	1000
3) Perpendicular	BRICE			3457.				
	MARLOWE	3661.		1975.	0.85	1.35	70.	800
	HERAD	3714.	3446.	1993.	0.80	0.70	63.	1000
4) Vector Range	MARLOWE	24206.		1309.	-1.77	6.09	46.	800
	HERAD	21262.	21533.	1266.	-1.69	4.66	40.	1000

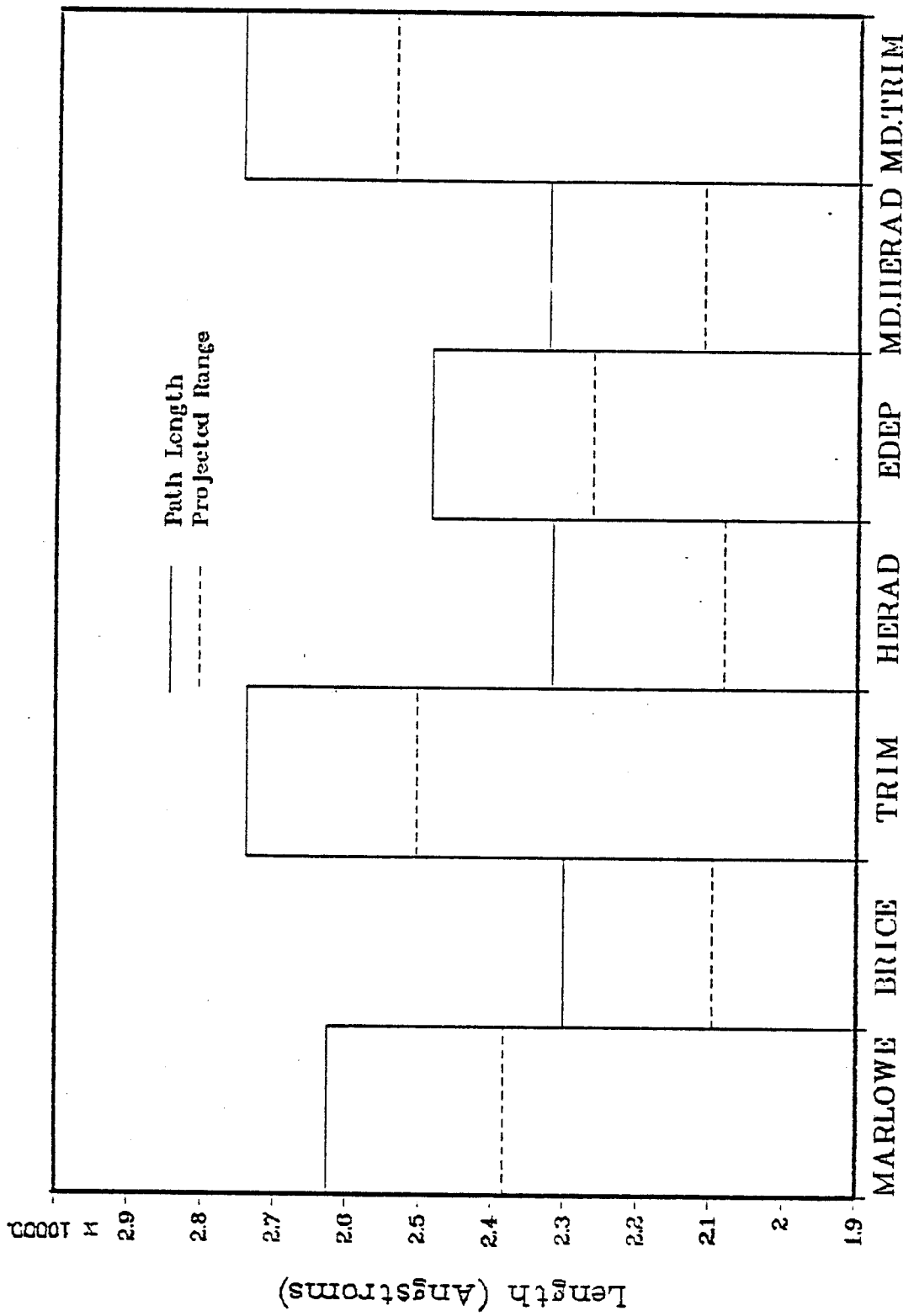

Fig. 6-8. The path length and projected range for 5 MeV C-Ni.

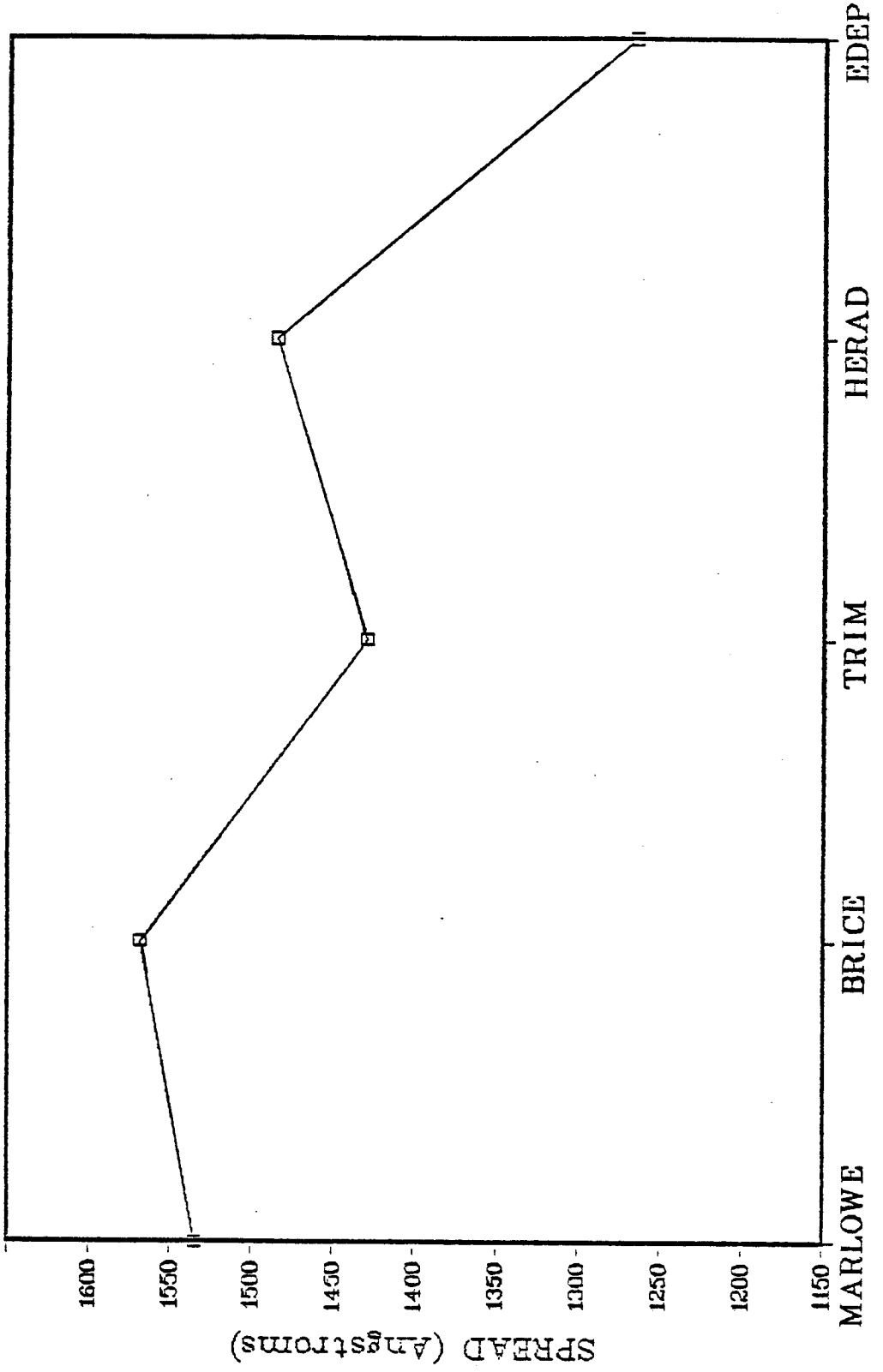

Fig. 6-9. The straggling in the projected range for 5 MeV C-Ni.

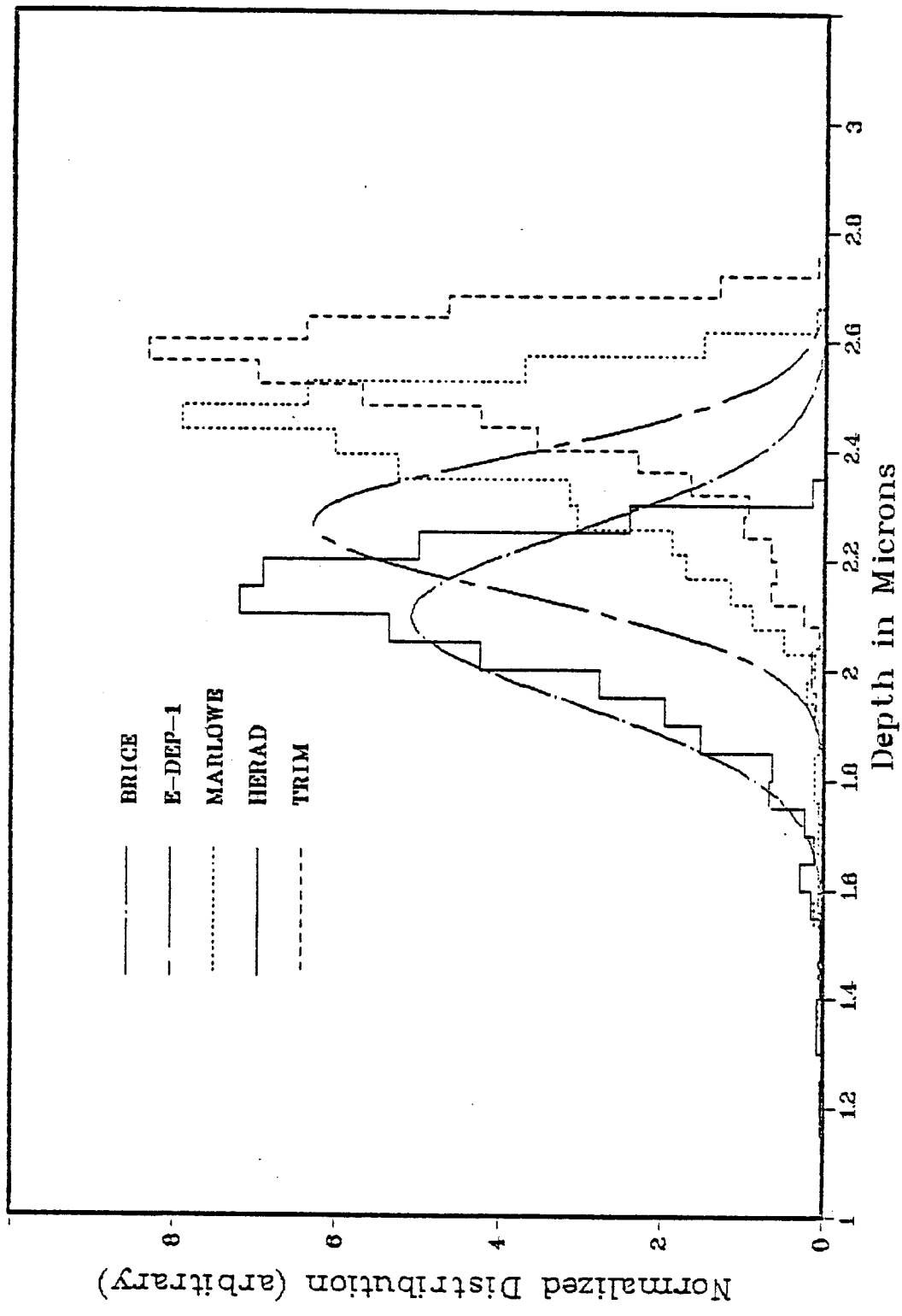

Fig. 6-10. The depth distribution for 5 MeV C ions incident on Ni target.

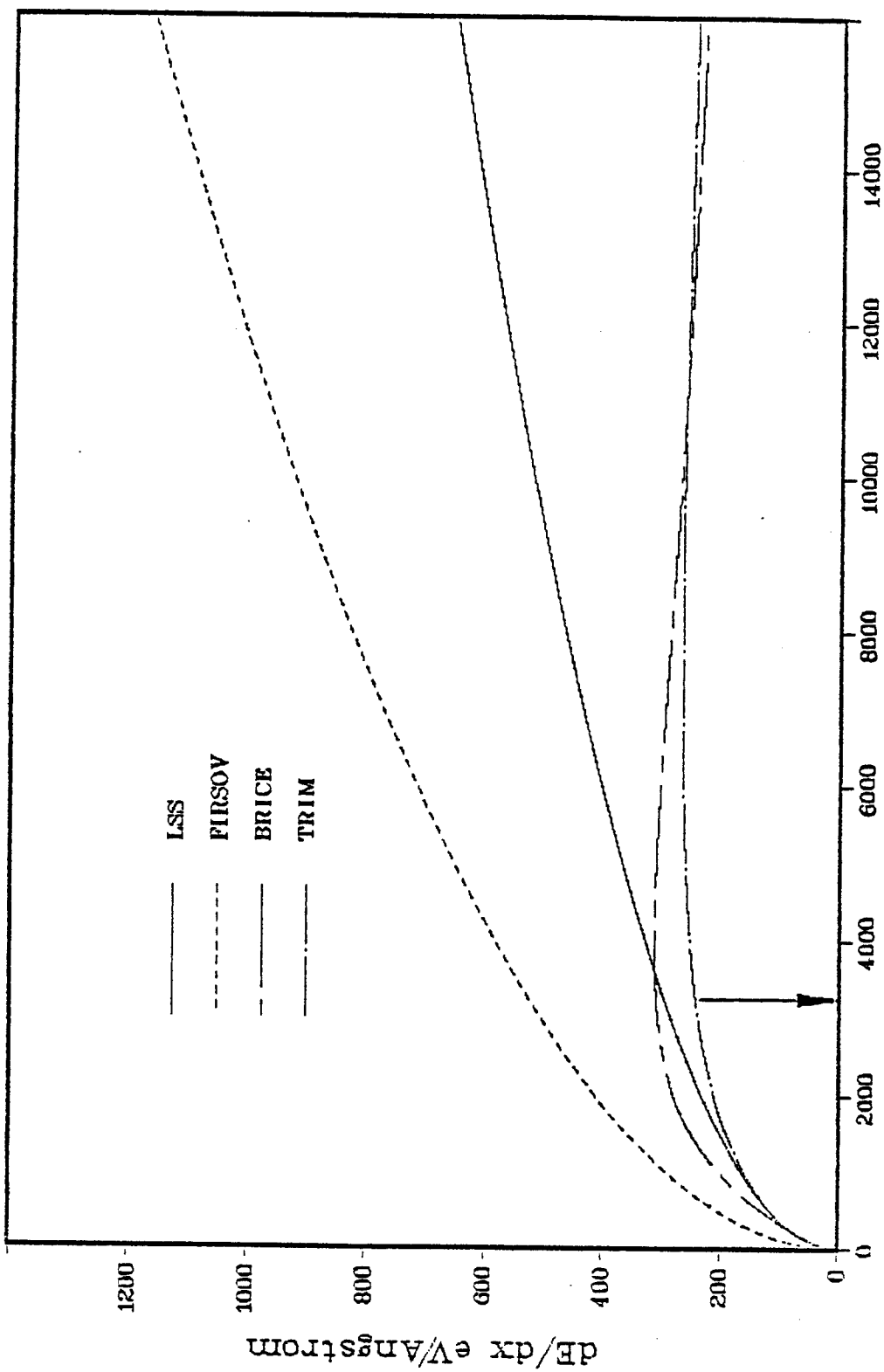

Fig. 6-11. The electronic energy loss for Carbon ions in Ni as a function of energy. The arrow points to Lindhard maximum energy.

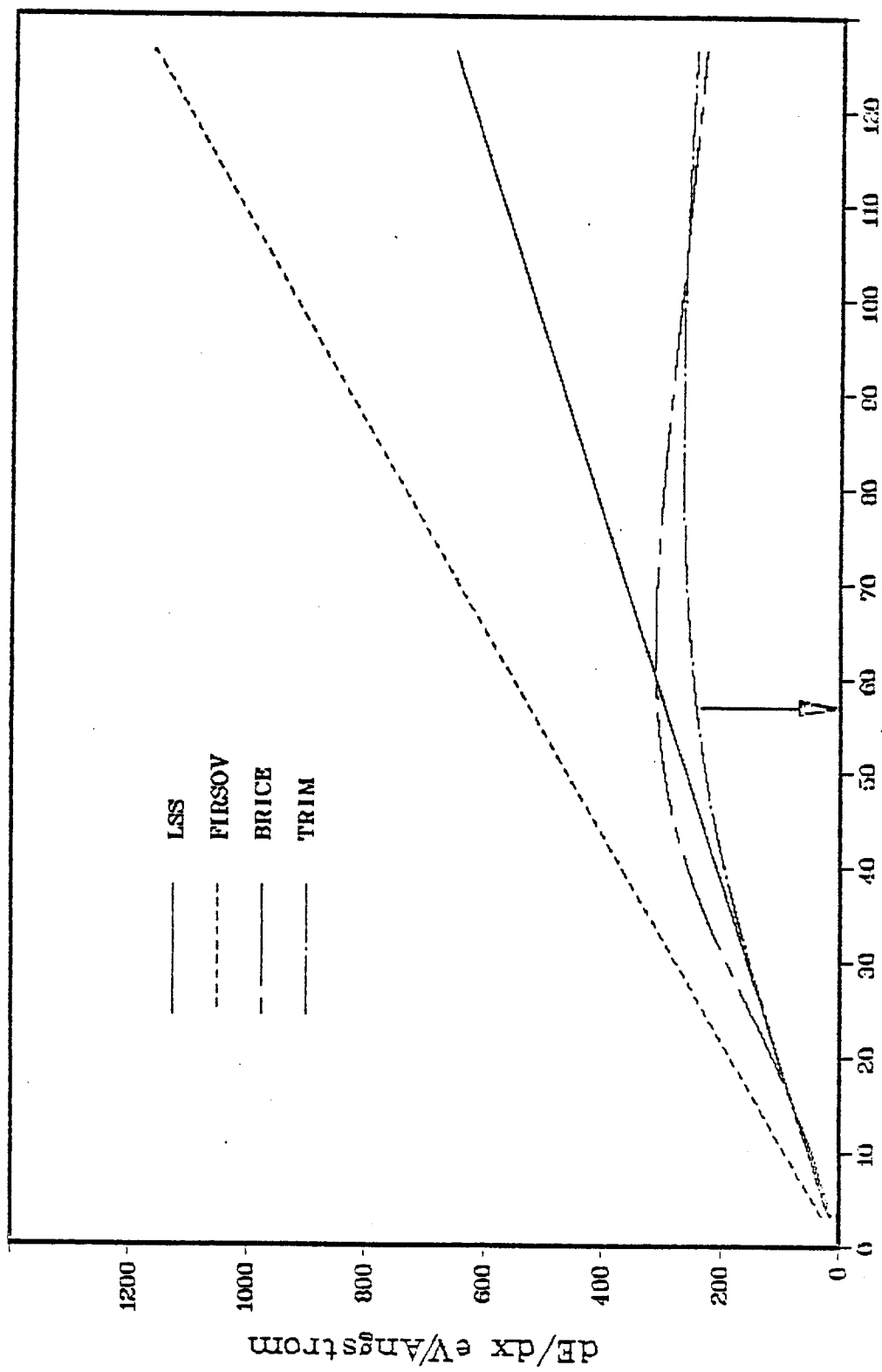

Fig. 6-12. The electronic energy loss of C in Ni as a function of the square root of the energy.

than LSS. BRICE and HERAD use the Brice three parameter formula and the other codes use the same electronic loss formulae as described in the case of Cu-Ni. One would expect from these figures that TRIM will give the longest range. The LSS electronic stopping is lower than Brice electronic stopping up to an energy of about 3.5 MeV, and for the codes which use LSS, the ranges are longer than those codes which use Brice electronic stopping. This is clear from the results in Table 6-5 and Figs. 6-8 - 6-10.

It is erroneous to use the E-DEP-1 code or any code which uses the LSS for such energy, but this case as well as the following case are presented to illustrate the effect of the electronic energy loss law on the calculated results.

Table 6-6 shows the results obtained from the various codes for the case of 10 MeV C-Ni. In this case it is clear that if the LSS stopping was used, it would give mistaken results for the ranges. HERAD results show a very good agreement with Brice results when both use the same electronic energy model, i.e. Brice formula. The difference between TRIM and the last two codes remains to be tested experimentally, i.e. which electronic energy loss model is more correct?

VI-3-3. 4 keV He^3 in Niobium

Helium and hydrogen ions emanated from fusion reaction may cause serious problems in the first wall. One of these problems is blistering, i.e. the deformation and partial exfoliation of the surface layers. No rigorous theory has yet been given to explain the

TABLE 6-6

Results of Range Calculation from Different Computer Codes for 10 MeV C-Ni (Units in Angstroms)

Ranges	Code	Mean	Median	Std. Dev.	Skewness	Kurtosis	Error	# Hist.
1) Depth	BRICE	38215.		1703.				
	E-DEP-1	33894.		1314.				
	MARLOWE	35755.		1633.	-2.10	8.49	58.	800
	TRIM	43568.	44110.	2393.	-6.71	77.97	76.	1000
	HERAD	37498.	38093.	2217.	-2.72	11.46	70.	1000
2) Path	BRICE	40063.						
	E-DEP-1	36173.		513.				
	MARLOWE	38224.		541.	-1.21	2.70	19.	800
	TRIM	46156.	46286.	685.	-4.98	48.24	22.	1000
	HERAD	40344.	40504.	730.	-2.91	17.70	23.	1000
3) Perpendicular	BRICE			4129.				
	MARLOWE	3903.		2227.	1.03	1.71	79.	800
	HERAD	5589.	5134.	3244.	1.38	3.65	103.	1000
4) Vector Range	MARLOWE	36044.		1451.	-2.05	8.74	51.	800
	HERAD	38075.	38515.	1753.	-2.52	9.79	55.	1000

mechanism by which blistering occurs. However, some of the existing theories [12,13] relate the depth of the hydrogen or helium to the thickness of the cover of the blisters. In this regard Behrisch et al. [14] measured the depth profile for 4 keV He^3 ions in niobium. Oen and Robinson [15] as well as Biersack [7b] compared the results of Behrisch with their codes, MARLOWE and TRIM, respectively. We present here the results of MARLOWE, TRIM, BRICE, and HERAD, with the experimental results. Table 6-7 together with Fig. 6-13 and Fig. 6-14 show these results. HERAD agrees very well with the other codes with respect to the statistics. Brice's code has been modified to be able to accept this low energy, and the high value of the straggling in the projected range obtained in this case is most likely to be not reliable. The depth distribution profiles show that the Monte Carlo codes predict fewer particles stopping near the surface than predicted by BRICE. HERAD, however, shows some agreement with the experimental data at the end of the range.

The agreement between HERAD, TRIM, and MARLOWE is very good with respect to the number of the backscattered He^3 ions. Out of 1000 histories used, in the three programs HERAD predicts that 288 particles would be reflected, i.e. with the reflection coefficient (number of reflected particles divided by the number of incident particles) equals to 0.288. For TRIM and MARLOWE the reflection coefficients are 0.291 and 0.283, respectively. It should be noticed that the last column in all the given tables gives the total number of the

TABLE 6-7

Results of Range Calculation from Different Computer Codes for 4 keV He^3-Nb (Units in Angstroms)

Ranges	Code	Mean	Median	Std. Dev.	Skewness	Kurtosis	Error	# Hist.
1) Depth	BRICE	156.		200.				
	MARLOWE	271.		140.	0.43	-0.43	5.	717
	TRIM	269.	342.	138.	0.40	-0.16	5.	709
	HERAD	298.	279.	155.	0.36	-0.47	6.	712
2) Path	BRICE	1048.						
	MARLOWE	1037.		64.	-0.26	-0.23	2.	717
	TRIM	1068.	1108.	66.	-0.15	-0.28	2.	709
	HERAD	1040.	1043.	69.	-0.35	0.03	3.	712
3) Perpendicular	BRICE			282.				
	MARLOWE	259.		124.	0.44	-0.17	5.	717
	HERAD	288.	271.	137.	0.39	-0.34	5.	712
4) Vector Range	MARLOWE	398.		130.	-0.03	-0.42	5.	717
	HERAD	439.	434.	147.	0.12	-0.38	6.	712

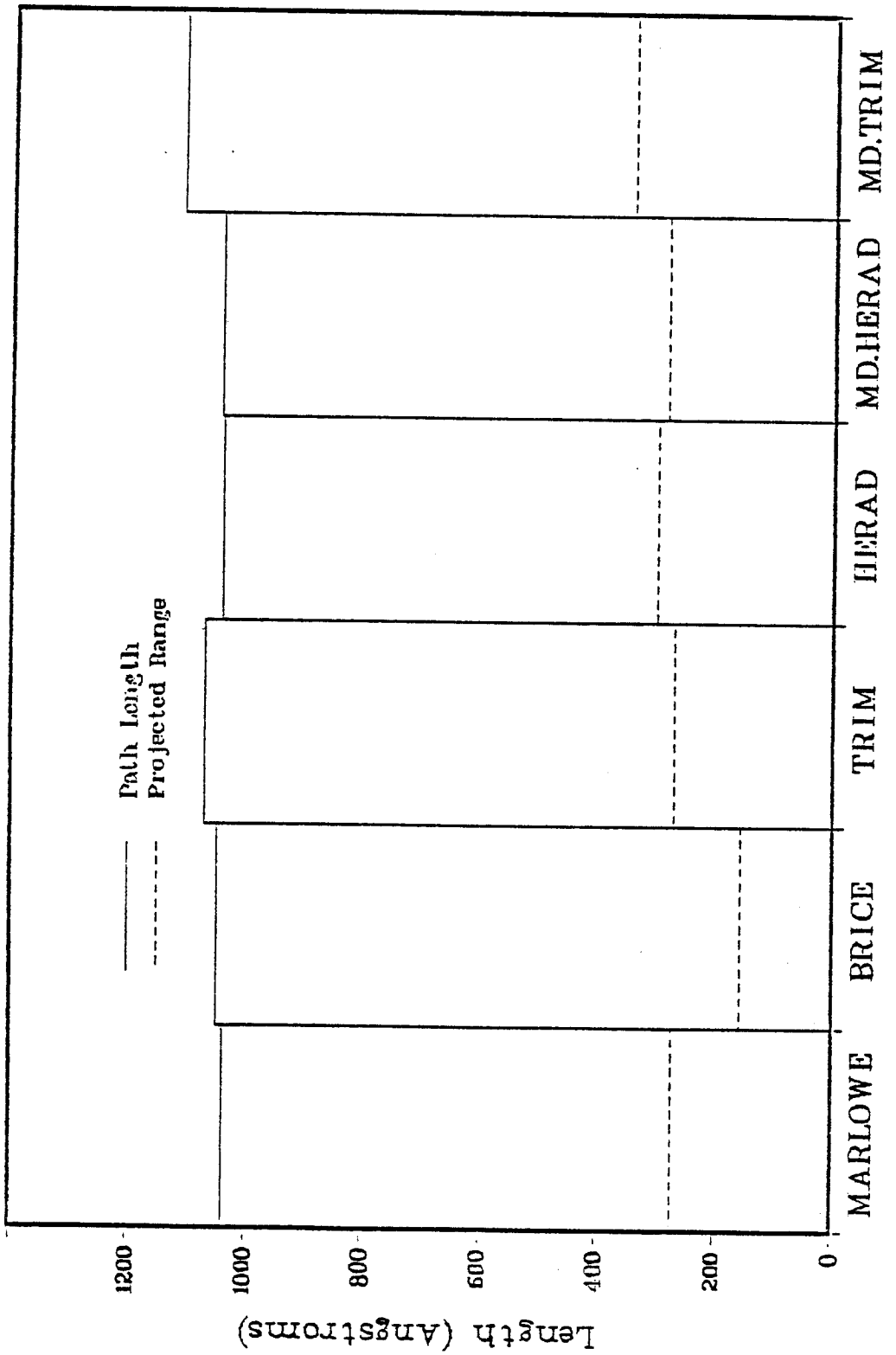

Fig. 6-13. The path length and projected range for 4 keV He^3-Nb.

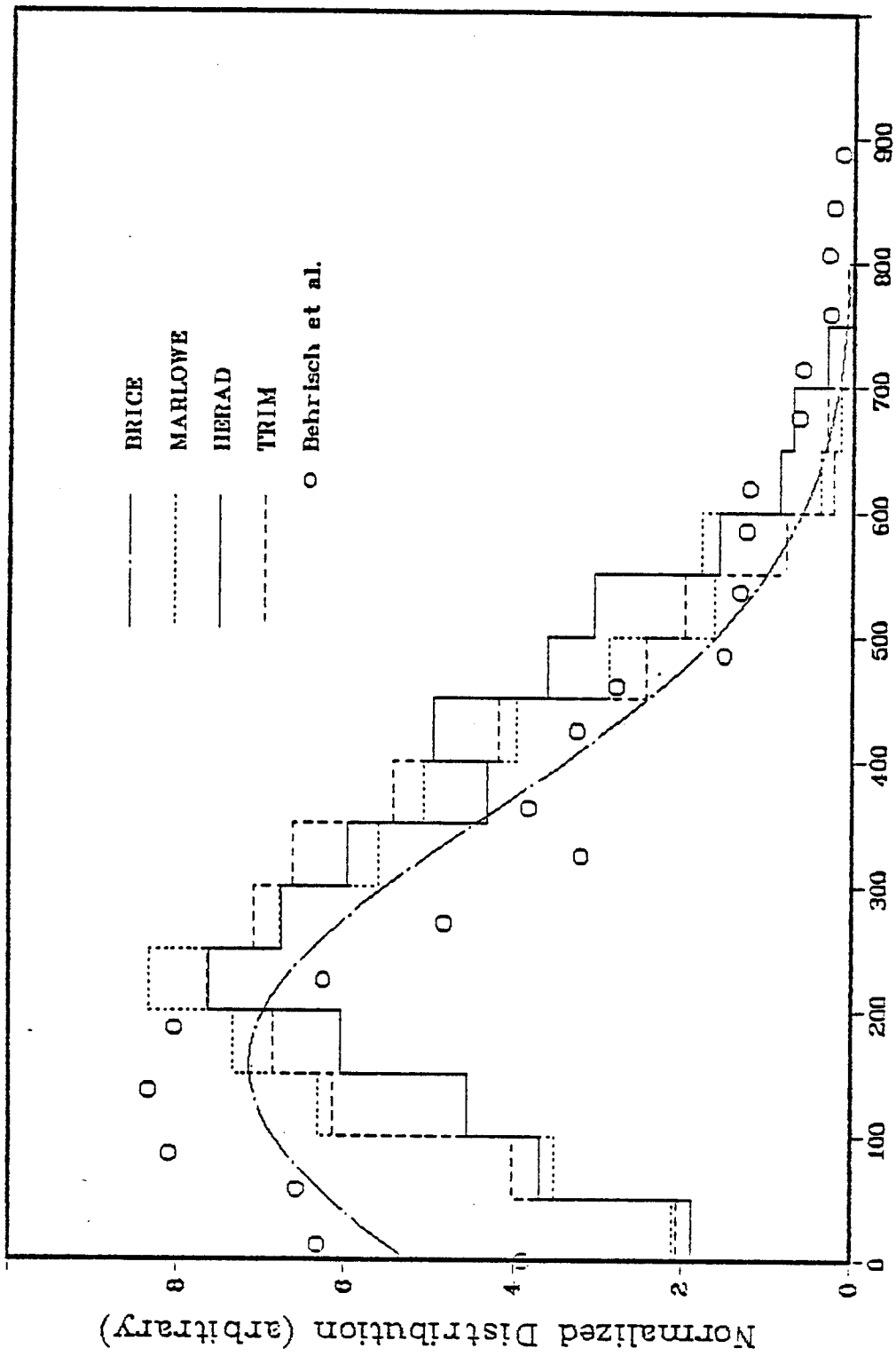

Fig. 6-14. The depth distribution for 4 keV He^3 on Ni. All curves are normalized to the same area.

particles who have neither transmitted or backscattered, and the statistics are made only for these particles.

None of the codes can predict full agreement with the data. One should realize that the depth measurements for low energy implanted ions are difficult and highly uncertain. Accurate measurements are needed in this energy region before more definitive statements can be made about the various models.

VI-3-4. Low Energy Heavy Ions in Silicon and Aluminum

There have recently been many experimental studies of the range of low energy heavy ions in Si and Al because of their importance in the semi-conductor industry. Unfortunately, it is a very rare event to find exactly the same ion with the same energy used in more than one experiment. Combasson et al. [16] reviewed some of these experimental results and pointed out the uncertainties in the data because of the known and the unknown conditions in which these experiments were done. Some of the conditions are the target preparation, energy calibration, target density topography, oxide layer, crystallinity and composition.

In most of these experiments the observed ranges are often considerably larger than the calculated ranges. In the following we present our results compared to the experimental results of Oetzmann et al. [17], Combasson et al. [16], and Grant et al. [18].

Figure 6-15 shows predictions from the HERAD code for 5, 10, 15, 30, and 60 keV antimony ions incident on silicon. The results are compared to BRICE, TRIM, and the experimental results of Oetzmann et

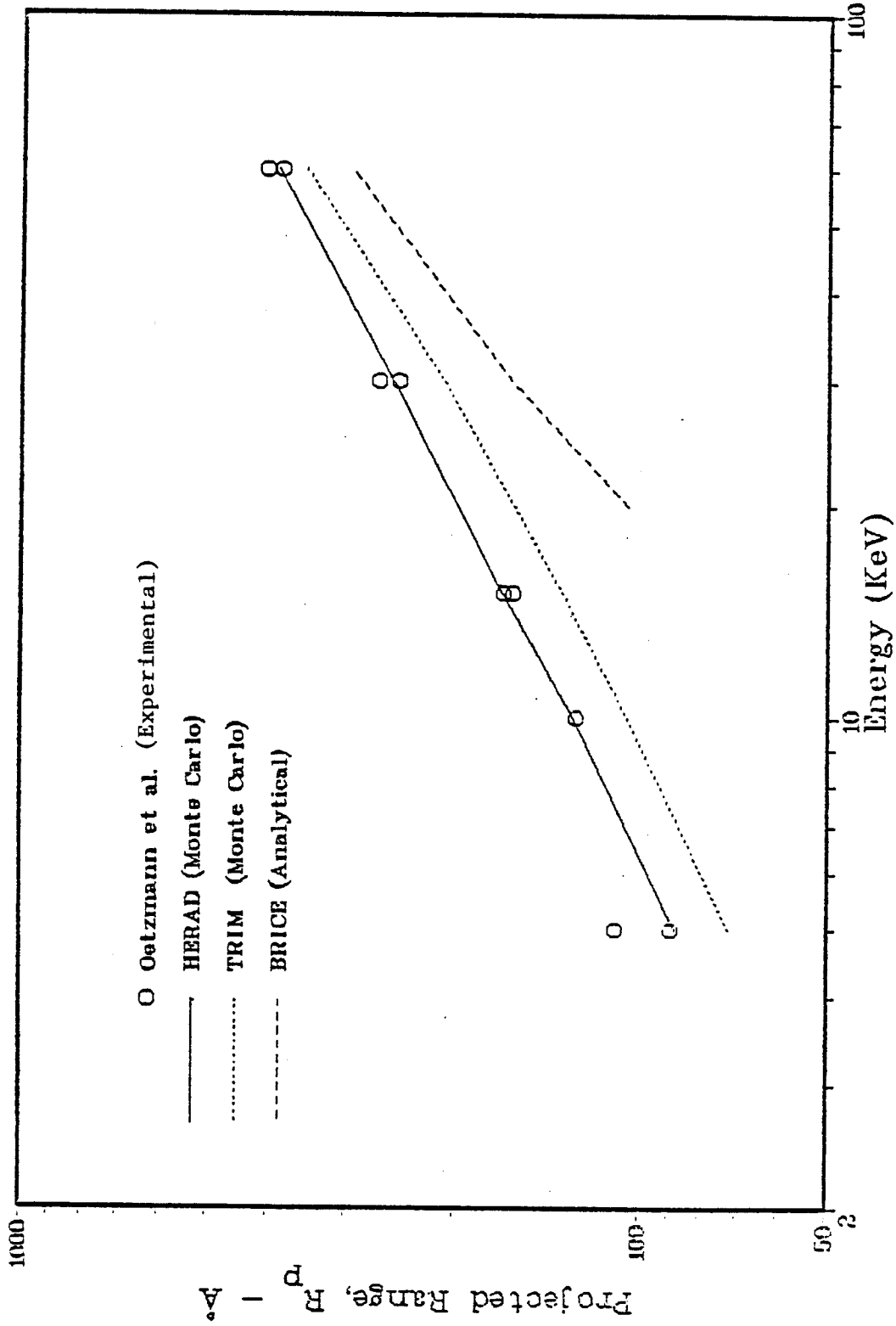

Fig. 6-15. The projected range for 5, 10, 15, 30, and 60 keV Sb-Si.

al. [17]. There is an excellent agreement between our results and the experimental data. The use of the Born-Mayer potential for energies less than the limit energy given by Eq. (5.11) is the main reason for this good agreement. Moliere or Thomas-Fermi potential used by TRIM and BRICE, respectively, for such very low energy would increase the nuclear stopping and consequently would underestimate the ranges.

Table 6-8 shows the projected ranges and the straggling in the projected ranges obtained by Combasson et al. [16] for different ions with different energies incident on Si together with HERAD results. Table 6.9 shows the comparison in the case of the aluminum target. The agreement is excellent in case of Si and with respect to the projected range in Al. With respect to the straggling in the projected range the agreement of our result with the experimental result is reasonable and is within the experimental errors which were the case of Si ±7% in R_p and ±10% in ΔR_p.

Although the predicted projected ranges in Al by HERAD agree well with the experimental data there are substantial disagreements with respect to the straggling in the projected range. Combasson et al. [16] discussed the experimental difficulties in reproducing the range data in Al and questioned the measured straggling because of these difficulties. Bister et al. [19] who used the Dirac-Fock potential in their Monte Carlo calculation, found larger disagreement in the straggling between their results and Combasson et al. results than we have.

TABLE 6-8

Comparison Between HERAD Results (Calc.) and the Experimental Results (Obs.) of Combasson et al.[15] for Eu, Gd, Tb, and Dy Ions in Silicon

Ion	E (KeV)	20	40	60	80	100	120	160	190
$^{63}Eu^{153}$									
	R_p (obs.)	159	236	318	352		496	656	684
	R_p (calc.)	162	246	322	382		514	680	755
	ΔR_p (obs.)	50	81	92	125		154	190	222
	ΔR_p (calc.)	42	64	84	108		140	175	198
$^{63}Gd^{158}$									
	R_p (obs.)	153	246	316	387		503	609	707
	R_p (calc.)	159	250	323	390		523	653	732
	ΔR_p (obs.)	48	77	97	122		166	185	203
	ΔR_p (calc.)	42	63	92	103		133	172	196
$^{65}Tb^{159}$									
	R_p (obs.)	169	251	313	367	434	501	611	685
	R_p (calc.)	163	248	317	380	451	517	633	712
	ΔR_p (obs.)	50	86	97	118	123	160	193	233
	ΔR_p (calc.)	41	65	84	102	118	139	166	188

TABLE 6-8. (Continued)

Ion	E (KeV)	20	40	60	80	100	120	160	190
$66_{Dy}164$									
	R_p (obs.)	169	252	334	371	447	505	603	704
	R_p (calc.)	164	246	319	387	450	519	645	730
	ΔR_p (obs.)	56	81	111	115	131	171	187	211
	ΔR_p (calc.)	40	63	82	102	120	140	165	193

TABLE 6-9

Experimental and Calculated Ranges for Different Implants on Al

Ion	Energy	R_p		ΔR_p	
		Obs.	Calc. HERAD	Obs.	Calc. HERAD
$^{55}Cs^{133}$	80	413±35	429	206±50	115
	100	470±20	487	209	133
	150	665±35	651	232	170
	200	827±35	800	285	207
$^{57}La^{139}$	80	418±35	431	237	112
	100	475±35	489	247	130
	150	677±35	648	267	170
	200	824±35	795	290	200
$^{59}Pr^{141}$	100	385±35	482	285	120
$^{63}Eu^{153}$	100	445±35	473	277	120
$^{65}Tb^{159}$	100	457±50	480	216	118
$^{66}Dy^{164}$	100	463±50	492	195	117
$^{67}Ho^{165}$	80	445±35	434	167	100
	100	485±35	489	170	113
	150	598±35	631	184	152
	200	700±35	760	242	187
$^{68}Er^{166}$	100	410±35	482	221	116
$^{71}Lu^{175}$	100	466	486	203	110
$^{72}Hf^{180}$	100	474±50	489	259	112
$^{78}Pt^{195}$	100	467±50	484	222	107
$^{79}Au^{197}$	80	477±50	431	262	100
	100	551±35	495	275	106
	150	673±35	637	284	133
	200	781±35	756	313	170

Finally, in Table 6-10 summarizes the prediction of HERAD compared to the experimental results of Grant et al. [18]. There is a very good agreement between the two, except for the straggling ΔR_p and ΔR_L in the case of Bi (200 keV), Bi (400 keV), Cu (40 keV) and Kr (40 keV) where there is more than a 25% difference. However, the agreement of HERAD is much better than the analytical results which were taken from Furukawa et al. [20] and Schoitt [21].

The disagreements mentioned above led us to study the sensitivity of HERAD results to some physical and artificial parameters used in the program. As suggested by Maynard [22] and outlined in Ref. 23, a simple regression analysis was made. The parameters used were the screening length, the cutoff energy, the minimum angle of scattering, the minimum step length between two successive collisions, the energy limit for switching to Born-Mayer or the hard sphere potential, and the use of other potentials. Our results show that in the low energy region, the use of the following potentials will give decreasing ranges according to the following order, Bohr, Lenz-Jensen, Moliere, Thomas-Fermi, and Thomas-Fermi-Sommerfeld. However, the ratio of $\Delta R_p/R_p$ is not so sensitive to the choice of the potential. Decreasing the energy limit for switching to the B-M potential will decrease the ranges but again no noticeable effect on ΔR_p. Using Firsov's screening length will give always longer ranges and slightly larger values of ΔR_p, and this may explain the high values of the projected range obtained from TRIM. Unfortunately even when the resulting parameters from the regression analysis work well

TABLE 6-10

Experimental Ranges of Grant et al.[18] Compared to HERAD's Results and to the Analytical Results of Furukawa[20] and Shiott[21]

Case	E (KeV)	R_p			ΔR_p			ΔR_L		
		Obs.	$\frac{R_p \text{Obs.}}{R_p \text{Anal.}}$	$\frac{R_p \text{Obs.}}{R_p \text{HERAD}}$	ΔR_pObs.	$\frac{\Delta R_p \text{Obs.}}{\Delta R_p \text{Anal.}}$	$\frac{\Delta R_p \text{Obs.}}{\Delta R_p \text{HERAD}}$	Obs.	$\frac{\Delta R_L \text{Obs.}}{\Delta R_L \text{HERAD}}$	$\frac{\Delta R_L \text{Obs.}}{\Delta R_L \text{HERAD}}$
Pb-Si	10	170	2.26	1.05	26	2.30	0.93	33	1.94	0.89
	20	209	1.69	0.92	44	1.69	0.98	44	1.83	0.82
	40	271	1.35	0.85	70	1.45	1.01	62	1.72	0.89
	80	456	1.38	0.95	108	1.36	1.05	92	1.59	0.89
Bi-Si	50	371	1.58	0.97	97	1.72	1.20	67	1.59	0.82
	150	603	1.14	0.86	178	1.40	1.17	141	1.56	0.94
	200	803	1.22	0.96	255	1.60	1.42*	137	1.23	0.75*
	400	1310	1.15	0.98	404	1.48	1.30*	198	1.06	0.72*
Ar-Si	40	458	1.13	1.01	---	---	---	---	---	---
Cu-Si	40	354	1.20	1.01	194	1.49	1.50*	128	1.02	1.04
Kr-Si	40	322	1.28	1.04	144	1.63	1.39*	75	1.17	0.80
Cd-Si	40	301	1.29	0.98	95	1.36	1.10	75	1.44	0.85
W-Si	40	278	1.46	0.86	73	1.60	0.95	68	1.79	0.91

for some cases they are not so good at other energies and different ion-target combinations.

One may conclude that there is an oscillating dependence on the charge of the ion as well as the target which is not included in both the electronic and the nuclear stopping formulae.

VI-4. Damage Calculations

The comparison that was just made with different codes and different experimental results for various ion-target-energy combinations shows that HERAD gives very good agreement with respect to range and ion distribution. In fact, in some cases HERAD gives better agreement than the previous codes, especially at low energies with the exception of a few disagreements mentioned in the previous section. The importance of this low energy region, where most of the primary knock atoms have their energies, cannot be overemphasized.

The damage calculations are straightforward and can be expressed in anyone of the following:

1) First, the damage could be expressed as the amount of energy that is calculated using Linhdard- Robinson partition formula given by Eq. (5.43). If the incident ion loses in a collision with a target atom energy T, then using Eq. (5.43) one obtains the amount of energy T_d which is available for damage (i.e. displacement). Only values of T which are greater than the displacment energy E_d are considered. If T is less than E_d, T is assumed to be spent in lattice vibrations (phonons).

2) Second, it could be the damage energy transported by the PKAs. In this case, a PKA created with energy T in a collision of the incident ion with a target atom is followed until its energy falls below a cutoff energy E_c, which has a default value of $2E_d$. The electronic energy loss along the PKA's trajectory is calculated and is subtacted from the initial energy T, and the remainder, is deposited at the end point, of the PKA trajectory as the damage energy.

3) Third, it could be full defect configuration, i.e. the final spatial distribution of vacancies and interstitials generated during the slowing down of every moving particle in the entire cascades. The information available in (2) is calculated too in this case. This is the most expensive choice, but we believe it is the most accurate one.

It should be mentioned that choice number 1 is the default choice in the program and is always calculated.

In the following we shall present four cases of the damage calculations. The first one serves as an illustration of the main features of the calculations, and was chosen to be 901.3 keV Be on U (this energy corresponds to 100 keV per atomic mass units for Be). The next two cases we will consider are 14 MeV Cu on nickel with and without the voids included. The last case is for 20 keV He on nickel.

VI-4-1. Be Ions on U

Complete damage calculations have been made for this case. Figure 6-16 shows the depth distribution of the incident Be ions as obtained from the HERAD and BRICE codes. HERAD distribution shows a peak of the ion concentration farther from the front surface than BRICE. Table 6-11 gives the calculated statistics of the ranges from the two codes. One thousand histories have been used in this run, and as shown in Table 6-11, 992 particles pentrated the target. The other 8 particles were reflected, thus the reflection coefficient of Be ions is .008.

Figure 6-17 shows the damage energy distributions of BRICE and that obtained from HERAD with and without recoil transport. The transported damage energy as calculated by BRICE (using Lindhard-Robinson partition formula and deposited at the average depth of the recoils from collision point of the ion) was 29.56 keV. The corresponding value given by HERAD and using Lindhard-Robinson formula is 29.622 keV. Allowing for the recoil transport, the transported damage energy is 30.323 keV, which shows that the LSS-Robinson partition equation (Eq. 5.43), slightly understimates the damage energy and overestimates the electronic energy loss of the PKAs. Because of the heavy mass of the recoils one cannot see a noticeable difference between the transported damage by the recoils and that deposited in the ions' collision points. The BRICE first and second moment of the damage distribution are 7123 Å and 928 x 10^4 $Å^2$, respectively. The corresponding values of HERAD are 7512 Å and 963 x 10^4 $Å^2$. HERAD

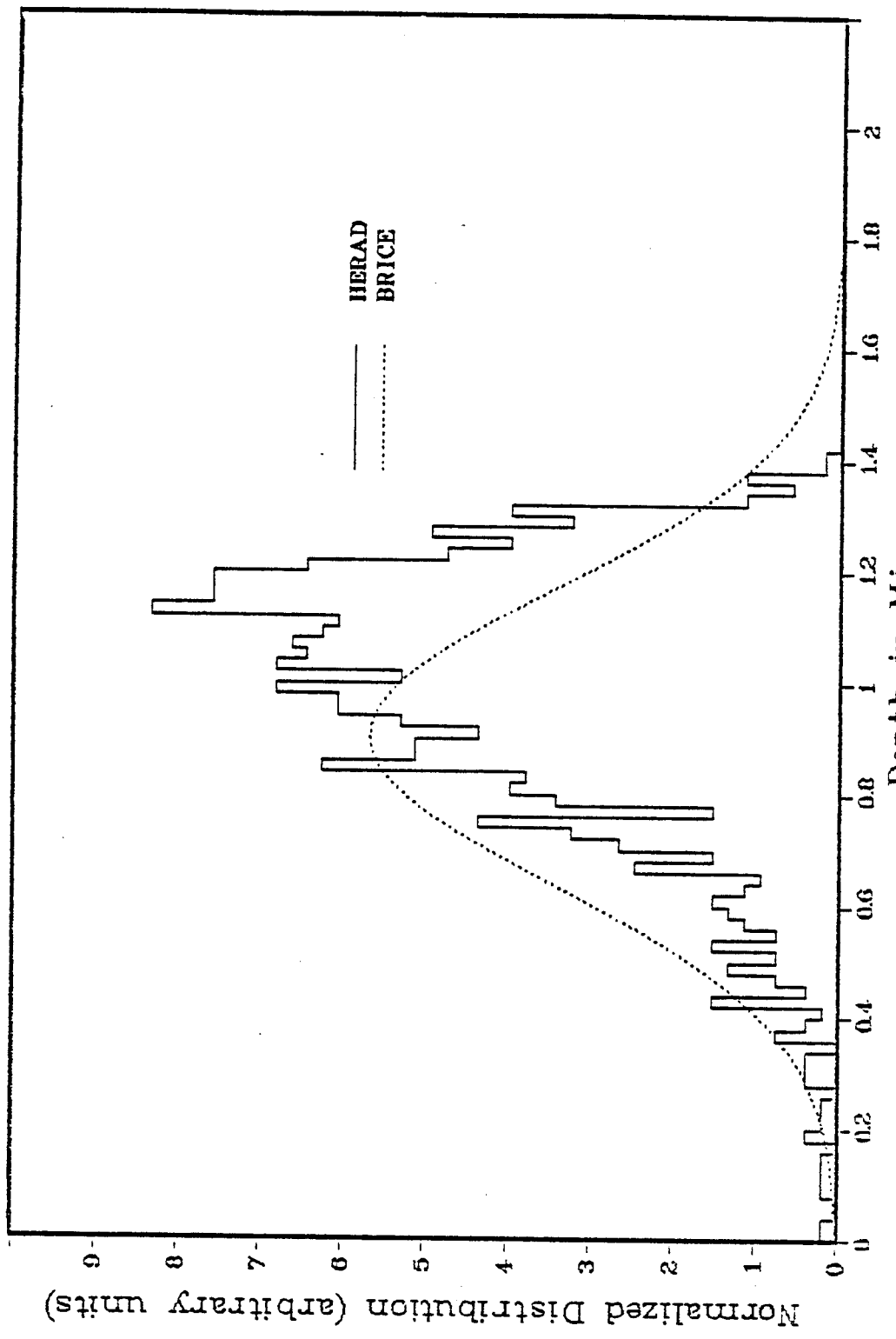

Fig. 6-16. The depth distribution for 901.3 keV Be ions incident on U target.

TABLE 6-11

Results of Range Calculation from the Different BRICE and HERAD Computer Codes for 901.3 keV Be-U

Ranges (Å)	Code	Mean	Median	Std. Dev.	Skewness	Kurtosis	Error	# Hist.
1) Depth	BRICE	9032.		2654.				
	HERAD	9855.	10243.	2345.	-1.04	1.21	74.	992
2) Path	BRICE	14948.						
	HERAD	15661.	15601.	289.	-0.89	1.45	9.	992
3) Perpendicular	BRICE			4605.				
	HERAD	4183.	4133.	1944.	0.30	-0.30	62.	992
4) Vector Range	HERAD	10978.	11213.	1838.	-0.88	0.94	58.	992

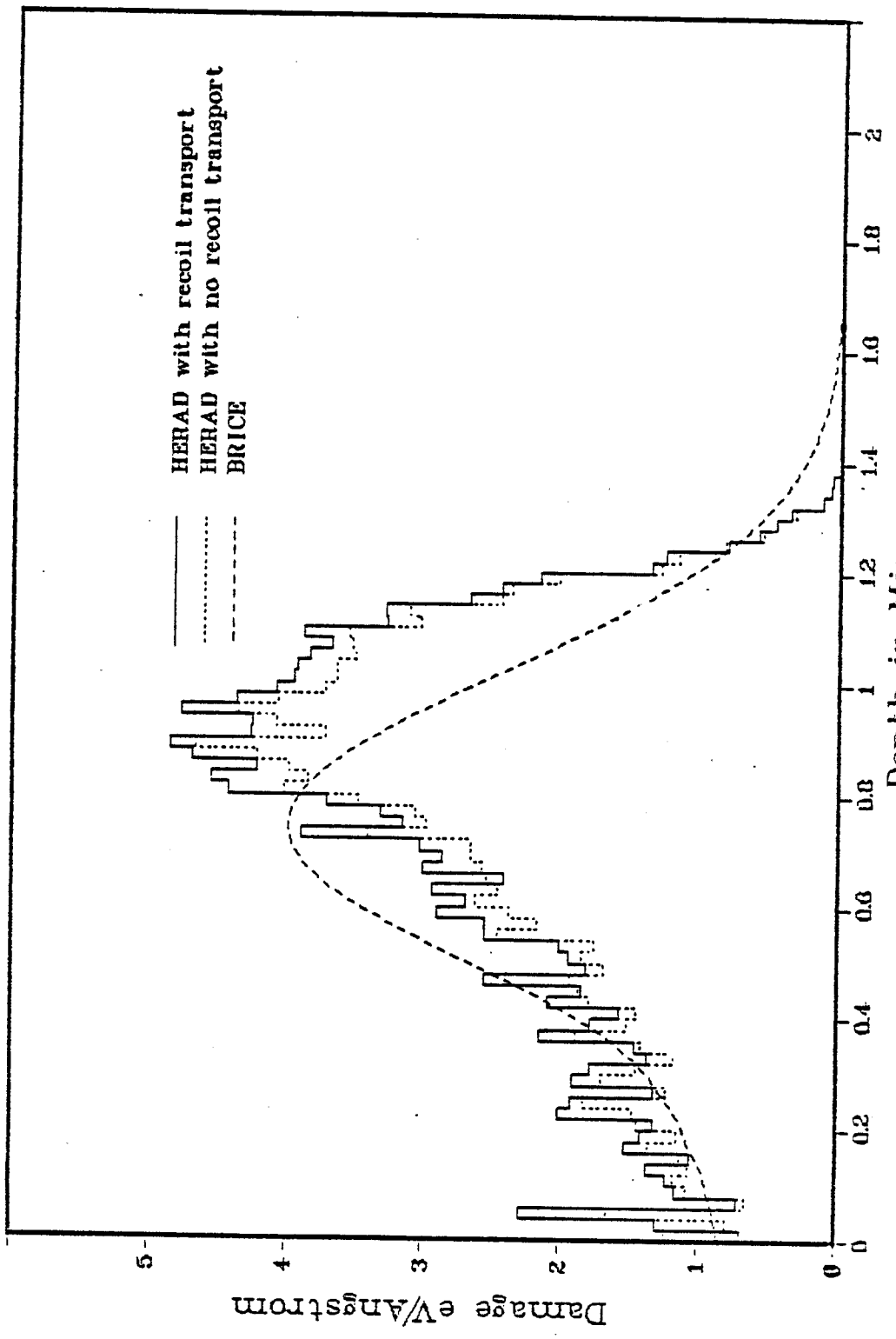

Fig. 6-17. The deposited damage energy for 901.3 keV Be ions incident on Uranium.

damage distribution is more skewed to the front surface and more deeper into the solid than that calculated from the BRICE code.

Figure 6-18 shows the distributions of different defects,i.e. vacancies, interstitials, and those vacancies and interstitials that are generated near each other. The latter quantity is registered when an atom is displaced but does not have energy much greater than the cutoff energy ($2E_d$) to produce more displacements. The program records this event as a NEAR V-I PAIR on the figure. Also shown on the same figure is the spatial distribution of the replacement events. Because of the heavy mass of the target and the relatively large width of the histogram interval (200 Å), one cannot see the difference between the vacancies and the interstitials distribution. The peak of the interstitial distribution is supposed to be deeper than for the vacancies. Also, one should remember that this is a one dimensional figure and cannot reflect the 3-D spatial distribution of both vacancies and interstitials.

Finally, Fig. 6-19 shows a comparison between the HERAD defect distribution and BRICE defect distribution, which was calculated using the Kinchen and Peace displacement model (damage efficiency = 0.8 and displacement energy = 25 eV). The total number of defects produced according to this model from BRICE is 473 defects, from HERAD without recoil transport is 474, and from HERAD with the recoil transport is 485 defects. The number of defects directly calculated from HERAD is 422. Thus K-P model with damage efficiency of 0.8 overestimates the number of defects by a factor of 15%. If the

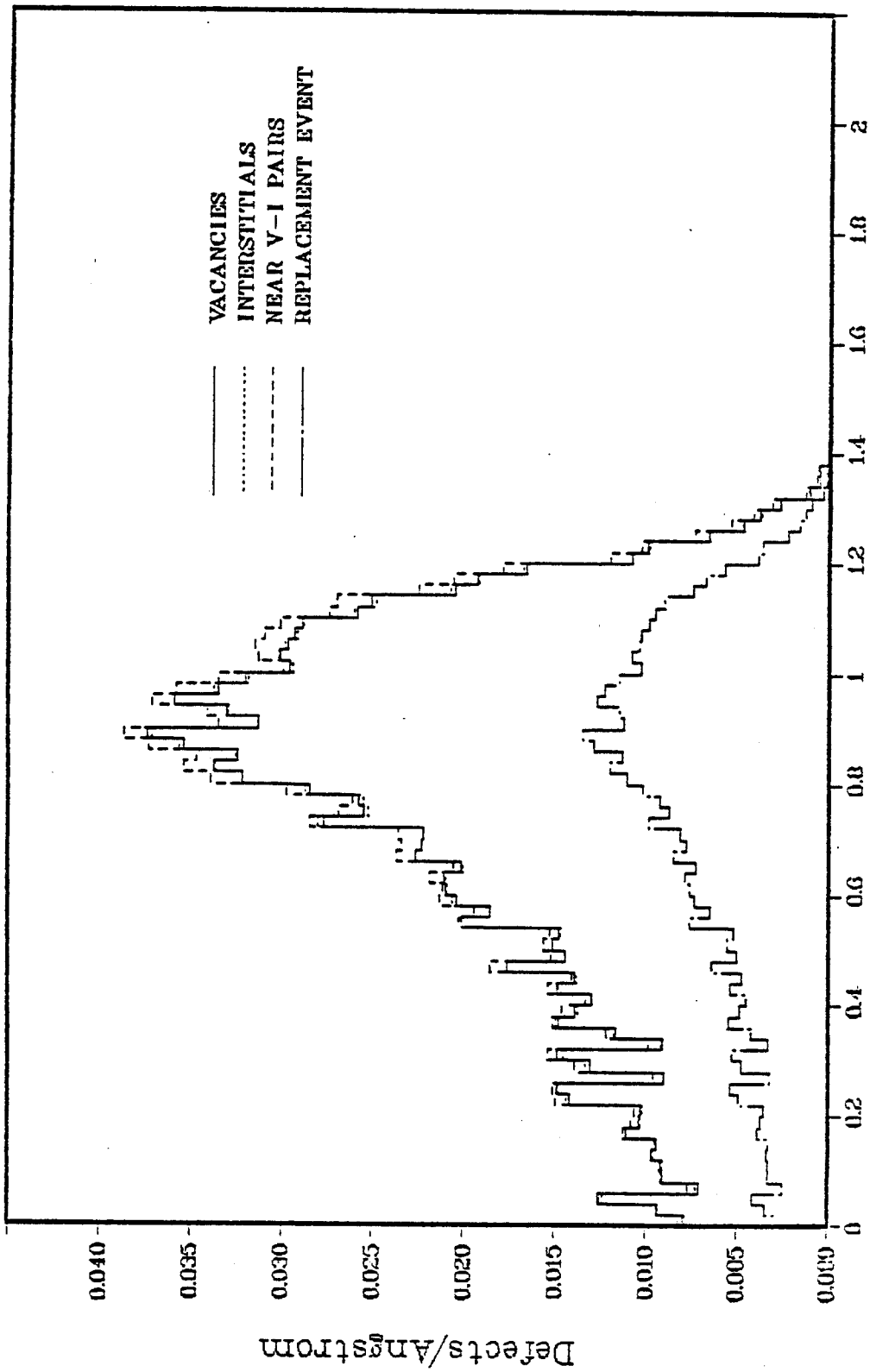

Fig. 6-18. Defect distribution for the case of 901.3 keV Be on U.

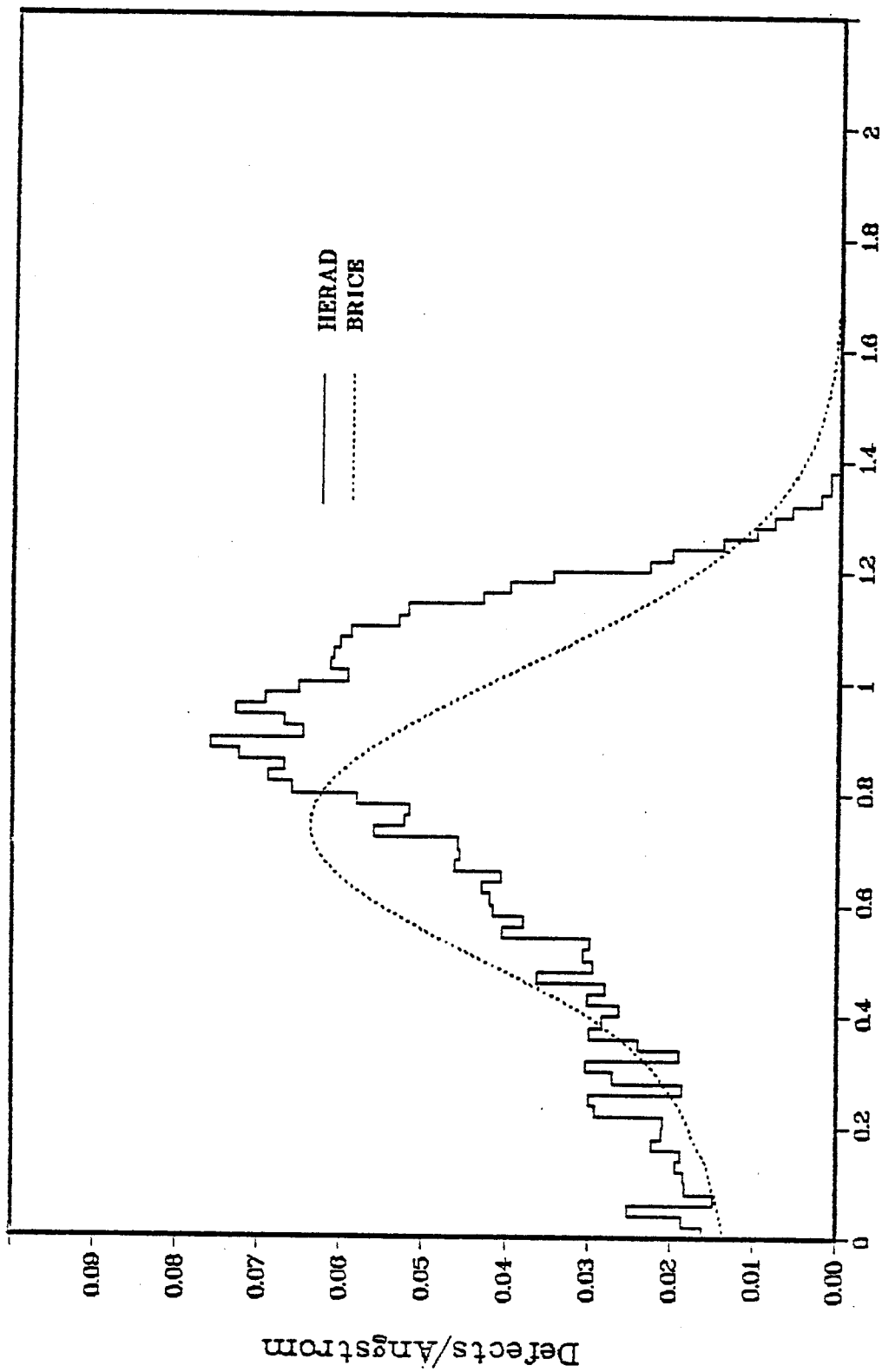

Fig. 6-19. The defect distribution for the case of 901.3 keV Be ions on U.

damage efficiency is reduced to 0.7, then using it with the K-P model gives the right number of defects.

In the following three pages we present only a portion of HERAD output which includes the statistics, the distributions and a complete energy-particle balance. The computer output on the first page shows the statistics of the projected range (penetration), the total path, the perpendicular range (spread) which is a scalar quantity, the vector range, and the perpendicular range (R-perp) which is a vector quantity whose mean equals zero. Next on the same page, the distributions of the first four ranges mentioned above are listed. Each histogram runs from left to the far right of the page. The second page shows the complete energy-particle balance. The third page shows a list of the normalized distributions of the following quantities along the depth: the collisions of the incident ion (coll.), electronic and the nuclear energy lost by the incident ion (ioniz., nuclear), the damage energy (displac.) and electronic energy loss (rec-ionz) as calculated using Lindhard-Robinson partition formula, the subthreshold energy lost (phonon) by the ions, the transported damage energy (dmg/pka), the electronic energy loss of the PKAs (se/pka), and the last four columns gives the distributions of the vacancies, interstitials, near V-I pair, and the replacement events. The last two histograms gives the energy distribution of the backscattered ions and the sputtered atoms, respectively.

be+ ions (901.3 kev) on u target

analysis of primary recoil ranges (992 particles)

	mean	median	variance	skewness	kurtosis	std dev.	error
penetration	9854.73	10243.2	0.550029e+07	-1.04462	1.21463	2345.27	74.5000
total path	15561.2	15600.7	83713.6	-0.886393	1.45162	289.333	9.19097
spread	4182.67	4133.33	0.377999e+07	0.296512	-0.301302	1944.22	61.7602
vector range	10977.7	11213.0	0.337993e+07	-0.876502	0.936920	1838.46	58.4006
R-perp			2.127469e+07			4612.45	

vector range distribution function
(histogram channel width 200.00)

0	0	0	0	0	0	0	0	0	0	0	0	0	0	0	0	1	0	0	1
0	1	1	1	1	4	2	2	1	2	3	2	4	2	8	7	1	8	9	7
14	11	7	16	16	16	27	31	25	29	30	27	37	44	49	46	46	35	52	35
42	59	51	35	36	27	25	16	18	12	5	3	1	0	1	0	0	0	0	0
0	0	0	0	0	0	0	0	0	0	0	0	0	0	0	0	0	0	0	0

penteration distribution function
(histogram channel width 200.00)

0	0	1	0	1	2	0	0	3	1	2	0	2	0	3	0	4	3	2	4
2	2	3	4	3	3	8	8	10	0	5	10	11	10	11	5	12	17	15	9
23	23	25	20	30	28	24	28	38	39	35	37	35	40	23	38	48	38	36	36
40	35	21	24	17	16	8	8	3	0	1	0	0	0	0	0	0	0	0	0
0	0	0	0	0	0	0	0	0	0	0	0	0	0	0	0	0	0	0	0

spread distribution function
(histogram channel width 200.00)

0	2	7	9	15	27	15	21	32	19	30	28	29	26	30	39	34	33	33	37
45	40	44	39	25	26	39	31	26	26	30	25	20	17	21	10	6	8	13	6
5	5	3	1	3	2	2	4	1	1	0	0	2	0	0	0	0	0	0	0
0	0	0	0	0	0	0	0	0	0	0	0	0	0	0	0	0	0	0	0
0	0	0	0	0	0	0	0	0	0	0	0	0	0	0	0	0	0	0	0

total path distribution function
(histogram channel width 200.00)

0	0	0	0	0	0	0	0	0	0	0	0	0	0	0	0	0	0	0	0
0	0	0	0	0	0	0	0	0	0	0	0	0	0	0	0	0	0	0	0
0	0	0	0	0	0	0	0	0	0	0	0	0	0	0	0	0	0	0	0
0	0	0	0	0	0	0	0	0	0	0	0	0	0	0	0	0	0	0	0
24	2	0	0	0	0	0	0	0	0	1	2	3	10	29	63	142	245	297	174
										0	0	0	0	0	0	0	0	0	0

1

be+ ions (901.3 kev) on u target

ION'S average num. of collisions = 663.
ION'S average num. backscattered = 8.0000e-03

ION'S energy partition

incident (average)	= 901.30	
1) - backs.	= 1.63	
2) - threshold	= 0.02	
3) - elect. (ions)	= 662.78	
4) - nuclear (ions)	= 36.87	
a) - recoil elect.	=	5.14
b) - displacement	=	29.62
c) - phonon	=	2.11
5) - total elect.	=	867.91

ALL moving particles : INCIDENT, PRIMARIES, and SECONDARIES will be followed

The Average NUCLEAR Energy loss by an ION = 36.871

Subthreshold collisions (Phonon) = 2.114
Net PKAS' energy = 34.757<1><2><4>

(A) Using Lindhard (Robinson) Partition Formula :

Effective Damage Energy = 29.622
Electronic Energy = 5.136

(B) Following the PKAS :

Effective Damage Transfered	= 30.323(1)		
Electronic Energy Loss	= 4.434(1)(2)		
Binding Energy Loss	= 0.000(1)(2)		
Sputtered Energy	= 0.000 (2)	No. of Sputtered PKAS	= 0.00000
Energy lost in replacement	= 0.210 (2)		
Cut-off Energy	= 3.491 (2)		
Subthreshold Energy Loss(phonon)	= 1.292 (2)		
Net Nuclear Energy to Secondaries	= 25.331 (2)<3>		

sum of [(1)'s] = 34.757<1>
sum of [(2)'s] = 34.757 <2>

The 'Effective Damage Transfered' has the following DISTRIBUION'S PARAMETERS :

total energy in distr. = 30.323

	mean	variance	skewness	kurtosis	std dev.	error
depth	7512.10	0.963125e+07	-0.491577	-0.625932	3103.43	98.1821
spread	2594.29	0.386771e+07	0.727934	-3.288203e-02	1966.65	62.2220
x	-49.9166	0.492839e+07	-0.138024	0.832251	2220.00	70.2376
y	-2.71521	0.566717e+07	-2.421567e-02	1.09053	2380.58	75.3163
r spread	8123.37	1.067178e+07	-0.616120	-0.544085	3266.77	103.355

average no. of pka's 103.258

(C) FOLLOWING ALL PARTICLES of ALL GENERATIONS :

	including only the SECONDARIES		including SECONDARIES + PKAS	
Electronic Energy Loss	= 7.745(3)		12.179(4)	
BINDING Energy Loss	= 0.000(3)		0.000(4)	
Phonon Energy Loss	= 3.540(3)		4.832(4)	
Sputtered Energy & No. sput.	= 0.000(3)	1.000e-03	0.000(4)	1.000e-03
Energy Loss in Replacement	= 0.652(3)		0.862(4)	
Cut-off Energy Loss	= 13.394(3)		16.885(4)	
sum	= 25.331<3>		34.757<4>	

No. of VACANCIES = 230.312
No. of INTERSTITIALS = 230.311
No. of (near) V-I = 192.367
No. of Replacement events = 64.595

Average No. of PKAS = 103.
Average No. of cascades = 85.
Average No. of Atoms in cascades = 261.
Average No. of ALL moving Atoms = 364.
maximum cascade storage = 55

```
1
                      be+ ions (901.3  kev)   on u target

          **  distribution (normalized for  1 particles)  **

                          interval  =  200.00

interval
  no.  coll.  ioniz.  nuclear    displac.   rec-ionz    phonon      dmg/pka     se/pka      se/scnd     V     I     V-I    Rplc
                                                                                                                   (near)

   1    0.9   21.6   0.12       0.10       1.68e-02    5.66e-03    0.10        1.49e-02    2.53e-02    0.8   0.8   0.8    0.2
   2    0.9   21.6   0.13       0.10       1.80e-02    5.73e-03    0.10        1.65e-02    2.61e-02    0.8   0.8   0.7    0.2
   3    1.7   21.4   0.29       0.23       4.93e-02    9.77e-03    0.25        3.98e-02    7.06e-02    1.8   1.8   1.5    0.5
   4    1.2   21.4   0.23       0.19       3.58e-02    6.87e-03    0.20        2.91e-02    5.46e-02    1.5   1.5   1.2    0.4
   5    1.7   21.2   0.29       0.23       4.86e-02    9.01e-03    0.15        2.60e-02    4.89e-02    1.4   1.4   1.2    0.4
   6    1.7   21.3   0.21       0.17       2.96e-02    9.78e-03    0.27        3.01e-02    7.34e-02    1.7   1.7   1.4    0.5
   7    1.6   20.8   0.20       0.16       3.13e-02    9.31e-03    0.16        2.28e-02    4.89e-02    1.3   1.4   1.1    0.4
   8    1.7   20.4   0.30       0.24       5.06e-02    9.41e-03    0.26        3.30e-02    7.67e-02    1.8   1.8   1.5    0.5
   9    2.0   20.3   0.23       0.19       3.40e-02    1.08e-02    0.21        2.54e-02    5.43e-02    1.5   1.5   1.3    0.4
  10    2.2   20.2   0.40       0.31       7.06e-02    1.21e-02    0.26        4.14e-02    8.92e-02    2.1   2.0   1.7    0.6
  11    2.2   20.0   0.19       0.16       2.58e-02    1.19e-02    0.23        2.41e-02    6.14e-02    1.6   1.6   1.4    0.5
  12    1.8   19.8   0.31       0.25       4.71e-02    1.09e-02    0.25        3.60e-02    6.32e-02    1.8   1.8   1.4    0.5
  13    1.9   19.6   0.39       0.31       6.60e-02    1.11e-02    0.28        4.56e-02    9.11e-02    2.2   2.2   1.8    0.6
  14    2.0   19.3   0.26       0.21       3.74e-02    1.14e-02    0.28        3.30e-02    7.77e-02    2.0   2.0   1.6    0.5
  15    2.4   19.0   0.28       0.22       4.23e-02    1.30e-02    0.21        3.19e-02    6.67e-02    1.7   1.8   1.5    0.5
  16    2.2   18.9   0.32       0.26       5.22e-02    1.21e-02    0.29        4.29e-02    7.50e-02    2.0   1.9   1.6    0.6
  17    2.9   19.0   0.33       0.27       5.25e-02    1.48e-02    0.29        3.56e-02    8.06e-02    2.1   2.1   1.7    0.6
  18    3.0   18.5   0.53       0.42       9.80e-02    1.46e-02    0.27        5.53e-02    0.11        2.7   2.7   2.2    0.8
  19    3.0   18.2   0.46       0.37       7.72e-02    1.45e-02    0.54        5.79e-02    0.14        3.2   3.2   2.6    0.9
  20    3.5   17.9   0.30       0.24       4.08e-02    1.67e-02    0.27        4.02e-02    6.95e-02    2.0   2.1   1.7    0.6
  21    3.5   17.7   0.33       0.26       4.75e-02    1.71e-02    0.27        4.13e-02    7.01e-02    2.1   2.1   1.8    0.5
  22    3.4   17.3   0.46       0.37       7.41e-02    1.66e-02    0.36        4.89e-02    0.10        2.7   2.6   2.1    0.7
  23    3.7   17.3   0.45       0.36       7.02e-02    1.73e-02    0.43        4.83e-02    0.11        2.9   2.9   2.4    0.8
  24    3.9   17.2   0.50       0.40       8.15e-02    1.85e-02    0.37        5.45e-02    0.11        2.9   2.9   2.3    0.8
  25    4.1   17.0   0.50       0.40       7.70e-02    1.94e-02    0.44        6.07e-02    0.14        3.4   3.4   2.8    1.0
  26    4.8   17.1   0.44       0.36       6.52e-02    2.16e-02    0.40        5.10e-02    0.10        2.8   2.8   2.5    0.8
  27    6.3   17.0   0.56       0.45       8.41e-02    2.56e-02    0.48        6.73e-02    0.12        3.5   3.4   3.0    1.0
  28    7.1   16.6   0.51       0.41       7.48e-02    2.79e-02    0.38        5.61e-02    0.10        3.0   3.1   2.5    0.9
  29    6.4   16.2   0.64       0.51       0.10        2.58e-02    0.56        6.82e-02    0.17        4.1   4.1   3.3    1.2
  30    4.8   15.9   0.69       0.55       0.11        2.24e-02    0.57        7.89e-02    0.17        4.2   4.2   3.3    1.2
  31    5.7   15.7   0.49       0.40       7.03e-02    2.54e-02    0.44        5.81e-02    0.11        3.1   3.1   2.7    0.9
  32    6.9   15.5   0.61       0.49       9.42e-02    2.98e-02    0.52        6.60e-02    0.14        3.7   3.7   3.0    1.0
  33    8.1   15.4   0.68       0.54       0.10        3.18e-02    0.51        8.40e-02    0.15        4.2   4.1   3.4    1.2
  34    7.8   14.9   0.63       0.51       9.15e-02    2.99e-02    0.53        7.15e-02    0.13        3.9   3.9   3.2    1.1
  35    9.6   14.2   0.59       0.47       8.12e-02    3.62e-02    0.51        7.84e-02    0.13        3.3   4.0   3.3    1.1
  36    9.0   14.0   0.73       0.58       0.10        3.50e-02    0.54        8.06e-02    0.14        4.2   4.2   3.5    1.2
  37    9.9   13.7   0.68       0.55       9.79e-02    3.73e-02    0.61        8.12e-02    0.16        4.4   4.4   3.7    1.2
  38   11.8   13.2   0.75       0.60       0.10        4.22e-02    0.61        9.14e-02    0.16        4.7   4.7   3.9    1.4
  39   11.9   12.9   0.73       0.59       9.94e-02    4.18e-02    0.63        9.05e-02    0.15        4.6   4.6   3.7    1.3
  40   12.4   12.8   0.82       0.66       0.11        4.45e-02    0.66        9.82e-02    0.18        5.2   5.2   4.4    1.4
  41   13.9   12.4   0.90       0.72       0.12        4.76e-02    0.72        0.10        0.18        5.5   5.5   4.8    1.5
  42   15.3   12.1   0.96       0.77       0.13        5.39e-02    0.78        0.11        0.19        5.9   5.8   4.8    1.7
  43   17.1   11.7   0.99       0.80       0.13        5.54e-02    0.87        0.12        0.21        6.4   6.5   5.4    1.8
  44   17.1   10.9   0.96       0.78       0.13        5.45e-02    0.79        0.11        0.20        6.0   5.9   4.9    1.7
  45   18.8   10.2   0.95       0.76       0.12        5.88e-02    0.75        0.11        0.19        6.0   6.0   5.1    1.7
  46   20.4   10.2    1.1       0.87       0.14        6.32e-02    0.89        0.13        0.21        6.8   6.7   5.7    1.9
  47   17.6    9.3   0.91       0.73       0.12        5.69e-02    0.74        0.11        0.18        5.8   5.9   4.7    1.7
  48   20.3    9.0    1.0       0.84       0.13        6.23e-02    0.84        0.12        0.20        6.6   6.5   5.4    1.8
  49   22.9    8.2    1.0       0.83       0.13        6.66e-02    0.84        0.12        0.21        6.5   6.5   5.5    1.8
  50   23.7    7.6    1.0       0.81       0.13        6.61e-02    0.81        0.12        0.19        6.3   6.4   5.3    1.8
  51   26.5    7.4   0.98       0.79       0.12        7.20e-02    0.81        0.12        0.18        6.4   6.4   5.3    1.8
  52   23.1    6.7   0.97       0.77       0.12        6.53e-02    0.76        0.11        0.18        6.0   6.0   5.1    1.6
  53   22.5    5.9   0.88       0.71       0.11        6.31e-02    0.73        0.11        0.18        5.7   5.7   4.8    1.6
  54   22.8    5.5   0.92       0.74       0.11        6.19e-02    0.74        0.11        0.17        5.8   5.8   4.9    1.6
  55   21.0    4.6   0.79       0.63       9.76e-02    5.68e-02    0.64        9.88e-02    0.14        5.1   5.1   4.4    1.4
  56   23.3    4.1   0.79       0.63       9.76e-02    6.13e-02    0.64        0.10        0.14        5.0   5.0   4.2    1.4
  57   23.3    3.5   0.79       0.63       9.73e-02    6.01e-02    0.63        0.10        0.14        5.1   5.1   4.3    1.4
  58   23.2    2.9   0.67       0.53       8.07e-02    5.58e-02    0.53        8.60e-02    0.11        4.3   4.2   3.5    1.2
  59   19.2    2.2   0.54       0.43       6.37e-02    4.61e-02    0.42        7.11e-02    8.77e-02    3.5   3.5   3.0    1.0
  60   19.5    1.9   0.49       0.39       5.67e-02    4.55e-02    0.38        6.57e-02    7.38e-02    3.1   3.1   2.7    0.9
  61   16.5    1.4   0.41       0.32       4.72e-02    3.91e-02    0.31        5.35e-02    6.20e-02    2.6   2.6   2.2    0.7
  62   13.2    1.0   0.29       0.23       3.27e-02    3.02e-02    0.23        4.09e-02    4.23e-02    1.9   1.9   1.7    0.5
  63   11.6    0.8   0.25       0.19       2.80e-02    2.54e-02    0.18        3.28e-02    3.36e-02    1.5   1.6   1.3    0.4
  64    8.8    0.3   0.17       0.13       1.87e-02    1.97e-02    0.13        2.25e-02    2.57e-02    1.1   1.1   1.0    0.3
  65    6.1    0.3   0.10       8.16e-02   1.08e-02    1.39e-02    8.03e-02    1.49e-02    1.19e-02    0.7   0.7   0.6    0.2
  66    5.1    0.2   7.29e-02   5.43e-02   6.88e-03    1.15e-02    5.09e-02    9.56e-03    7.18e-03    0.5   0.5   0.4    0.1
  67    4.1    0.1   5.55e-02   4.15e-02   5.36e-03    8.56e-03    4.09e-02    7.47e-03    5.84e-03    0.4   0.4   0.3    0.1
  68    2.1    0.1   2.53e-02   1.96e-02   2.41e-03    4.31e-03    1.90e-02    3.56e-03    2.15e-03    0.2   0.2   0.1    0.0
  69    0.8    0.0   1.33e-02   1.00e-02   1.40e-03    1.86e-03    8.07e-03    1.45e-03    1.78e-03    0.1   0.1   0.1    0.0
  70    0.1    0.0   4.22e-04   2.55e-04   2.55e-05    1.41e-04    1.45e-03    2.01e-04    8.85e-05    0.0   0.0   0.0    0.0
  71    0.2    0.0   2.55e-03   1.38e-03   2.32e-04    4.38e-04    1.63e-03    4.37e-04    1.85e-04    0.0   0.0   0.0    0.0
  72    0.0    0.0   0.00       0.00       0.00        0.00        1.72e-03    1.43e-04    5.15e-04    0.0   0.0   0.0    0.0
  73    0.0    0.0   0.00       0.00       0.00        0.00        0.00        0.00        5.59e-06    0.0   0.0   0.0    0.0
  74    0.0    0.0   0.00       0.00       0.00        0.00        0.00        0.00        2.07e-05    0.0   0.0   0.0    0.0
  75    0.0    0.0   0.00       0.00       0.00        0.00        0.00        0.00        0.00        0.0   0.0   0.0    0.0

sum :  663.   863.   36.9       29.6       5.14        2.11        30.3        4.43        7.74        230.  230.  192.   65.
           backscattered ions energy distribution
           number of histories =   1000   channel width5120.00000 (ev)
   0   1   0   0   0     0   0   1   0   0     0   0   0   0   0     0   0   0   0   1     0   0   0   0   0
   0   0   0   0   0     0   0   0   0   0     0   0   0   0   0     0   0   1   0   0     0   0   0   0   1
   0   0   0   0   0     0   0   1   0   1     0   0   0   0   0     0   0   0   0   0     0   0   0   0   0
   0   0   0   0   1     0   0   0   0   0     0   0   0   0   0     0   0   0   0   0     0   0   0   0   0

           sputtered atoms' energy distribution
           number of histories =   1000   channel width  10.00000 (ev)
   0   0   0   0   0     0   1   0   0   0     0   0   0   0   0     0   0   0   0   0     0   0   0   0   0
   0   0   0   0   0     0   0   0   0   0     0   0   0   0   0     0   0   0   0   0     0   0   0   0   0
   0   0   0   0   0     0   0   0   0   0     0   0   0   0   0     0   0   0   0   0     0   0   0   0   0
   0   0   0   0   0     0   0   0   0   0     0   0   0   0   0     0   0   0   0   0     0   0   0   0   0


        # histr. =    1000    energy(mev) =      0.90   iseed =        84550200738973


                                   end    HERAD   - end    HERAD
                                   end    HERAD   - end    HERAD
```

VI-5. Effect of Voids on the Damage Distribution

VI-5-1. 14 MeV Cu Ions on Ni

This section includes the results of the damage calculation for 14 MeV Cu ions on Ni without and with voids. The experimentally measured void distribution is that of Whitley [2].

First we consider the damage without the inclusion of the voids. Table 6-12 shows the results of the obtained ranges from the BRICE and HERAD codes. The difference between BRICE and HERAD is only 80 Å in the projected range, and 26 Å in the straggling of the projected range. However, the distribution of the projected range is skewed toward the front surface. Figure 6-20 shows the depth distribution as obtained from the two codes.

Figure 6-21 shows the damage distributions of HERAD with and without the transport of the recoils, and the damage distribution of BRICE. It is quite clear in this case (as in the case of Be on U) the recoils shift the distribution deeper into the material. The total damage energy deposited in the nickel target as given by the BRICE code is 1010 keV. The use of the LSS-Robinson formula (Eq. 5.43) in HERAD, for the energy partition predicts the damage energy is equal to 1070 keV. The damage energy as calculated by following the PKAs is 1323 keV which again shows that the LSS-Robinson formula underestimates the damage energy, in this high energy case, with a larger error than in the low energy case of Be on U.

Using a displacement energy of 30 eV, we obtained a total of 13255 defects, with 0.16 Ni atom sputtered per incident ion. Using

TABLE 6-12

Results of the Range Calculation from BRICE and HERAD Codes for the Case of 14 MeV Cu-Ni

(Units in Angstroms)

(Voids are not included in HERAD)

Ranges	Code	Mean	Median	Std. Dev.	Skewness	Kurtosis	Error	# Hist.
1) Depth	BRICE	20785.		2048.				
	HERAD	20704.	21166.	2074.	-1.66	4.39	66.	1000
2) Path	BRICE	22100.						
	HERAD	21965.	22306.	1716.	-1.63	4.41	54.	1000
3) Perpendicular	BRICE			3809.				
	HERAD	3562.	3400.	1857.	0.64	0.75	59.	1000
4) Vector Range	HERAD	21107.	21530.	1886.	-1.57	4.04	60	1000

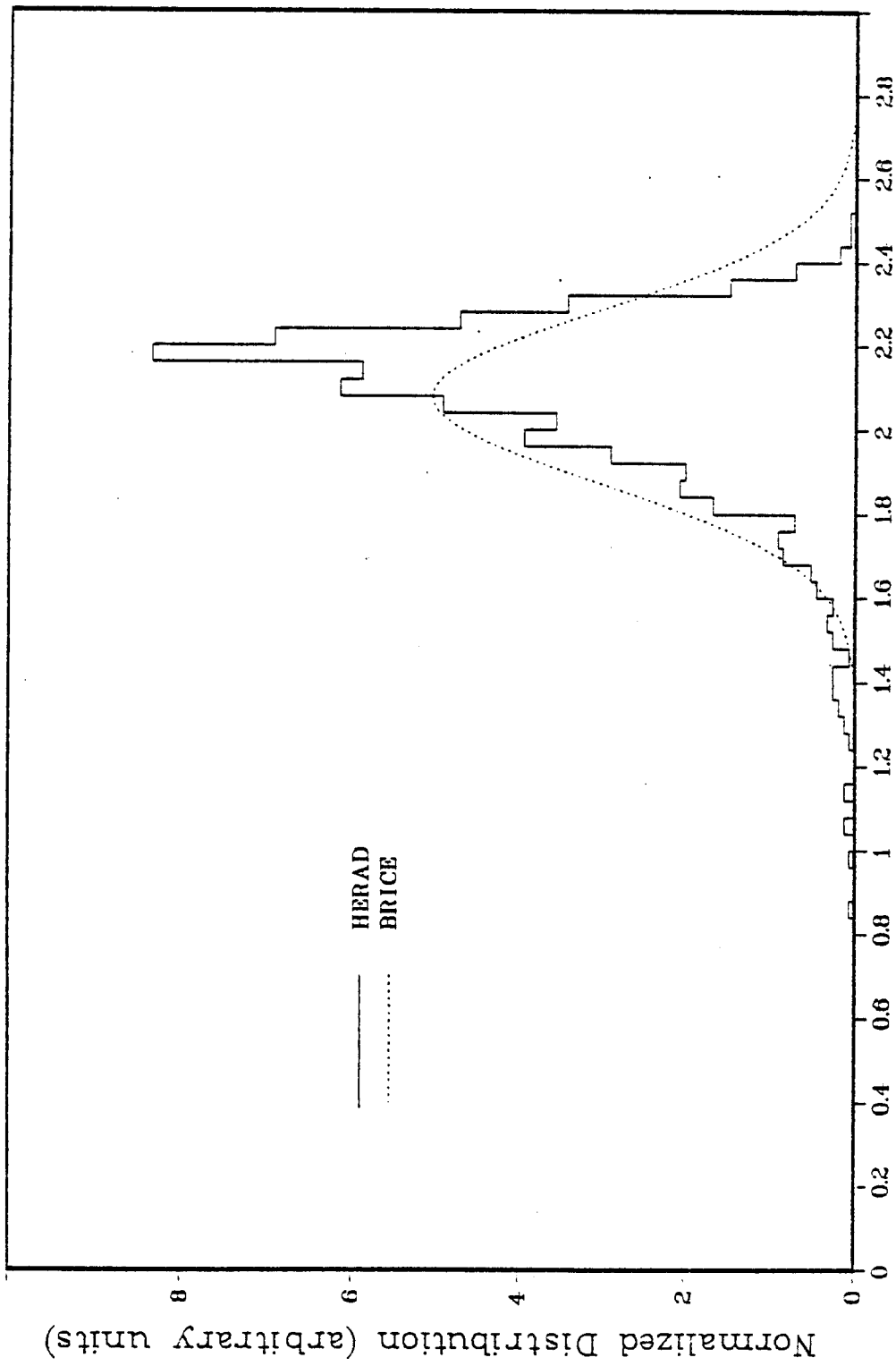

Fig. 6-20. The depth distribution for 14 MeV Cu on void-free nickel target.

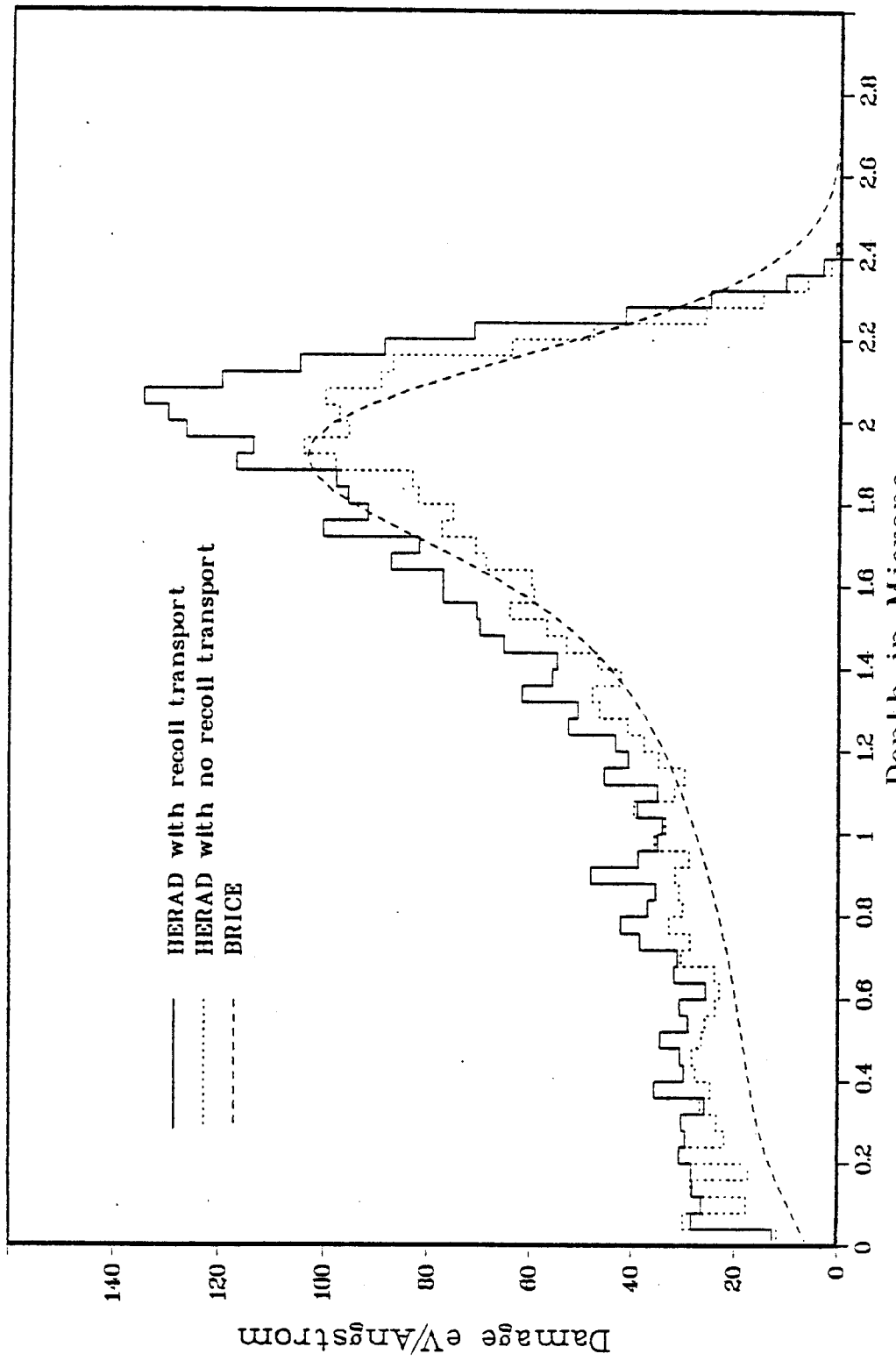

Fig. 6-21. The damage distribution for the case of 14 MeV Cu on void-free nickel target.

the K-P displacement model with a damage efficiency of 0.8, the total number of defects is 13466, 14267, and 17640, as obtained from BRICE, HERAD with no recoil-transport, and HERAD with recoil transport, respectively. These values again show that the normally used value of the damage efficiency, i.e. 0.8, is too high, and a value of 0.6, according to our calculation, would more accurately predict the total number of defects. Figure 6-22 shows the different defect distributions as well as the depth distribution of the replacement events. Notice that the so called near V-I pairs, which are very likely to annihilate each other, are about the same number density as the vacancies and interstitials. That means about half of the above mentioned number of defects would be available for any damage effect, i.e. loop or voids, formation. Figure 6-23 shows BRICE and HERAD defect distributions.

Next we consider the same case with the voids included in the nickel. Table 6-13a gives the measured swelling [2] in the different sections of the nickel target and Table 6-13b gives the calculated ranges. The maximum value of the swelling 2.4%. The average swelling is 1.6%.

The average depth (the projected range) as well as the average path length increased by 1.9%. The straggling in the projected range increased by 2.2%. The inclusion of the voids causes the peak of the projected range distribution to shift slightly away from the front surface. Figure 6-24 shows the projected range distribution.

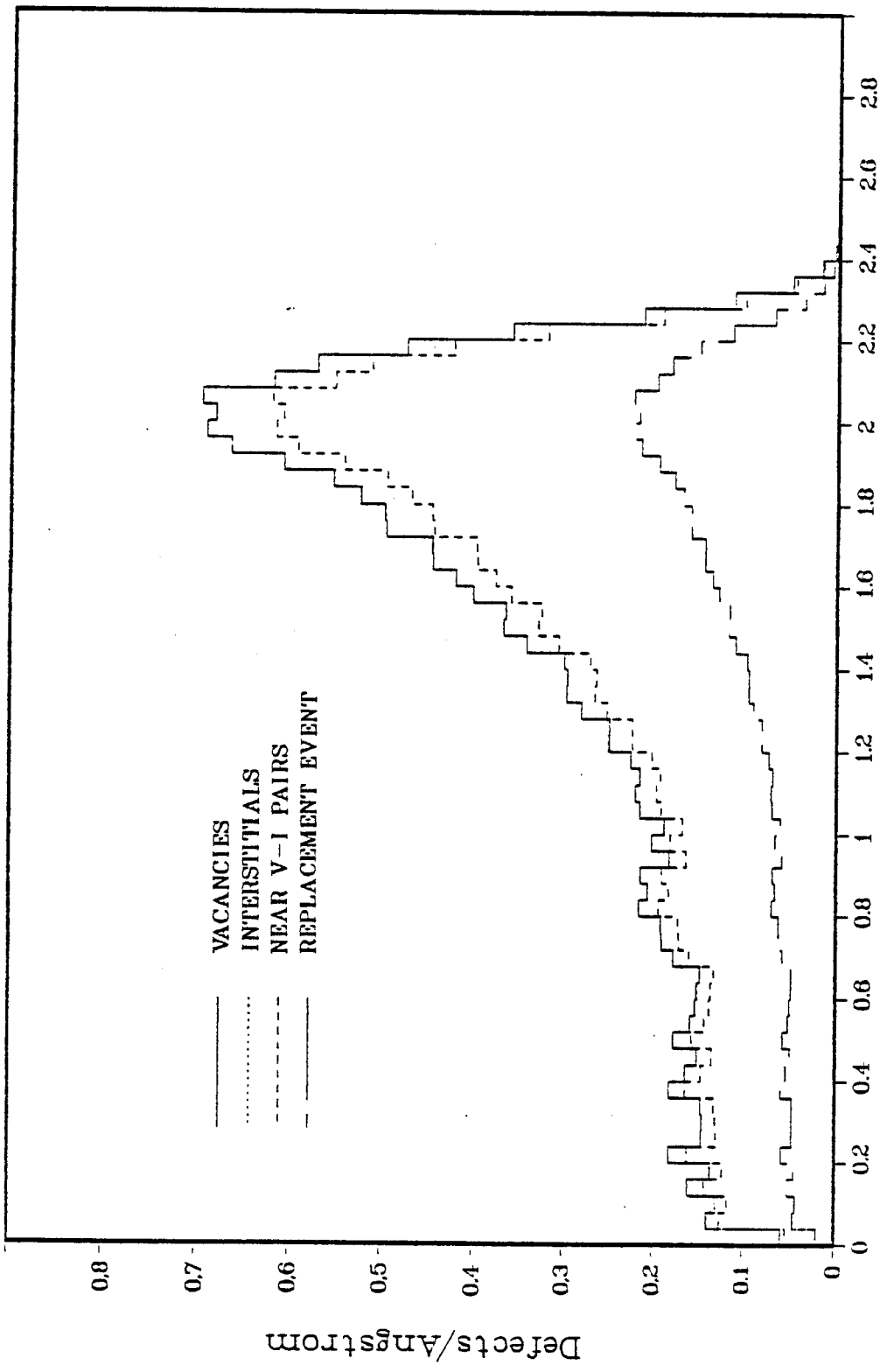

Fig. 6-22. The defect distribution for the case of 14 MeV Cu on void free Ni target.

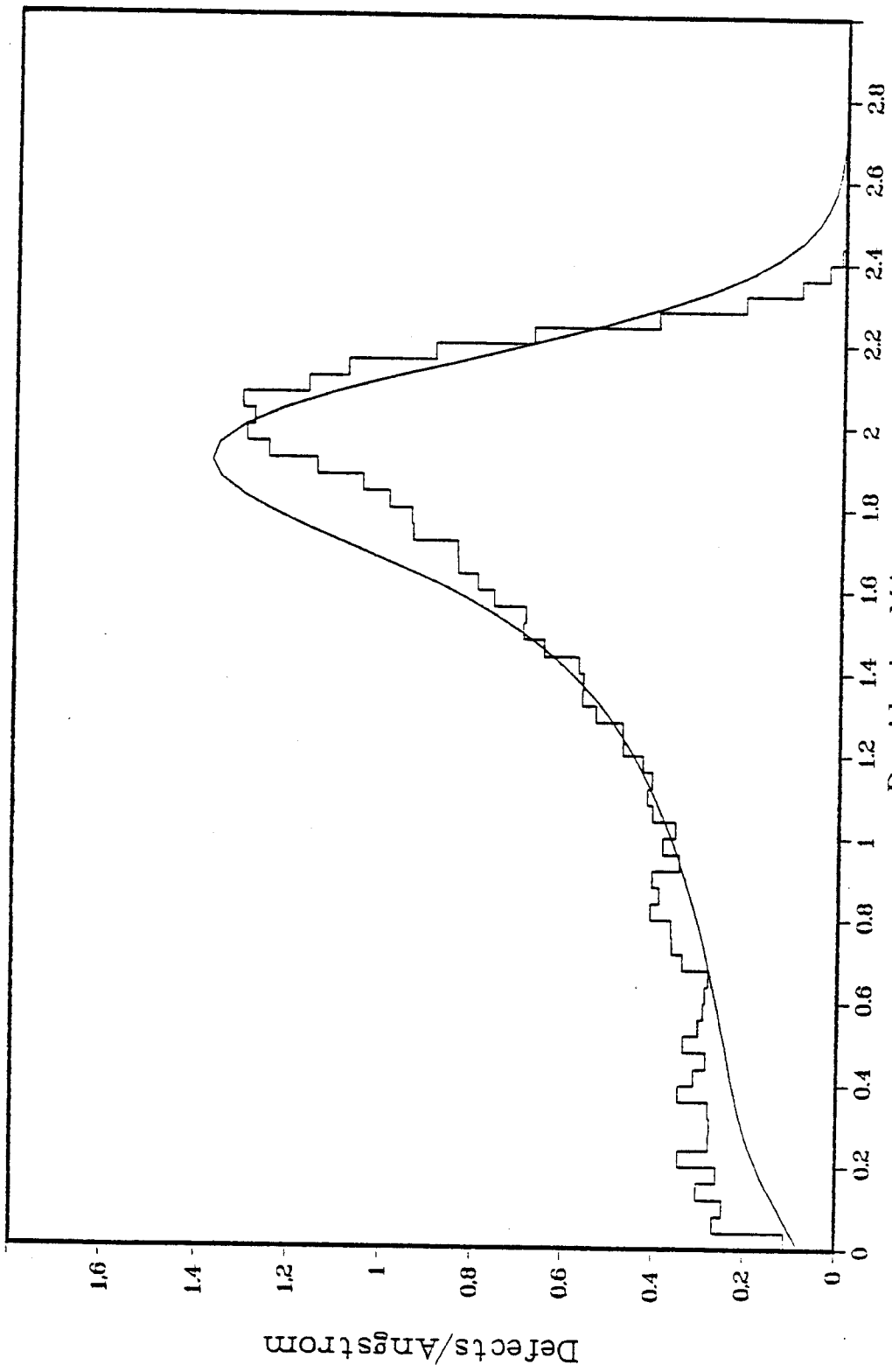

Fig. 6-23. The defect distribution as predicted by Brice (continuous line) and by HERAD (broken line).

TABLE 6-13a

Measured Swelling for 14 MeV Cu-Ni[2]

Section	Depth (μ)	ΔV/V%
1	0.0 - 0.25	1.0
2	0.25 - 0.5	1.61
3	0.5 - 0.75	1.58
4	0.75 - 1.0	1.81
5	1.0 - 1.25	1.91
6	1.25 - 1.50	1.86
7	1.50 - 1.75	2.0
8	1.75 - 2.0	2.4
9	2.0 - 2.25	2.4
10	2.25 - 2.50	1.5
11	2.50 - 2.75	0.97
12	2.75 - 3.0	0.28

TABLE 6-13b

The Range Calculation for 14 MeV Cu-Ni, As Obtained from the BRICE and HERAD Codes, With the Voids Included in HERAD

Ranges	Code	Mean	Median	Std. Dev.	Skewness	Kurtosis	Error	# Hist.
1) Depth	BRICE	20785.		2040.				
	HERAD	21073.	21551.	2120.	-1.66	4.36	67.	1000
2) Path	BRICE	22100.						
	HERAD	22361.	22712.	1755.	-1.63	4.39	56.	1000
3) Perpendicular	BRICE			3809.				
	HERAD	3634.	3456.	1893.	0.64	0.73	60.	1000
4) Vector Range	HERAD	21486.	21920.	1920.	-1.57	4.02	61.	1000

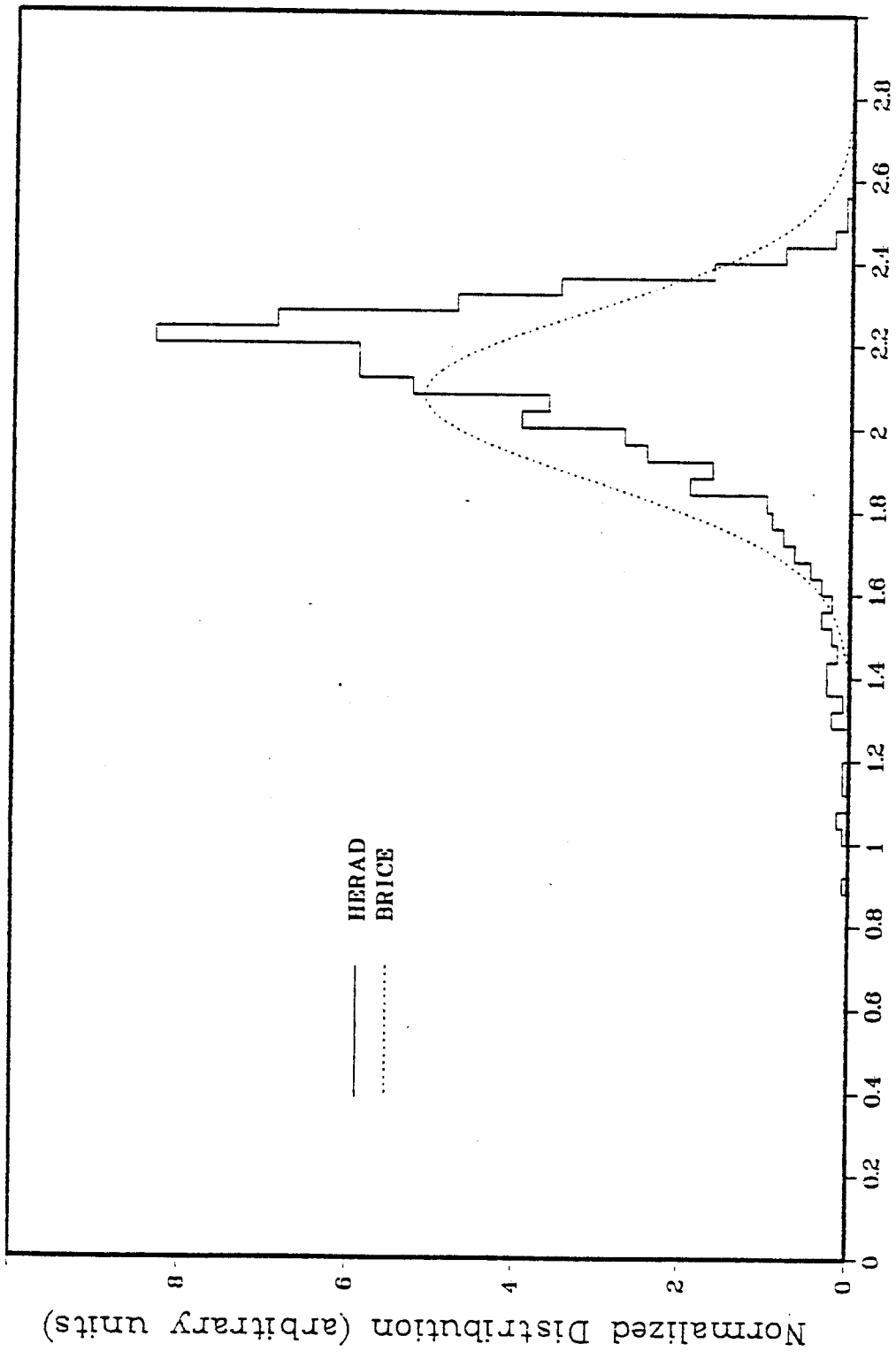

Fig. 6-24. The depth distribution for 14 MeV Cu ions incident on nickel target containing voids.

Because of the low value of swelling in this case one cannot see large effects of the cavities on the ranges; however, the direct calculations with the swelling included gives more effect than if a global density correction was made. It should be pointed out that the inclusion of the voids in our calculations would allow for more accurate estimation of the effect of the voids on the range, since it considers this effect during the slowing down and in the 3-D space.

With respect to the damage, Fig. 6-25 shows the swelling profile together with the calculated damage from BRICE and from HERAD with the voids included in the calculations. The first moment of the damage increased by 1.7%. The square root of the second moment (the standard deviation) increased by a factor of 1.9%. The skewness increased slightly (less negative) but was still negative, i.e. the distribution is skewed toward the front surface. The kurtosis becomes more negative, i.e. the distribution becomes flatter at the top. The first moment of the damage around the penetration axis increased by 1.7%.

Again because of the low swelling values in this case, the effect is not large enough to illustrate the effect of the swelling on the calculated damage. This is in contrast to the work of Odette et al. [24] who assumed 50% peak swelling in their work. Although there are many reported large values of swelling, to the best of our knowledge there is no available data for swelling-depth measurement which has such high values of swelling. Finally, in this case, Figs.

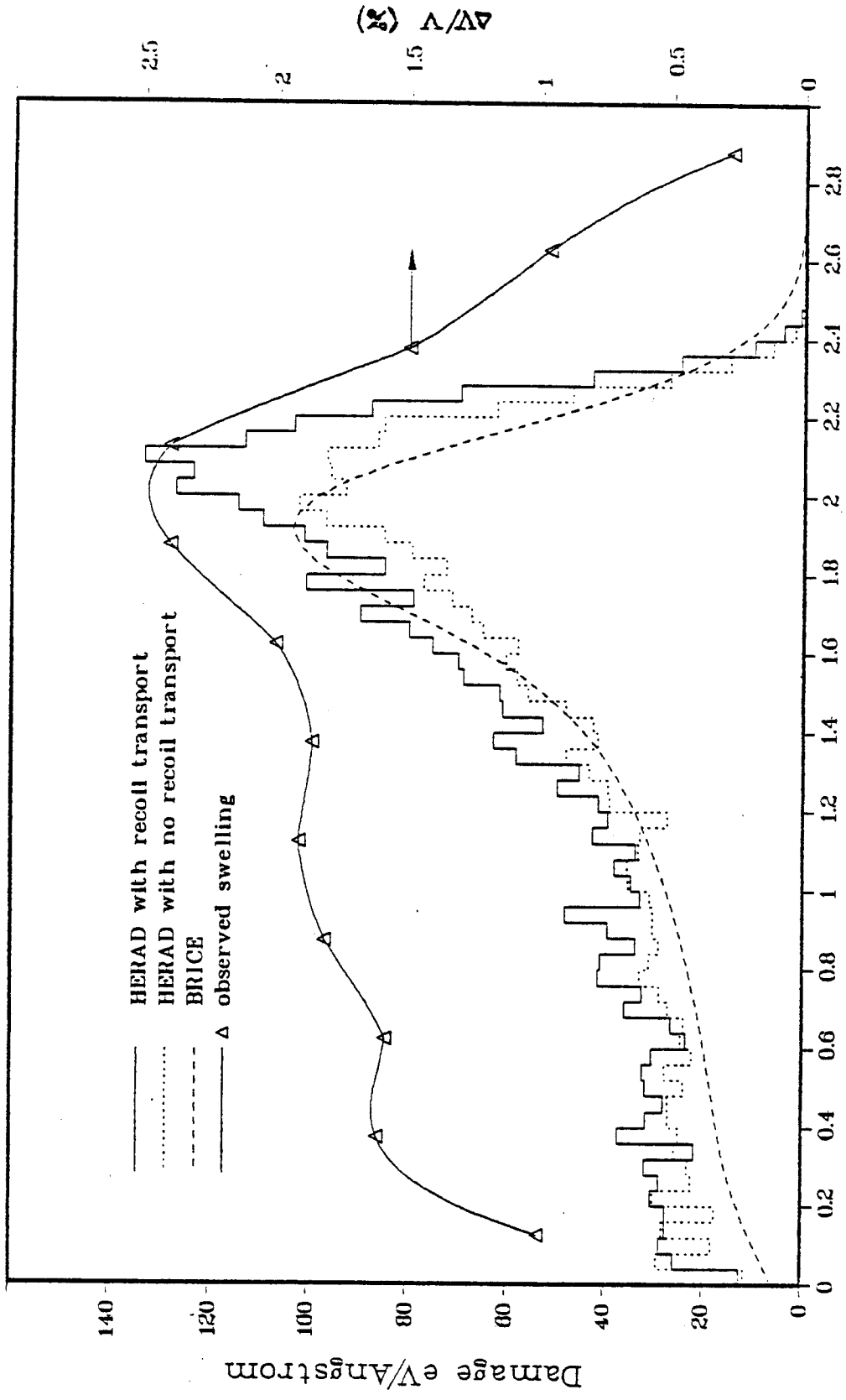

Fig. 6-25. The damage energy for 14 MeV Cu ions incident on nickel target containing voids.

6-26 and 6-27 show the defect distributions from the HERAD and BRICE codes.

VI-5-2. 20 keV He Ions on Ni

Fenske et al. [25] have recently measured the swelling profile as a function of the implant depth for 20 keV He in nickel. The difference between the theoretical prediction (using BRICE and TRIM) of the damage profile and the measured swelling profile was reported to be as much as 50%. In their conclusion, they suggested that the LSS electronic stopping should be reduced by a factor 20% to achieve better agreement between the theory and the experiment. The HERAD code was used to test the validity of this suggestion with respect to the damage distribution.

The HERAD calculations included 10,000 histories, with cavities included in the calculations, and with different electronic stopping powers. The following ratios of the LSS electronic stopping were used; 1., 0.8, 0.6, 0.4, 0.2, and 0, i.e. with electronic stopping completely neglected. Figure 6.28 shows the results of these calculations. The reduction of LSS electronic stopping being a factor of only 0.2 appears to have no effect on bringing the calculated damage profile closer to the swelling profile. Reducing the electronic stopping by a factor of 0.6 and 0.8 shows a much closer agreement between the calculated damage and the measured swelling and perhaps the best value would be 0.7. Complete neglect of LSS stopping would cause the helium to be injected much too far into the nickel.

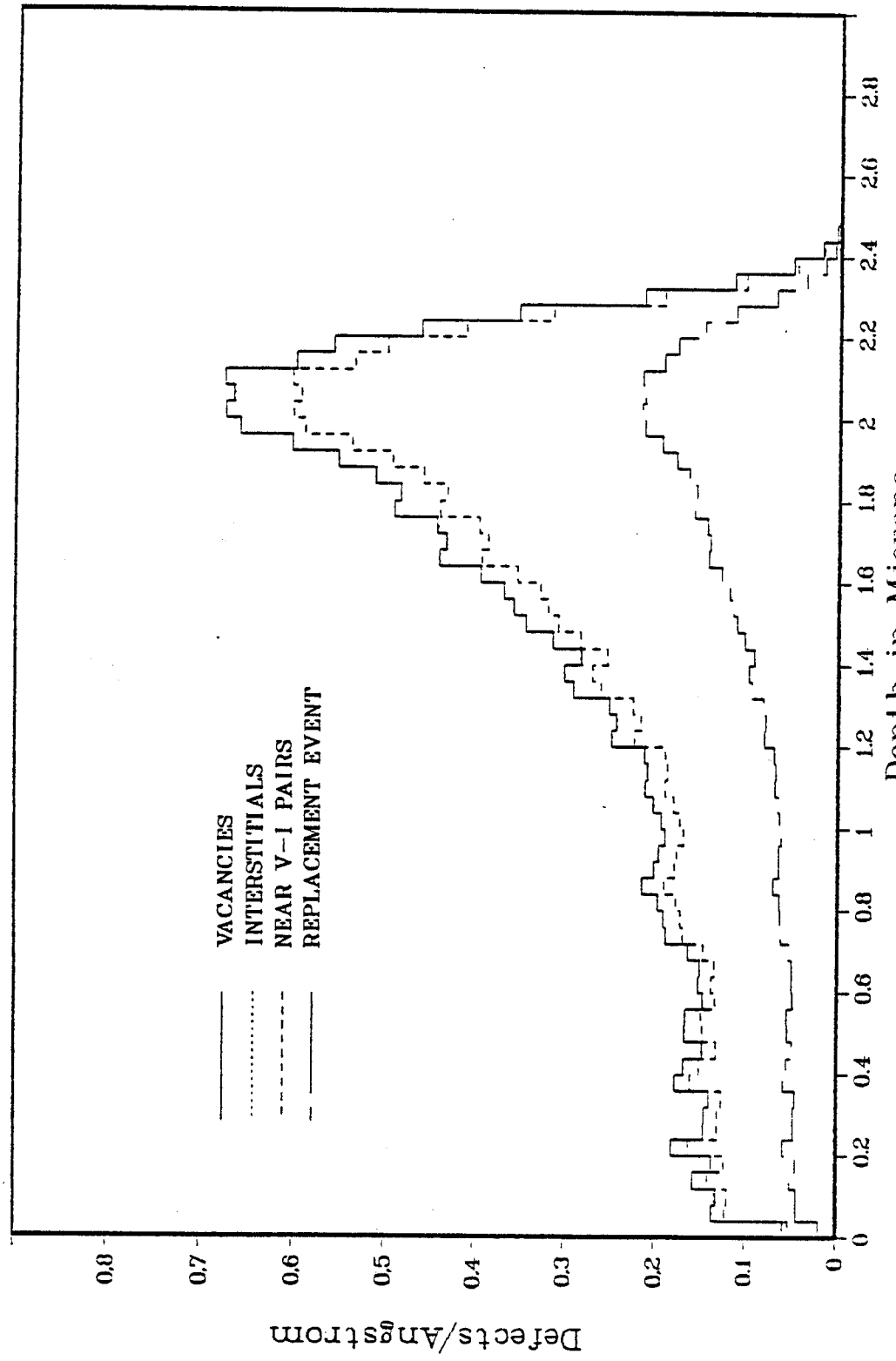

Fig. 6-26. The defect distribution for 14 MeV Cu on Ni containing voids.

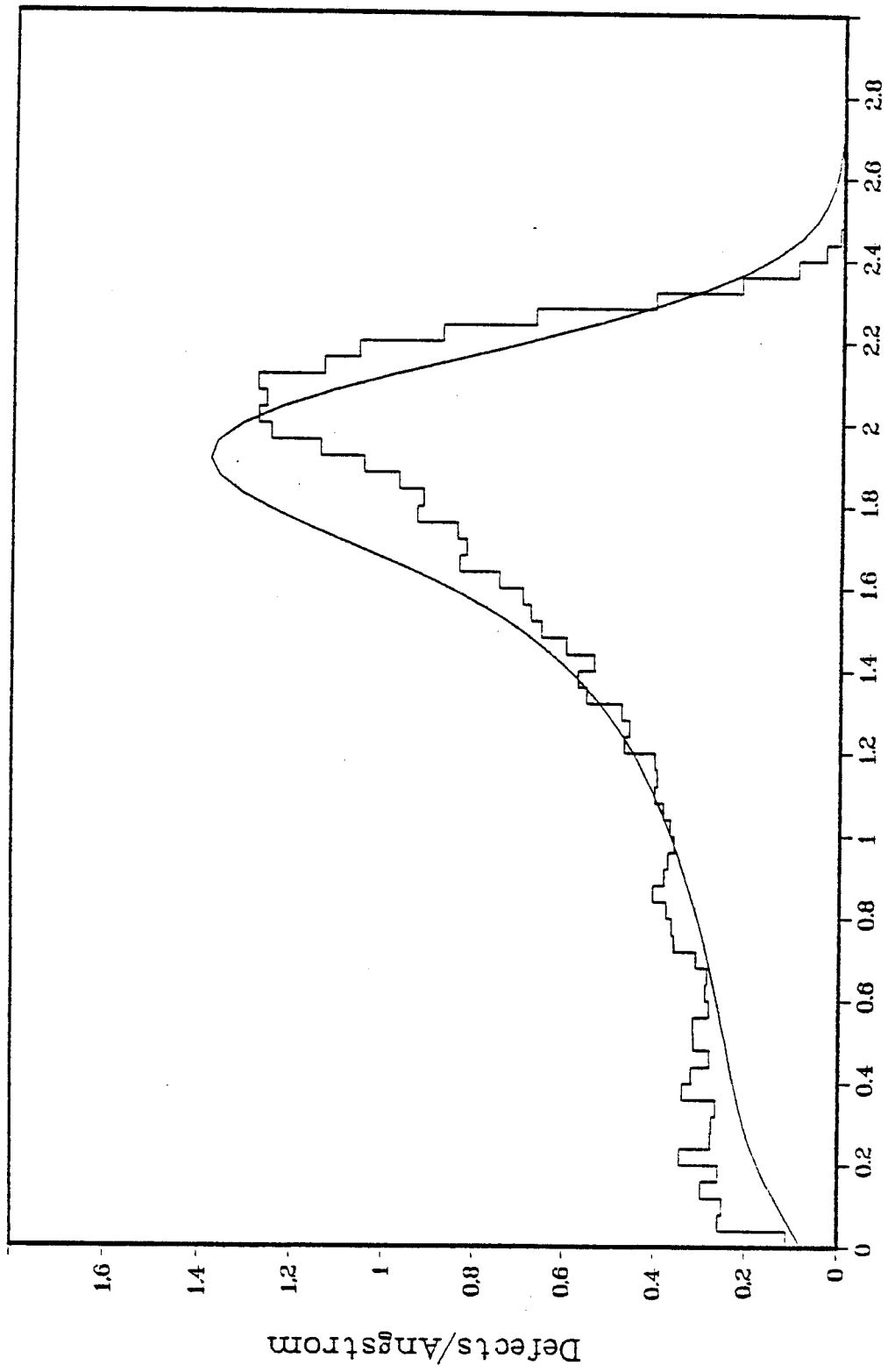

Fig. 6-27. The defect distribution for 14 MeV Cu-Ni. Voids are included in HERAD. The continuous curve corresponds to BRICE and the broken curve corresponds to HERAD.

a. $k = k_{LSS}$

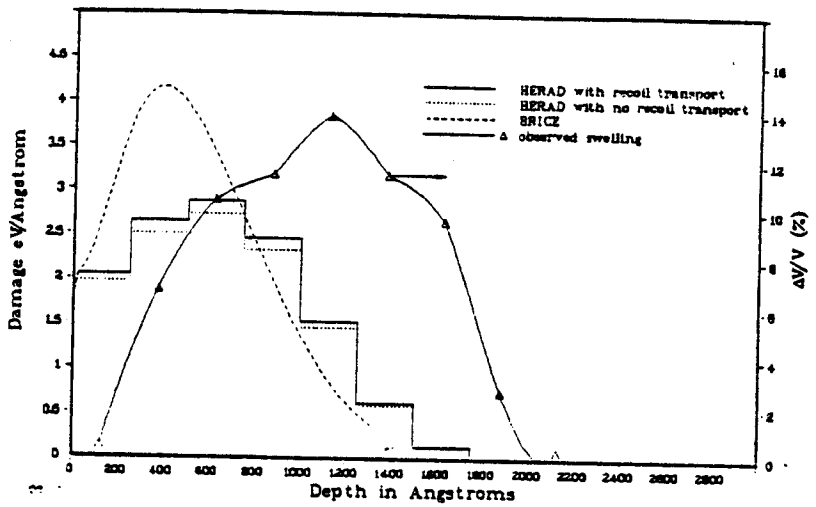

b. $k = .8\ k_{LSS}$

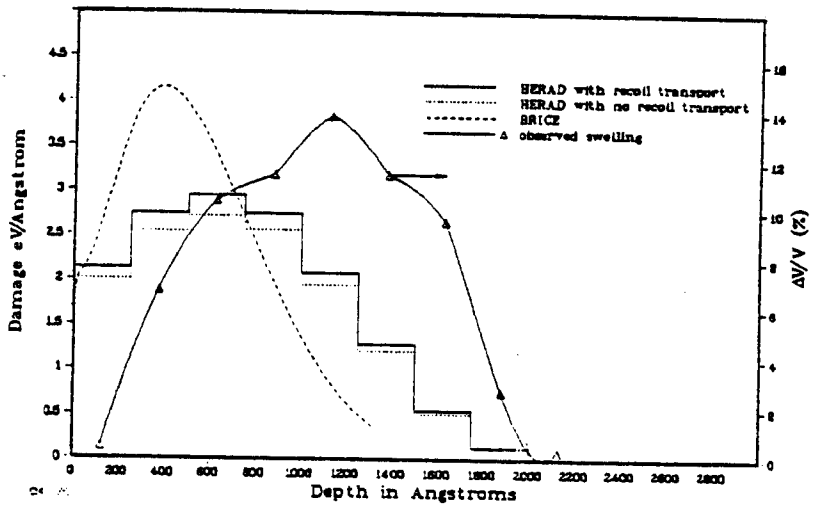

c. $k = .6\ k_{LSS}$

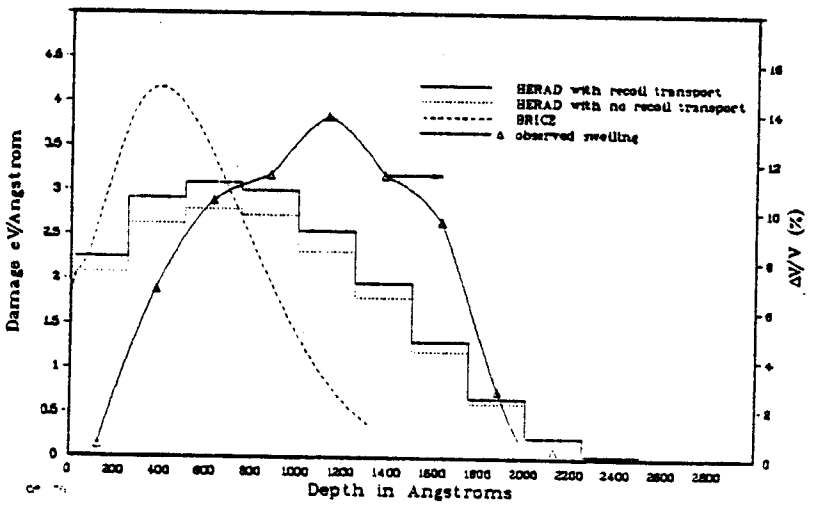

Fig. 6-28. The swelling and the damage profiles for 20 KeV He ions on Ni; with different electronic stopping used in HERAD.

d. $k = .4\ k_{LSS}$

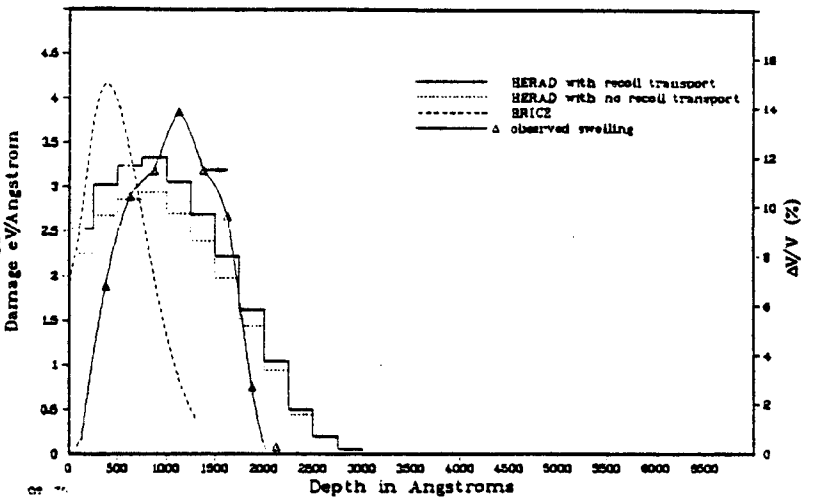

e. $k = .2\ k_{LSS}$

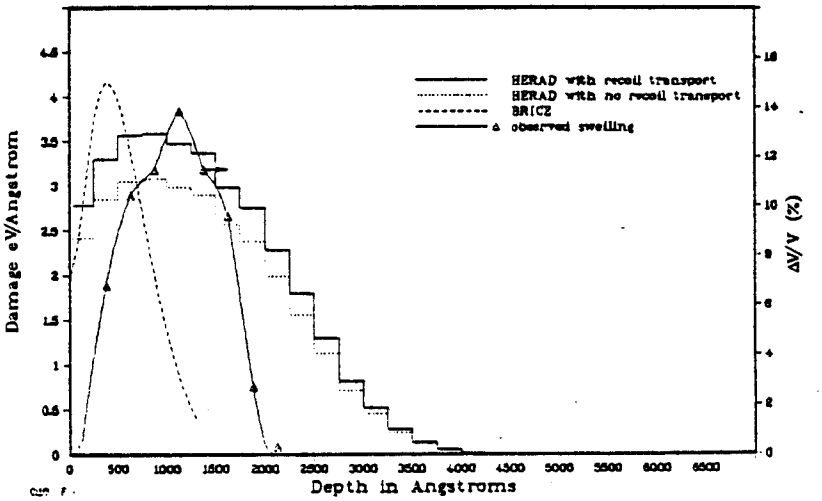

f. $k = 0.0$

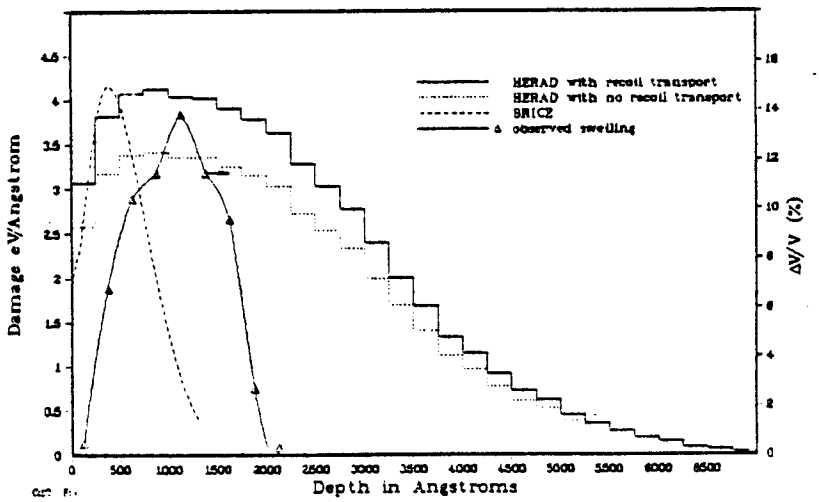

Fig. 6-28 (continued).

Unfortunately there are no experimental measurements for the electronic stopping of He in Ni for energies below 30 keV [26] which would guide us in choosing a proper value for the electronic stopping.

VI-6. Concluding Remarks

The peak of the calculated damage profile of the HERAD code with or without the voids included is closer to the observed swelling peak than that of the BRICE code. With the voids included the peak is closer to that observed experimentally. In any case, we were still not able to match the calculated damage to the swelling profile at the far end of the profile.

Because of the low values of the swelling we have not been able to notice the anticipated crucial effect of the pressure of cavities on the damage calculations.

The typical value of 0.8 for the damage efficiency is, as we noticed, high; a value of 0.6-0.7 is more realistic in predicting the number of defects with the Kinchen and Peace model. About half of the born defects are near enough to be annihilated. We noticed that the partition formula of Lindhard underestimates the damage energy and overestimates the electronic energy loss of the PKAs.

More systematic and precise experimental work is needed in the area of electronic stopping and the determination of the ranges of ions in material.

References for Chapter VI

1. G. Fenske, S. K. Das, M. Kaminsky, and G. H. Miley, J. Nucl. Mat. 85 & 86, 707 (1979).

2. J. B. Whitley, Ph.D. Thesis, University of Wisconsin-Madison, (1978).

3. G. Fenske, S. K. Das, M. Kaminsky, and G. H. Miley, J. Nucl. Mat. 76 & 77, 247 (1978).

4. J. Narayan, O. S. Oen, and T. S. Noggle, J. Nucl. Mat. 71, 160 (1977).

5. I. Manning and G. P. Mueller, Comp. Phys. Commun. 7, 85 (1974).

6. D. K. Brice, Ion Implantation Range and Energy Deposition Codes CORE1, RASE4 and DAMG2. SAND75-0622 (1977); in the text we used "BRICE" to refer to these three codes.

7. a) J. B. Biersack private communications.
   b) J. B. Biersack and L. G. Haggmark, Nucl. Inst. Meth. 174 257 (1980).

8. M. T. Robinson and I. M. Torrens, Phys. Rev. B9, 5008 (1974).

9. M. T. Robinson, private communication.

10. M. T. Robinson, Proc. Int. Conf. on "Radiation-Induced Voids in Metals," Albany, NY, June 1971, CONF-710601, 397 (1972).

11. H. Attaya and G. L. Kulcnski, Transactions, American Nuclear Society 34, 224 (1980).

12. M. Kaminsky, Adv. Chem. Series 158, 112 (1976).

13. J. Roth, Inst. Phys. Conf. Series 28, 280 (1976).

14. R. Behrisch, J. Bottiger, W. Eckstein, U. Littmark, J. Roth, and B. M. U. Scherzer, Appl. Phys. Lett. 27, 199 (1975).

15. O. S. Oen and M. T. Robinson, Ref. 13, p. 329.

16. J. L. Combasson, B. W. Farmery, D. McMculloch, G. W. Neilson, and M. W. Thompson, Rad Eff. 36, 149 (1978).

17. a) H. Oetzmann, A. Feuerstein, H. Grahmann, and S. Kalbitzer, Phys. Lett. 55A, 170 (1975).
    b) A. Feuerstein, S. Kalbitzer and H. Oetzmann, Phys. Lett. 51A, 165 (1975).

c) H. Oetzmann, A. Feuerstein, H. Grahmann, and S. Kalbitzer, Proc. Int. Conf. on "Ion Beam Surface Layer Analysis," Karlsruhe, 1975, ed. O. Mayer, p. 245 (1976).

18. a) W. A. Grant, J. S. Williams, and D. Dodds, Ref. 17c, p. 235.
b) R. A. Baragiola, D. Chivers, D. Dodds, W. A. Grant, and J. S. Williams, Phys. Lett. 56A, 371 (1976).
c) W. A. Grant, D. Dodds, J. S. Williams, C. E. Christodoulids, R. A. Baragiola, and D. Chivers, Proc. 5th Int. Conf. Ion Implantation, August 1976, (Boulder, Colorado, USA).

19. M. Bister, M. Hautala, and M. Jäntti, Rad. Eff. 42, 201 (1979).

20. S. Furukawa and H. Matsumura, private communication in Ref. 18(a).

21. H. E. Schiott, Proc. Int. Conf. on Ion Implantation, Thousand Oaks, CA, USA (1970). Gordan and Breach, London, p. 197 (1971).

22. a) C. W. Maynard, private communications.
b) C. W. Maynard, in Symp. on "Neutron Cross Sections from 10 to 40 MeV," held at Brookhaven National Laboratories, NY, 1977, BNL-NCS-50681, p. 375 (1977).

23. V. V. Federov, "Theory of Optimal Experiments," Academic Press, NY, 1972, p. 33.

24. G. R. Odette, D. Schwartz and A. Ardell, Rad. Eff. 22, 217 (1974).

25. G. Fenske, S. K. Dao, and M. Kaminsky, to be published in Appl. Phys. Lett.

26. J. F. Ziegler, Helium, Stopping Powers and Ranges in All Elemental Matter, Pergamon Press, NY (1977).

CHAPTER VII

SUMMARY AND CONCLUSIONS

The 3-D Monte Carlo code, HERAD, has been developed in this work to study the ranges of ions, and the damage produced by those ions in material. The model used in HERAD incorporates different electronic and nuclear stopping models, and takes into account the effect of cavities on the ion distribution and the damage distribution.

With respect to the ion range, comparisons have been made between the results of HERAD and those predicted by most all of the available codes in the literature. In some cases it was possible to compare recent experimental measurements of the ion range in material to the predictions of HERAD.

These comparisons show:

a) The choice of the electronic energy loss law is very important in the high energy region ($\varepsilon > 10$). A noticeable difference was found between the existing theoretical models and the reasons for that difference have been documented.

b) In the high energy region ($\varepsilon > 10$) our results show that there is no appreciable difference in the range of the ions when either the Thomas-Fermi or Moliére potentials were used.

c) There is an urgent need for precise experimental measurements of the electronic stopping and ion range in this high energy region. Unfortunately, no experimental data is presently available to check the validity of the different theoretical models over a wide range of ion-target-energy combinations.

d) In the low energy region ($\varepsilon < 0.1$), the choice of the interatomic potential is critical. The HERAD code has used the Born-Mayer potential in this region which yields a very good agreement with most experimental data. However, there is a noticeable disagreement between the theory and some of these experimental results of ion straggling.

e) A simple linear regression analysis was performed to find the suitable values of the physical parameters which would give better agreement with the experimental results. This analysis suggests that there may be an oscillatory electronic and nuclear stopping dependence on Z_1 and Z_2 which have not been taken into account in the existing models.

f) The HERAD code has been shown to be much less expensive than other Monte Carlo codes and provides more statistical information than the analytical codes.

With respect to the damage distribution calculations it was found that:

g) The partition formula of Lindhard underestimates the damage energy and overestimates the electronic energy loss.

h) A damage efficiency of 0.6-0.7 is more realistic than the value of 0.8 which is usually used in predicting the number of defects.

i) About half of the total number of defects born during the ion slowing down have small distances of separation and most probably will be annihilated, leaving only half of the defects available for any damage effect, i.e. loops or void formation.

With respect to the effect of voids on the damage distribution it was found that:

j) The peak of the calculated damage profile using HERAD is closer to the observed swelling peak than that predicted by the BRICE code regardless of whether voids were or were not included in the calculation.

k) When the voids are included in the HERAD calculation the damage peak moves closer to that of the measured swelling profile.

l) It was not possible to match the swelling profile at the end of the range of 14 MeV Cu ion on Ni with HERAD or any other code presently in use.

m) The LSS electronic stopping seems to highly overestimate the electronic loss for low z ions at low energy. Having the electronic stopping power reduced to 80% of the LSS electronic stopping power, as has been recommended in past studies, will have relatively little effect on the agreement between the theory and experiment in the case of 20 keV He on Ni. It was found that electronic stopping power with values of 40-80% of the LSS stopping power is needed to achieve reasonable agreement.